

A Thesis Submitted for the Degree of PhD at the University of Warwick

Permanent WRAP URL:

<http://wrap.warwick.ac.uk/177401>

Copyright and reuse:

This thesis is made available online and is protected by original copyright.

Please scroll down to view the document itself.

Please refer to the repository record for this item for information to help you to cite it.

Our policy information is available from the repository home page.

For more information, please contact the WRAP Team at: wrap@warwick.ac.uk

Ultrafast Spectroscopy of Natural Sunscreen Filters



WARWICK
THE UNIVERSITY OF WARWICK

Jack Matthew Woolley

Thesis Submitted for the Qualification of

Doctor of Philosophy in Chemistry

Department of Chemistry

University of Warwick

July 2020

Table of Contents

List of Figures	vi
List of Tables.....	viii
List of Abbreviations.....	ix
Acknowledgements	xi
Declarations.....	xii
Abstract	xiii
1 Introduction.....	1
1.1 Photoprotection	2
1.1.1 Solar Radiation and the Atmosphere	2
1.1.2 Human Photoprotection	3
1.1.3 Sunscreens.....	3
1.2 Molecular Photochemistry	6
1.2.1 Fundamental Principles.....	6
1.2.1.1 Schrödinger Equation	6
1.2.1.2 Transition Dipole Moment	7
1.2.1.3 Franck-Condon Principle	8
1.2.1.4 Uncertainty Principle.....	9
1.2.1.5 Conical Intersections	10
1.2.2 Jablonski Diagram.....	12
1.2.2.1 Absorption.....	12
1.2.2.2 Radiative Decay Pathways	14
1.2.2.3 Internal Conversion and Intersystem Crossing.....	14
1.2.2.4 Vibrational Relaxation	15
1.2.2.5 Photodissociation.....	16
1.3 Spectroscopic Investigations of Sunscreens	16
1.3.1 Mycosporine-like Amino Acids	18
1.3.1.1 Advances in MAA photochemistry	19

1.3.2	Cinnamates.....	22
1.3.2.1	Advances in Cinnamate Photochemistry.....	22
1.4	Pump-Probe Spectroscopy	25
1.4.1	Transient Electronic Absorption Spectroscopy.....	25
1.4.1.1	Ground State Bleach (GSB)	27
1.4.1.2	Excited State Absorption (ESA).....	27
1.4.1.3	Stimulated Emission (SE)	27
1.4.1.4	Photoproducts	28
1.5	Computational Chemistry.....	28
1.6	Summary	29
1.7	Bibliography	31
2	Experimental	41
2.1	Femtosecond Pulse Generation	42
2.1.1	Laser Operation	42
2.1.1.1	Population Inversion.....	42
2.1.1.2	Optical Cavities	44
2.1.2	Mode Locking	46
2.1.3	Chirped Pulse Regenerative Amplification.....	47
2.2	Nonlinear Optical Processes.....	48
2.2.1	Frequency Conversion	49
2.2.2	Optical Parametric Amplification	50
2.2.3	Super Continuum Generation.....	51
2.3	Transient Electronic Absorption Spectroscopy Setup.....	51
2.3.1	Laser Details.....	52
2.3.2	Pump Beam Generation	53
2.3.2.1	Harmonic Generation	53
2.3.2.2	TOPAS	53
2.3.3	Probe Beam Generation	55
2.3.4	Sample Interaction	56

2.3.4.1	Pump-Probe Interaction.....	56
2.3.4.2	Group Velocity Dispersion.....	57
2.3.4.3	Instrument Response	58
2.3.4.4	Sample Delivery	59
2.3.5	Data Collection and System Control.....	59
2.4	Data Processing	60
2.4.1	Global Fitting Analysis	62
2.4.2	Chirp Correction.....	63
2.5	Summary	64
2.6	Bibliography	65
3	Photoprotection Properties of Mycosporine Amino Acid Motifs.....	68
3.1	Introduction	69
3.2	Experimental Methodology	70
3.2.1	Synthesis and Characterisation	70
3.2.2	Experimental Details.....	70
3.2.3	Calculations.....	71
3.3	Results	71
3.3.1	Sample Characterisation.....	71
3.3.2	Transient Electronic Absorption Spectroscopy Measurements	72
3.4	Discussion	73
3.5	Conclusions	77
3.6	Supporting Information	79
3.6.1	Fitting Residuals	79
3.6.2	Power Dependencies	79
3.7	Bibliography.....	81
4	Symmetric Functionalisation Effects on the Photoisomerisation Pathway of a UV Filter	83
4.1	Introduction	84

4.2	Experimental Methodology	85
4.2.1	Synthesis and Characterisation	85
4.2.2	Experimental Details	85
4.2.3	Calculations.....	86
4.3	Results	87
4.3.1	Sample Characterisation.....	87
4.3.2	Steady-State Spectroscopy Measurements.....	88
4.3.3	Transient Electronic Absorption Spectroscopy Measurements	90
4.4	Discussion	90
4.5	Conclusion.....	95
4.6	Supporting Information	96
4.6.1	Fitting Residuals	96
4.6.2	Power Dependencies	97
4.7	Bibliography.....	98
5	Expanding on the <i>Bottom-up</i> and Functionalisation Approaches	101
5.1	The Photodynamics of Bacterial Sunscreens	102
5.1.1	Experimental Methodology.....	103
5.1.1.1	Biosynthesis and Extraction	103
5.1.1.2	Experimental Details	104
5.1.2	Results.....	104
5.1.2.1	Transient Electronic Absorption Spectroscopy Measurements.....	104
5.1.3	Discussion	105
5.1.4	Conclusions for Bacterial Sunscreens.....	110
5.2	Effects of Positional Substitution on Photoisomerisation	111
5.2.1	Experimental Methodology.....	111
5.2.1.1	Synthesis and Characterisation.....	111
5.2.1.2	Experimental Details	112
5.2.1.3	Calculations	113

5.2.2	Results	113
5.2.2.1	Transient Electronic Absorption Spectroscopy Measurements.....	113
5.2.2.1	Calculations	114
5.2.2.2	Steady-State Spectroscopy Measurements.....	114
5.2.3	Discussion	115
5.2.4	Conclusions for Substituent Effects on Photoisomerisation	117
5.3	Supporting Information	119
5.3.1	Fitting Residuals	119
5.3.2	Power Dependencies	120
5.4	Bibliography.....	121
6	Conclusions and Outlook	124
6.1	Conclusions	125
6.2	Outlook.....	127
6.2.1	Mycosporine–Like Amino Acids.....	127
6.2.2	Functionalisation and Substituent Effects of Cinnamates.....	128
6.3	Bibliography.....	129

List of Figures

Figure 1.1 Structure of the atmosphere and solar spectrum	2
Figure 1.2 Common UV filters in current commercial products	4
Figure 1.3 Franck-Condon principle	9
Figure 1.4 Representation of conical intersections	11
Figure 1.5 Jablonski diagram	12
Figure 1.6 Chemical structures of common mycosporine-like amino acids	19
Figure 1.7 Chemical structures studied by Losantos <i>et al</i>	19
Figure 1.8 Minimum energy pathways computed by Losantos <i>et al</i>	20
Figure 1.9 Chemical structures of cinnamates	22
Figure 1.10 Simple transient absorption spectroscopy setup	26
Figure 1.11 Components of transient absorption spectroscopy signal	27
Figure 2.1 Schematic of laser systems	43
Figure 2.2 Fabry-Perot laser cavity	45
Figure 2.3 Laser cavity modes in a laser lineshape envelope	45
Figure 2.4 Mode locking in a cavity	46
Figure 2.5 Chirped pulse amplification	48
Figure 2.6 Nonlinear optical processes	50
Figure 2.7 Optical parametric amplification	51
Figure 2.8 Schematic of main laser table	52
Figure 2.9 Schematic of transient absorption spectroscopy table	54
Figure 2.10 White light generation setup	55
Figure 2.11 Spectrum of white light probe	56
Figure 2.12 Pump-probe geometry at sample interaction	57
Figure 2.13 Time zero as a function of probe wavelength	58
Figure 2.14 Instrument response as a function of probe wavelength	58
Figure 2.15 Picture of sample flow setup	59
Figure 2.16 Fitting models	61

Figure 2.17 Effect of chirp correction on transients	64
Figure 3.1 Chemical structures of ACyO and NN	70
Figure 3.2 UV/Vis and ¹ H NMR spectra of ACyO and NN	71
Figure 3.3 TAS of ACyO	72
Figure 3.4 TAS of NN	73
Figure 3.5 EADS of ACyO and NN extracted from global fit	74
Figure 3.6 Schematic of ACyO and NN relaxation	77
Figure S3.1 Fitting residuals from global fitting of ACyO and NN	79
Figure S3.2 Power dependencies of ACyO	80
Figure S3.3 Power dependencies of NN	80
Figure 4.1 Chemical structures and UV/Vis of <i>p-E,E</i> -DPD	85
Figure 4.2 ¹ H NMR of <i>p-E,E</i> -DPD	86
Figure 4.3 Steady-state spectra and ¹ H NMR of <i>p-E,E</i> -DPD	88
Figure 4.4 TAS of <i>p-E,E</i> -DPD	89
Figure 4.5 2.5 ns TAS of <i>p-E,E</i> -DPD	90
Figure 4.6 EADS of <i>p-E,E</i> -DPD extracted from global fit	91
Figure 4.7 Schematic of <i>p-E,E</i> -DPD relaxation	92
Figure 4.8 Power dependencies of 2.5 ns TAS for <i>p-E,E</i> -DPD	93
Figure S4.1 Fitting residuals extracted from the global fit of <i>p-E,E</i> -DPD	96
Figure S4.2 Power dependencies of <i>p-E,E</i> -DPD	97
Figure 5.1 UV/Vis and structures of MAAs	103
Figure 5.2 TAS of MAAs	105
Figure 5.3 EADS of Sample 1 extracted from global fit	106
Figure 5.4 EADS of Sample 2 extracted from global fit	108
Figure 5.5 Selected TAS of MAAs	109
Figure 5.6 UV/Vis and structures of substituted methyl cinnamate structures	111
Figure 5.7 ¹ H NMR of <i>o-E,E</i> -DPD and <i>m-E,E</i> -DPD	112
Figure 5.8 TAS of <i>o-E,E</i> -DPD and <i>m-E,E</i> -DPD	114
Figure 5.9 Steady-state spectra and ¹ H NMR of <i>o-E,E</i> -DPD and <i>m-E,E</i> -DPD	115

Figure 5.10 EADS of <i>o</i> - <i>E,E</i> -DPD and <i>m</i> - <i>E,E</i> -DPD extracted from global fit	116
Figure S5.1 Fitting residuals from global fitting of MAAs	119
Figure S5.2 Fitting residuals from global fitting of <i>o</i> - <i>E,E</i> -DPD and <i>m</i> - <i>E,E</i> -DPD ...	119
Figure S5.3 Power dependencies of MAAs	120
Figure S5.4 Power dependencies of <i>o</i> - <i>E,E</i> -DPD and <i>m</i> - <i>E,E</i> -DPD	120

List of Tables

Table 3.1 Extracted lifetimes from the global fit of ACyO and NN	74
Table 3.2 Calculated energies of critical points on the S ₁ surface of ACyO	74
Table 4.1 Calculated energies and transition oscillator strengths for DPD	87
Table 4.2 Extracted lifetimes from the global fit of <i>p</i> - <i>E,E</i> -DPD	91
Table 5.1 Extracted lifetimes from the global fit of three MAAs	106
Table 5.2 Calculated ground state relative energies of <i>o</i> - <i>E,E</i> -DPD and <i>m</i> - <i>E,E</i> -DPD substituted species	114
Table 5.3 Extracted lifetimes from the global fit of <i>o</i> - <i>E,E</i> -DPD and <i>m</i> - <i>E,E</i> -DPD ...	116

List of Abbreviations

ACyO	3-aminocyclohex-2-en-1-one
BBO	β -Barium Borate
CaF ₂	Calcium Fluoride
CASSCF	Complete Active Space Self Consistent Field
CASSCF/PT2	CASSCF 2 nd Order Perturbation Theory
CI	Conical Intersection
CPA	Chirp Pulse Amplification
DFT	Density Functional Theory
EADS	Evolutionary Associated Difference Spectra
<i>E</i> -EHMC	2-Ethylhexyl- <i>E</i> -4-Methoxycinnamate
<i>E</i> -MMC	Methyl- <i>E</i> -4-Methoxycinnamate
ESA	Excited State Absorption
eV	Electron Volts
FDA	Food and Drug Administration
fs	Femtosecond
FWHM	Full width Half Maximum
GSB	Ground State Bleach
IC	Internal Conversion
IET	Intermolecular Energy Transfer
IPTG	Isopropyl β -D-1-Thiogalactopyranoside
ISC	Intersystem Crossing
IVR	Intramolecular Vibrational Energy Redistribution
kHz	Kilohertz
KOALA	Kinetics Observed After Light Absorption
MAAs	Mycosporine-like Amino Acids
<i>m-E,E</i> -DPD	Dimethyl 3,3'-(1,3-Phenylene)(2 <i>E</i> ,2' <i>E</i>)-Diacylate
MHz	Megahertz

nm	Nanometres
NN	(Z)-N-(3-(Butylamino)-2-Methylcyclohex-2-en-1-ylidene)Butan-1-aminium 4-Methylbenzenesulfonate
ns	Nanosecond
OD	Optical Density
OD ₆₀₀	Optical Density at 600 nm
<i>o</i> - <i>E,E</i> -DPD	Dimethyl 3,3'-(1,2-Phenylene)(2 <i>E</i> ,2' <i>E</i>)-Diacrylate
OPA	Optical Parametric Amplification
<i>p</i> - <i>E,E</i> -DPD	Dimethyl 3,3'-(1,4-Phenylene)(2 <i>E</i> ,2' <i>E</i>)-Diacrylate
<i>p</i> - <i>E,Z</i> -DPD	Dimethyl 3,3'-(1,4-Phenylene)(2 <i>Z</i> ,2' <i>E</i>)-Diacrylate
PECs	Potential Energy Cuts
ps	picoseconds
<i>p</i> - <i>Z,Z</i> -DPD	Dimethyl 3,3'-(1,4-Phenylene)(2 <i>Z</i> ,2' <i>Z</i>)-Diacrylate
s	seconds
SCF	Self Consistent Field
SE	Stimulated Emission
SPF	Sun Protection Factor
TAS	Transient Absorption Spectrum
TD-DFT	Time Dependent Density Functional Theory
TEAS	Transient Electronic Absorption Spectroscopy
UV	Ultraviolet
UVA	Ultraviolet-A
UVB	Ultraviolet-B
UVC	Ultraviolet-C
UVR	Ultraviolet Radiation
Z-EHMC	2-Ethylhexyl- <i>Z</i> -4-Methoxycinnamate

Acknowledgements

I wish to express the deepest thanks and appreciation to my supervisor, Professor Vas Stavros. Firstly for the continuous support and encouragement at any time, even at 7 am waiting for the gym to open. Secondly, for assembling such a great team for me to have the opportunity to work with over the last four years.

As I have already mentioned every member ‘Team Stavros’ has made each day here enjoyable. However special thanks must go to Dr’s Michael ‘Mick’ Staniforth and Michael ‘Mitch’ Horbury for helping me find my feet, their own special way of support and encouragement was always helpful. Alongside Dr Nat Rodrigues Lopes for helping me with all the things a PhD student should be doing and also Mr Matthew Turner for trying to teach me computational chemistry and the engaging chats throughout my PhD. Additionally I would like to thank all the members of the Stavros group; Abbie, Adam, Daniel, Emily, Konstantina, Martin, Sofia, and Tosin for all the helpful office discussions. I also wish to extend my thanks to all the masters’ students who I have worked with during my time here: Jack, Abbie, Sofia, and Michelle. Finally all the collaborators who have worked with me; Professor Martin Wills, Dr Guy Clarkson, Dr Gareth Ritchings, Dr James Lloyd-Hughes, Dr Christophe Corre, Ms Nazia Auckloo and Mr Rod Wesson.

None of this would have been possible without the support of my family and friends who have provided many helpful distractions and cakes over the last few years. I especially want to thank my brother George for all the adventures we have had in the National Parks.

Finally I wish to thank one-pot cooking that has kept me going over the last few years, the silence of the National Parks when I need to get away from it all, and fish and chips on a Friday.

Declarations

This thesis is submitted to the University of Warwick in support of my application for the degree of Doctor of Philosophy. It has been composed by myself and has not been submitted in any previous application for any degree. The work presented (including data generated and data analysis) was carried out by the author except in the cases outlined below:

Chapter 1: The literature review in Section 1.3.1 has been published in:

J. M. Woolley, V. G. Stavros, Unravelling Photoprotection in Microbial Natural Products, *Science Progress.*, 2019, **102**, 1-17.

Chapter 3: The work presented here was published in:

J. M. Woolley, M. Staniforth, M. D. Horbury, G. W. Richings, M. Wills and V. G. Stavros, Unravelling the Photoprotection Properties of Mycosporine Amino Acid Motifs, *J. Phys. Chem. Lett.*, 2018, **9**, 3043–3048.

Synthesis of NN was performed by Professor Martin Wills, while the CASSCF calculations in Table 3.1 of ACyO were performed by Dr Gareth Richings.

Chapter 4: The work presented here was published in:

J.M. Woolley, J.S. Peters, M.A.P. Turner, G.J. Clarkson, M.D. Horbury and V.G. Stavros, The Role of Symmetric Functionalisation on Photoisomerisation of a UV Commercial Chemical Filter, *Phys. Chem. Chem. Phys.*, 2019, **21**, 14350-14356.

Synthesis of *p-E,E*-DPD was performed by Mr Jack Peters and Dr Guy Clarkson. TD-DFT calculations in Table 4.1 were performed by Mr Matthew Turner.

Chapter 5:

Biosynthesis of MAAs was performed by Ms Nazia Auckloo. Synthesis of *o-E,E*-DPD and *m-E,E*-DPD was performed by Ms Michelle Chan and Dr Guy Clarkson. DFT calculations in Table 5.2 were performed by Ms Sofia Goia and Mr Matthew Turner.

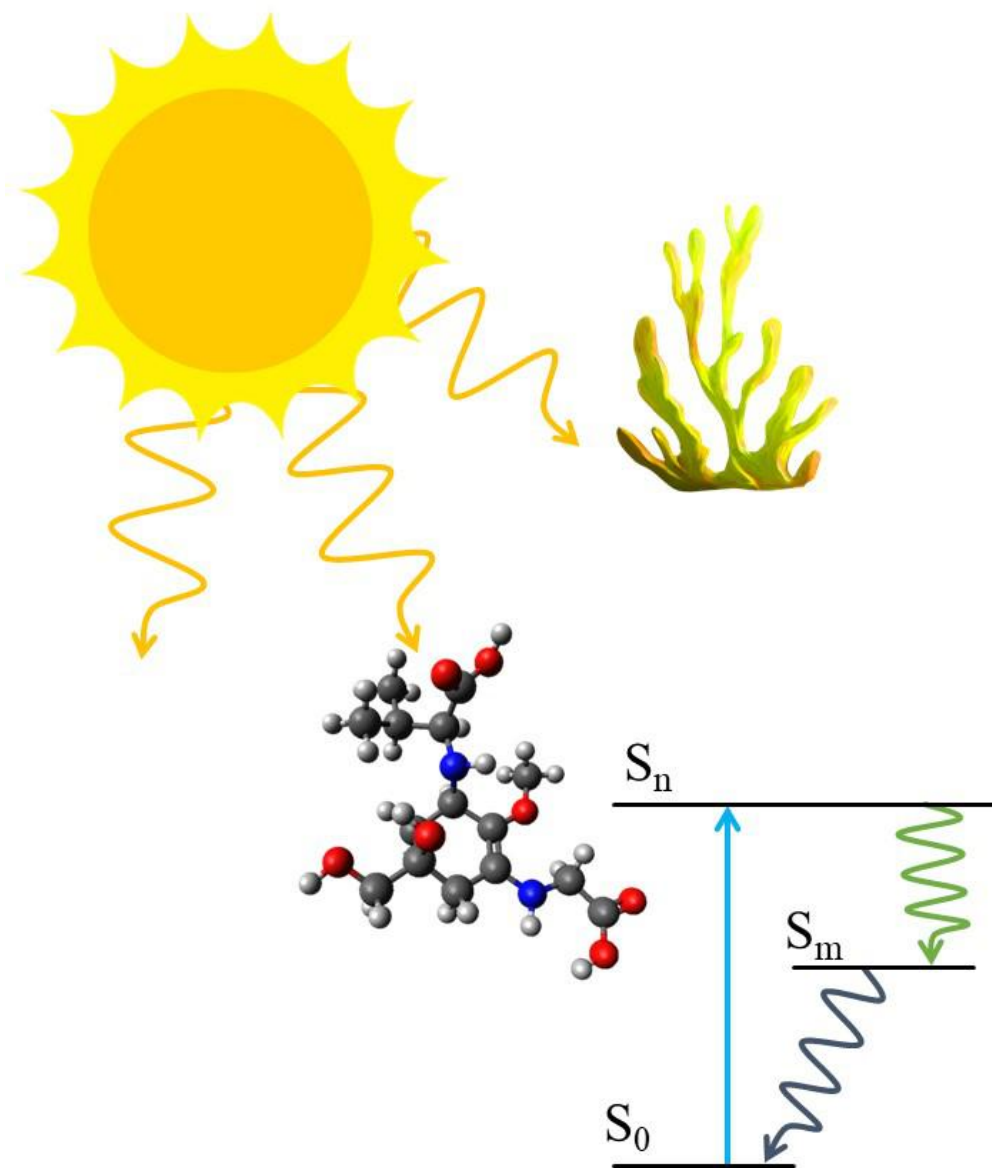
Abstract

Ultraviolet radiation (UVR) has both positive and negative effects on biological systems. In humans, for example, UVR is responsible for producing vitamin D, while excessive exposure to UVR increases the risk of skin cancer. To avoid photodamage, both plants and humans have developed molecular species to deal with any excessive UVR. Two such classes of molecular species in plants are mycosporine-like amino acids and sinapates. Both these species have previously been investigated for their ability to provide protection from UVR and they have been proposed to be the next generation of UV filters to be utilised in commercial sunscreen formulations.

The work presented in this thesis builds on the current literature on both mycosporine-like amino acids and cinnamates, a family of molecules structurally similar to sinapates, and currently employed in commercial formulations. The work presented in Chapter 3 discusses the photodynamics of mycosporine-like amino acids motifs, the results of which are used to aid the discussion in Chapter 5 on the photodynamics of natural mycosporine-like amino acids themselves. Chapter 4 published work exploring the structure-dynamics-function relationship for a symmetrically functionalised methyl cinnamate. Again these results are utilised to further explore this relationship in Chapter 5 through additional functionalisation of the methyl cinnamate moiety. All of these experiments were performed on an ultrafast transient electronic absorption setup, the details of which are described in Chapter 2.

By conducting studies aiming to understand the intrinsic molecular motions involved in photoprotection like those discussed in this thesis, it is hoped that we can then begin to utilise such structure-dynamics-function approaches to design next generation UV filters that are nature inspired.

1 Introduction



Parts of this Chapter are based on the following publication:

J. M. Woolley, V. G. Stavros, Unravelling Photoprotection in Microbial Natural Products, *Science Progress*, 2019, **102**, 1-17.

“Prior preparation prevents poor performance” **James Baker.**

1.1 Photoprotection

1.1.1 Solar Radiation and the Atmosphere

The Sun emits radiation across the electromagnetic spectrum, ranging from high energy X-rays (10-0.001 nm) to low energy radio waves (100-10 m).¹ Ultraviolet radiation is defined as the region of the electromagnetic spectrum between 400 and 10 nm.¹ The highest energy portion of the UV to reach the Earth is 280-10 nm, which contains the ultraviolet-C 280-100 nm (UVC), far and extreme ultraviolet 200-122 nm and 122-10 nm respectively.¹ The 280-10 nm region of the ultraviolet spectrum is prevented from reaching the Earth's surface by the molecular composition of the upper atmosphere.^{2,3} The regions transmitted through the atmosphere cover the remaining portion of the ultraviolet spectrum and into the visible and infrared. These transmitted regions can be further separated into ultraviolet-B, 315-280 nm (UVB) and ultraviolet-A, 400-315 nm (UVA). From this point on, both UVA and UVB will be described together as ultraviolet radiation, and abbreviated henceforth as UVR. The interactions of UVR with matter form the main discussion for the rest of this thesis. Figure 1.1 shows the penetration depth of each spectral region of ultraviolet and visible light spectrum (400-760 nm) alongside the solar spectrum incident on the Earth's atmosphere and surface.^{4,5}

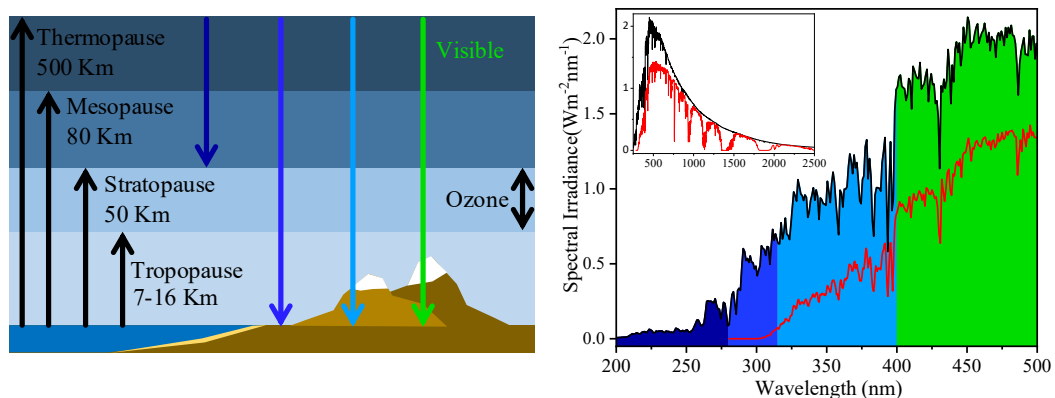


Figure 1.1 Left: schematic of the Earth's atmosphere showing penetration depth of each region of ultraviolet and visible light. Right: Solar spectrum incident on the Earth's atmosphere shown in black, and the spectrum reaching the Earth's surface shown in red. Colours distinguish the spectral regions. Data for the solar spectrum acquired from reference 5.

The layered protection given by the atmosphere is critical as allowing high energy photons to impact the Earth's surface will result in the denaturing of critical molecules, including DNA and proteins in animals, along with reducing growth rates in plants and algae.⁶⁻¹⁰ However, there are positives to the irradiation of the Earth's surface. Processes such as Vitamin D production in certain mammals and photosynthesis rely

on photoactivation.¹⁰⁻¹⁴ As such there needs to be a balance between under and over exposure to UVR.¹⁵

1.1.2 Human Photoprotection

As discussed above, there is a balance that needs to be maintained between under and over exposure to UVR, given that either too much or too little exposure can result in health concerns to humans and damage to plant life.^{9,12,14,16-18} To cope with the levels of (potentially) damaging UVR, molecules capable of absorbing and dissipating harmful energy are produced by many species on Earth.^{6,16,19,20} In humans, this role of photoprotection is taken by a class of compounds called melanins.²¹⁻²³ Melanins provide protection through pigmentation of the skin in the epidermal layer.²⁴ Pigments are produced in two main chemical forms: pheomelanin and eumelanin, both providing pigmentation and hence protection to the skin against UVR.^{24,25} Eumelanin is a darker pigment and provides better absorption of UVR than pheomelanin, leading to fairer skinned individuals (those with less eumelanin) being more susceptible to skin damage from UVR.²⁶ Additionally differing environmental effects account for different levels of pigmentation; in geological regions of higher incident UVR humans require higher quantities of melanins within the skin to afford optimum photoprotection.^{24,27,28} Further to the generation of melanin pigments for photoprotection, DNA itself has also designed repair mechanisms. The absorption of UVB radiation by DNA bases can generate photolesions within the polymeric DNA which, if left unrepaired, can be reproduced to form mutations and potentially cancer.^{29,30}

On occasions when an abnormal quantity of UVR is detected by the body, its natural response is to increase production of melanins.³¹ This process, commonly referred to as tanning, occurs over several days.³²⁻³⁴ During the time taken to produce sufficient melanin pigments, damage to DNA could already have occurred. Therefore, to supplement the body's UVR defence mechanism, cosmeceutical products with UV filters can be used to aid the natural photoprotection afforded by melanins.^{35,36}

1.1.3 Sunscreens

A way to support natural photoprotection mechanisms is through the use of light absorbing chemicals to prevent the harmful UVR from reaching the skin, *i.e.* sunscreens.³⁵⁻³⁷ Currently, there are numerous cosmeceutical products available

offering UVR protection, all of which will contain differing proportions of UV filters (Figure 1.2) approved by regulatory bodies such as the United States Food and Drug Administration (FDA) and European Union (EU). To fully protect across the UVA and UVB spectral regions, these filters are often combined together in formulations to fully protect across the UVA and UVB spectral regions.

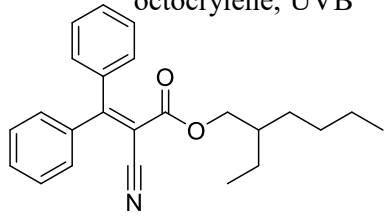
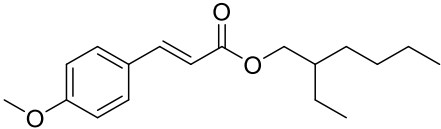
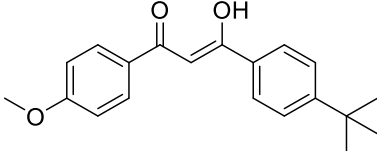
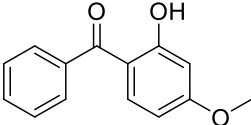
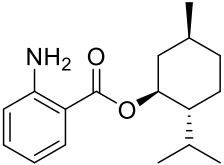
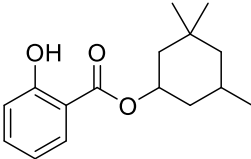
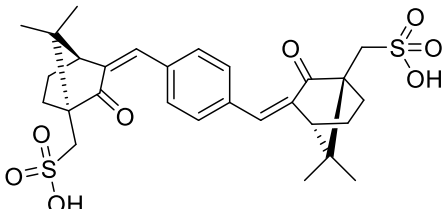
<p>octocrylene, UVB</p> 	<p>ethylhexyl methoxycinnamate, UVB</p> 																									
<p>avobenzene, UVA</p> 	<p>oxybenzone, UVB</p> 																									
<p>menthyl anthranilate, UVB</p> 	<p>homosalate, UVB</p> 																									
<p>ecamsule, UVA</p> 	<table border="1"> <thead> <tr> <th>Filter</th> <th>US</th> <th>EU</th> </tr> </thead> <tbody> <tr> <td>octocrylene</td> <td>✓</td> <td>✓</td> </tr> <tr> <td>ethylhexyl methoxycinnamate</td> <td>✓</td> <td>✓</td> </tr> <tr> <td>avobenzene</td> <td>✓</td> <td>✓</td> </tr> <tr> <td>oxybenzone</td> <td>✓</td> <td>✓</td> </tr> <tr> <td>menthyl anthranilate</td> <td>✓</td> <td>✗</td> </tr> <tr> <td>homosalate</td> <td>✓</td> <td>✓</td> </tr> <tr> <td>ecamsule</td> <td>✗</td> <td>✓</td> </tr> </tbody> </table>		Filter	US	EU	octocrylene	✓	✓	ethylhexyl methoxycinnamate	✓	✓	avobenzene	✓	✓	oxybenzone	✓	✓	menthyl anthranilate	✓	✗	homosalate	✓	✓	ecamsule	✗	✓
Filter	US	EU																								
octocrylene	✓	✓																								
ethylhexyl methoxycinnamate	✓	✓																								
avobenzene	✓	✓																								
oxybenzone	✓	✓																								
menthyl anthranilate	✓	✗																								
homosalate	✓	✓																								
ecamsule	✗	✓																								

Figure 1.2 Chemical structures of common UV filters and which region of the electromagnetic spectrum they protect. The inset table shows the approval status for each UV filter in both the US and EU.

To provide information on the photoprotection offered by sunscreens (more specifically UV filters), two separate scales exist for UVB and UVA protection. For UVB protection the Sun Protection Factor (SPF) is used to measure how long the erythema (redness) of skin takes to respond when exposed to a solar simulator both with and without a sunscreen application. The SPF is then the ratio between these two doses of UV light administered. SPF values range from 5 to 50 depending on the concentration of the UV filters employed in the formulation.³⁸ UVA protection is measured by the critical wavelength;³⁹ defined as the wavelength at which 90% of the

integrated absorption occurs, between 290 nm and 400 nm.^{40,41} A critical wavelength of longer than 370 nm is said to provide broad spectrum coverage.³⁹ While these tests provide data in a simple manner to consumers, they do have their drawbacks. These tests are carried out in an *in-vitro* environment using the prescribed dosage of 2 mg/cm². In reality, there is a large variation on the SPF value depending on the amount which is typically applied.³⁸ Research has shown that the actual coverage applied by the consumer ranges between 0.5 – 1 mg/cm².^{40,42} Furthermore, there is little understanding obtained through such testing of the intrinsic molecular dynamics occurring.⁴⁰

The measurements of SPF and critical wavelength provide an insight into the ability of UV filters to absorb UVR. This is one of three key properties required of UV filters.^{43,44} The second property is that they dissipate the absorbed energy in a radiationless decay fashion to the electronic ground state, (see Section 1.2.2 for details on how molecules dissipate energy). Rapid relaxation from the excited electronic state is beneficial to UV filters as the probability for either *intra* or *inter* molecular side reactions is minimised with the reduced time spent in a higher energy electronic state. Finally, UV filters should be able to repeat this deactivation process without a decrease in their UVR absorbance.⁴⁵ This photostability under UVR irradiation is key to UV filters as sunscreens are often applied only once or twice throughout the day by consumers,⁴⁶ even with the guidance suggesting re-application every two hours.⁴⁷ These three principles are the key photochemical properties expected of UV filters, there are however additional demands expected by both consumers and cosmetic companies such as feel and application methods onto the skin. While these concerns are secondary to the photochemical properties in the development of new UV filters, they do present the ability to effect the photodynamics of UV filters. Such effects may obstruct the effective relaxation pathways observed in a weakly interacting solvent environment in a laboratory setting. As such there has been recent impetus to develop the existing spectroscopic methods to include the effects of both the environment and the skin itself.⁴⁸

A large catalogue of UV filters which provide protection across the UVA and UVB spectral regions is already in use.⁴⁹ However, recently there have been many reports pertaining to health and safety issues over of several commonly used UV filters, including their role in endocrine disruption and their ability to act as photoallergens.⁵⁰⁻

⁵⁴ Furthermore, oxybenzone and 2-ethylhexyl-*E*-4-methoxycinnamate, both very common UVB absorbers, (shown in Figure 1.2), have been shown to cause bleaching of coral,^{55–58} culminating in the banning of sunscreen products containing these UV filters in Hawaii from 2021.⁵⁶ Due to these reports, there has been considerable impetus to use naturally abundant molecules as the next generation of UV filters.

1.2 Molecular Photochemistry

UV filters provide photoprotection through dissipation of the energy gained by absorption of electromagnetic radiation. As such, an understanding of the mechanisms through which molecules absorb and dissipate energy is essential. This section will highlight the fundamental principles involved in such processes from a quantum mechanical perspective, followed by an overview of the relaxation mechanisms available to molecules in excited electronic states.

1.2.1 Fundamental Principles

1.2.1.1 Schrödinger Equation

For any quantum mechanical system, a wavefunction, $\psi(\mathbf{R}, \mathbf{r})$, can be written to fully describe the system. Such a wavefunction will contain information relating to the energy of the molecule at a given time.^{59,60} In 1926 Erwin Schrödinger proposed that the energy of a system, E , can be calculated through knowing the wavefunction, $\psi(\mathbf{R}, \mathbf{r})$, as a function of nuclear position, \mathbf{R} , electron position, \mathbf{r} , and the appropriate Hamiltonian, \hat{H}

$$\hat{H}\psi(\mathbf{R}, \mathbf{r}) = E\psi(\mathbf{R}, \mathbf{r}). \quad (1.1)$$

The Hamiltonian \hat{H} describes the total energy of the system,⁶¹ and by making use of the Born-Oppenheimer approximation can be separated into a sum of the kinetic and potential energies of both the nuclei and electrons,

$$\hat{H} = T_n(\mathbf{R}) + T_e(\mathbf{r}) + V_{nn}(\mathbf{R}) + V_{ne}(\mathbf{R}, \mathbf{r}) + V_{ee}(\mathbf{r}), \quad (1.2)$$

where T_n and T_e are the kinetic energy operators of both the nuclei and electrons respectively, and V_{nn} , V_{ne} and V_{ee} are the potential energy operators for nuclear-nuclear, nuclear-electron and electron-electron interactions, respectively. The Born-Oppenheimer approximation states that the nuclear and electronic motion can be

considered separately due to the timescales at which the motion occurs, with the motion of electrons being much faster than nuclei, owing to their considerably lighter mass.^{3,62,63} The wavefunction can also be written separately for nuclear and electronic coordinates.^{3,62,63} through the Born-Oppenheimer approximation,

$$\psi(\mathbf{R}, \mathbf{r}) = \psi_n(\mathbf{R})\psi_e(\mathbf{R}, \mathbf{r}). \quad (1.3)$$

Combining Equations 1.2 and 1.3 with the Equation 1.1 allows two equations to be constructed, linking electronic and nuclear wavefunctions with energy shown in Equation 1.4 and 1.5 respectively.

$$[T_e(\mathbf{r}) + V_{ne}(\mathbf{R}, \mathbf{r}) + V_{ee}(\mathbf{r})]\psi_e(\mathbf{R}, \mathbf{r}) = E_e(\mathbf{R})\psi_e(\mathbf{R}, \mathbf{r}) \quad (1.4)$$

$$[T_n(\mathbf{R}) + V_{nn}(\mathbf{R}) + E_e(\mathbf{R})]\psi_n(\mathbf{R}) = E_n(\mathbf{R})\psi_n(\mathbf{R}) \quad (1.5)$$

The Born-Oppenheimer approximation again allows for the separation of coordinates as each term operates on either the nuclear coordinate, \mathbf{R} , or the electronic coordinate, \mathbf{r} . The nuclear-electron potential, $V_{ne}(\mathbf{R}, \mathbf{r})$, acts on both the nuclear and electronic coordinates. However, as these equations apply to a fixed nuclear coordinate, \mathbf{R} can be considered constant for a given nuclear position. The electronic energy, $E_e(\mathbf{R})$, and the nuclear potential, $V_{nn}(\mathbf{R})$, combined give the potential energy of the system, $V(\mathbf{R})$, for a fixed nuclear geometry. By varying one nuclear coordinate while all other nuclear coordinates within the molecule remain constant, the potential energy along that coordinate can be displayed as Potential Energy Cuts (PECs). The potential energy of a nonlinear molecule of N atoms can be given on a $3N - 6$ dimensional surface, where each dimension relates to a vibrational degree of freedom in the molecule.¹ These Potential Energy Surfaces (PESs) and more often PECs along relevant coordinates can be used to visualise molecular dynamics and aid interpretations of experimental data.⁶⁴

1.2.1.2 Transition Dipole Moment

Electronic transitions in molecules are driven by the absorption of light which leads to a transition between an initial state i and a final state f . The transition has a probability proportional to the transition dipole moment,^{60,65}

$$p(\text{abs}) \propto |\mu_{fi}|^2. \quad (1.6)$$

¹ For a linear molecule this is reduced to a $3N - 5$ dimensional surface.⁶³

Here μ_{fi} is the transition dipole moment between states f and i . The transition dipole moment is given by^{3,60,63}

$$\mu_{fi} = \int \psi_f^* \hat{\mu} \psi_i d\tau, \quad (1.7)$$

where $\hat{\mu}$ is the electric dipole operator and, ψ_i and ψ_f^* define the wavefunction of the initial state and complex conjugate of the final state respectively across all space $d\tau$. Again through application of the Born-Oppenheimer approximation, these wavefunctions can be split into the nuclear and electronic components leading to a modified form of Equation 1.7,^{3,60,63}

$$\mu_{fi} = \int \psi_{e,f}^* \hat{\mu} \psi_{e,i} d\tau \int \psi_{n,f}^* \psi_{n,i} dR. \quad (1.8)$$

In the above equation, the first integral defines the electronic spatial overlap of the wavefunctions and their interaction with the electric dipole operator. The second integral relates to the nuclear position of the ground and excited electronic states, referred to as the Franck-Condon factor.⁶³

1.2.1.3 Franck-Condon Principle

Through evaluation of the transition dipole moment, there is an observed dependence on the nuclear wavefunction of both the ground and the excited electronic state, as depicted by Equation 1.8. Quantitatively, this can be described as the overlap between the initial and final nuclear wavefunction. A larger overlap between the final, v'_n , and initial, v''_m wavefunction will give a larger transition probability compared to two states which share no overlap. In the case of Figure 1.3, the greatest overlap is between $v'_3 \leftarrow v''_0$ while a transition to the state v'_0 is less likely due to the poor overlap.^{63,66,67} Transitions which involve a change in both electronic and vibrational state such as the $v'_3 \leftarrow v''_0$ transition in Figure 1.3 are defined as vibronic transitions.

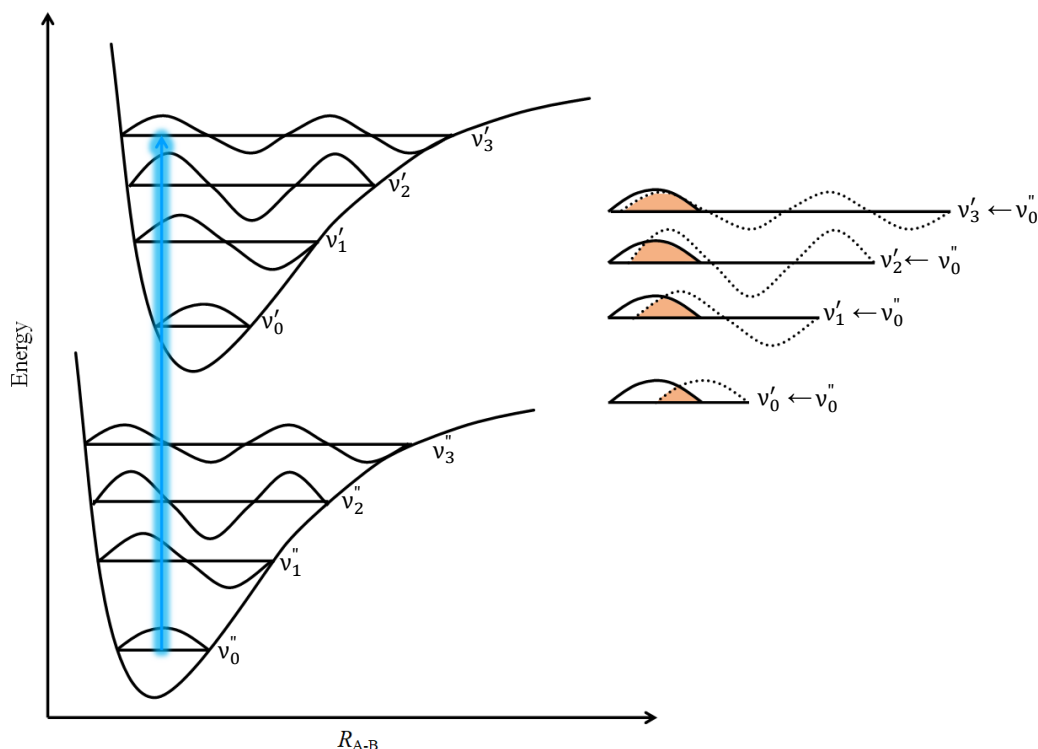


Figure 1.3 Graphical representation of Franck-Condon principle for a potential energy along bond coordinate R_{A-B} . Inset demonstrates the overlap (highlighted in orange) between the ground vibrational state v''_0 (full lines) and the excited vibrational states v'_n (dotted lines). v'_n and v''_n refer, respectively, to vibrational states in the excited electronic and ground electronic states.

1.2.1.4 Uncertainty Principle

Two complementary observables such as position, x , and momentum, p , cannot simultaneously be observed with absolute precision as their quantum mechanical operators do not commute, that is $[\hat{A}\hat{B}] \neq \hat{A}\hat{B} - \hat{B}\hat{A}$, if \hat{A} and \hat{B} are operators of observables a and b . This means that the minimum observed uncertainty across both the momentum or position of a particle is given by^{61,63}

$$\Delta p \Delta x \geq \hbar/2. \quad (1.9)$$

Here Δp and Δx is the uncertainty in momentum and position respectively and \hbar is the reduced Planck's constant. While this is the common form of the uncertainty principle, any two non-commutable operators of observables will have an uncertainty relationship.⁶³ A similar relationship between energy and time exists, leading to the same description of the uncertainty in the energy and time, ΔE , and Δt respectively. Due to this energy time uncertainty, a large spectral bandwidth (ΔE) is required to generate ultrafast femtosecond pulses (fs, $1 \text{ fs} = 1 \times 10^{-15} \text{ s}$, see Chapter 2 for more

details on femtosecond pulse generation). Assuming that the laser pulses are Gaussian in nature, the energy-time relationship can be written as

$$\Delta\nu = \frac{0.441}{c\tau_p}. \quad (1.10)$$

Here $\Delta\nu$ is the full width half maximum (FWHM) of the energy (spectral bandwidth) in wavenumbers, and τ_p is the FWHM in seconds of the pulse, with c being the speed of light in cm s^{-1} . Consequently, to generate pulses of 40 fs, $\Delta\nu$ is 368 cm^{-1} . This frequency range is large enough to excite multiple vibronic transitions within one pulse, creating a non-stationary state (wavepacket) of differing vibrational states on the PES of the molecule. So, while ultrafast pulses are ideal for observing molecular dynamics, the increased time resolution they provide inherently reduces the spectral resolution.

1.2.1.5 Conical Intersections

Conical intersections are a consequence of the break down in the Born-Oppenheimer approximation, when the nuclear and electronic motion can no longer be decoupled.^{68,69} These intersections allows for the efficient conversion between two electronic states as they approach a degeneracy in energy. Their presence depends on both the initial conditions of the system and the potential energy surfaces themselves, because of this it is required to describe them using the time-dependent Schrödinger equation.⁶⁸

$$[T_n(\mathbf{R}) + U - \Lambda]\psi_n(\mathbf{R}) = i\hbar \frac{\partial \psi_n}{\partial t}. \quad (1.11)$$

Where, $T_n(\mathbf{R})$ is the nuclear kinetic energy operator, U is a matrix representing the potential energy surfaces of the molecule, $\psi_n(\mathbf{R})$ is the nuclear wavefunction and Λ is the matrix of nonadiabatic coupling operators. By considering just two electronic states, i and f (where $i \neq f$), described by the electronic wavefunctions $\psi_{e,i}(\mathbf{R}, \mathbf{r})$ and $\psi_{e,f}(\mathbf{R}, \mathbf{r})$ the nonadiabatic coupling, $A_{i,f}$ is given by:

$$A_{i,f} = \frac{1}{2M} (2\mathbf{F}_{i,f} \cdot \nabla - G_{i,f}). \quad (1.12)$$

Here M is a suitable mass scale, ∇ is the derivative operator with respect to the nuclear coordinates. The terms $\mathbf{F}_{i,f}$ and $G_{i,f}$ are the derivative coupling vector and the scalar coupling respectively defined in bra-ket notation as:

$$\mathbf{F}_{i,f} = \frac{\langle \psi_{e,i}(\mathbf{R}, \mathbf{r}) | \nabla \hat{H}_{el} | \psi_{e,f}(\mathbf{R}, \mathbf{r}) \rangle}{\Delta E_{i,f}}, \quad (1.13)$$

and

$$\mathbf{G}_{i,f} = \langle \psi_{e,i}(\mathbf{R}, \mathbf{r}) | \nabla^2 \psi_{e,f}(\mathbf{R}, \mathbf{r}) \rangle. \quad (1.14)$$

Where \hat{H}_{el} is the electronic Hamiltonian, $\Delta E_{i,f}$ is the energy difference between the two electronic states i and f and ∇ is the Laplacian operator. As can be seen for Equation 1.13 the derivative coupling between the two electronic states is inversely proportional to the energy difference between them, so as the two PESs converge the derivative coupling between them increases. This allows the excited state population on the PES of state i to pass to the PES of state f without losing energy.⁶⁸ Where these two PESs are degenerate the topology will resemble a double cone joined at the apices, giving the name conical intersections (Figure 1.4).⁶⁸ The plane on which the apices meet is called the branching space given by a $3N - 8$ subset of the degrees of freedom in the molecule. For a linear molecule this leaves the remaining degrees of freedom to be one, where conical intersections cannot exist as they require two dimensions (Figure 1.4) at these points in a linear molecule avoided crossings occur.⁷⁰ For molecules with more than three atom types there is enough degrees of freedom within the molecule giving rise to the $3N - 8$ subspace. This space is spanned by two vectors \mathbf{g} and \mathbf{h} , termed the gradient difference and the non-adiabatic coupling vector

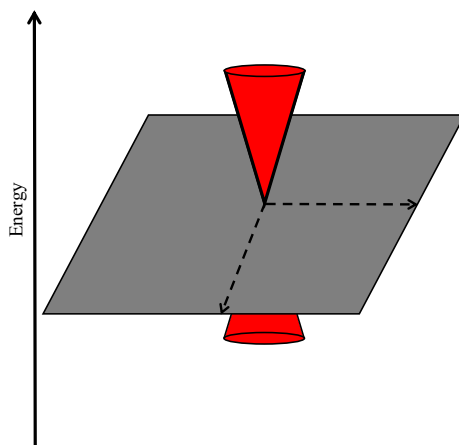


Figure 1.4 Representation of a Conical Intersection in the 2-Dimensional space.

respectively. The presence of conical intersections is difficult to observe experimentally but recent evidence has been observed through the use of two dimensional spectroscopy by monitoring the vibrational mode frequencies.⁷¹ The coupling of these two electronic states at this point on the PES allows for rapid population transfer from one electronic state to another without loss of energy this plays an important the fate of photoexcited molecules, further explored in Section 1.2.2.3.⁷²

1.2.2 Jablonski Diagram

Following the absorption of a photon, the molecule now contains excess energy for a given structural configuration. The molecule will release this excess energy to re-establish the equilibrium with the surroundings and return to the electronic ground state. This occurs either through radiative decay resulting in the release of a photon or in a nonradiative manner. Both radiative and nonradiative processes are commonly detailed on a Jablonski diagram,⁷³ such as the one displayed in Figure 1.5.

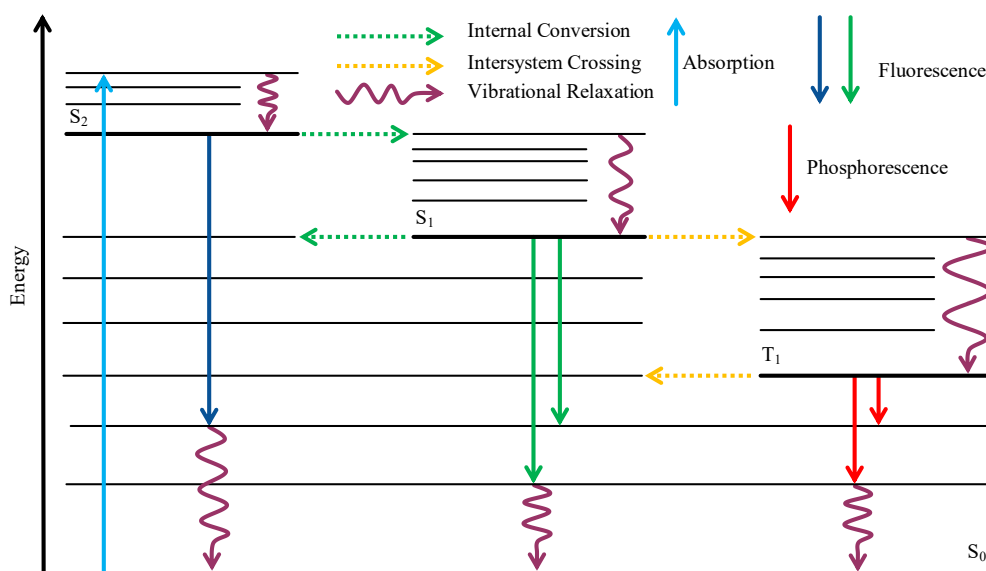


Figure 1.5 Jablonski diagram showing the relaxation pathways for a molecule electronically excited to its second singlet excited state (S_2). Thick black lines denote vibrational ground states ($\nu = 0$), while thin lines depict higher lying vibrational states ($\nu > 0$) in a given electronic state.

1.2.2.1 Absorption

In Section 1.2.1 we have provided a quantum mechanical interpretation of absorption. From a classical perspective the absorbance, A , at a given wavelength λ can be related to the intensity of the incident light, $I(\lambda)_0$, and the intensity of the light transmitted through the sample, $I(\lambda)$, by the Beer-Lambert law.⁶¹ This, in turn, is dependent on

the sample concentration, c , path length, l , and molar absorption coefficient, $\varepsilon(\lambda)$. The molar absorption coefficient here links the quantum mechanical discussion in Section 1.2.1.2 to the classically based concept discussed here.

$$A(\lambda) = \log \left[\frac{I(\lambda)_0}{I(\lambda)} \right] = \varepsilon(\lambda)cl \quad (1.15)$$

The absorption of a photon must also satisfy selection rules as well as the transition dipole moment described above. The angular momentum, l , of the overall absorption ($h\nu + \text{molecule} \rightarrow \text{molecule}^*$) must also be conserved. As a photon has an angular momentum of ± 1 ,⁶³ the change in the angular momentum of the molecule must either gain or lose a unit of angular momentum to conserve the angular momentum of the whole system. This leaves the change in angular momentum of the molecule to be $\Delta l = \pm 1$.⁷² Finally the spin of the electron involved in the transition must remain constant for the transition.⁶³ Knowing this, the spin multiplicity, $2S + 1$, of the initial and final state must be the same. Here, S , is the sum of the individual electron spins, each taking a value of $\pm 1/2$ for a given electronic state. This thesis will focus on electronic states of two different multiplicities; singlets (S_n , $S = 0$) and triplets (T_n , $S = 1$).

Within the organic molecules studied in this thesis there are two main types of electronic excitation. The first is a $\pi\pi^*$ transition where an electron located in a π molecular orbital is promoted to a molecular orbital with π^* character. Transitions of this type play an important role in the photochemistry of UV filters as they have a strong absorption coefficient and the energy between the two states typically lies within the UV region of the electromagnetic spectrum. The second source of transition is an $n\pi^*$ transition where an electron is promoted from a non-bonding (n) molecular orbital to a π^* type orbital. Transitions of this type have weaker absorption coefficients than $\pi\pi^*$ transitions but again fall within the range of energies across the UV region of the electromagnetic spectrum. The effects of solvent environment on both these transitions is an important consideration for the development of new UV filters. $\pi\pi^*$ transitions move to lower energies (red shift) when solvent polarity is increased as the solvent stabilises the π^* molecular orbital lowering the energy between the two states. Conversely, $n\pi^*$ states move to higher energies (blue shift) when solvent polarity increases as the n molecular orbital is stabilised increasing the energy gap between the n and π^* orbitals.

1.2.2.2 Radiative Decay Pathways

Radiative decay can be considered as the inverse of absorption obeying the same selection rules, *viz.* coupling through the transition dipole moment and the Franck-Condon factor required between the two states for the transition to occur. The energy of the emitted photon will correspond to the difference in energy between the two states such that $h\nu = \Delta E$. As described above in Section 1.2.1.3, the absorption of a photon has the probability to populate a vibrationally excited state within the electronic state ($S_n (\nu \neq 0)$). Kasha's rule states that any observed emission is from the lowest vibrational state ($S_n (\nu = 0)$) (see Figure 1.5);^{72,74} this causes an emission at lower energy when compared to the absorption, a so called Stokes shift.^{3,75,76} This shift in wavelength is due to the timescale involved between competing processes; vibrational relaxation and internal conversion occur on faster timescales (typically femto- to picoseconds) than those of fluorescence and phosphorescence (typically nanoseconds to seconds), the latter two therefore often outcompeted as relaxation pathways.⁷²

Excited molecules on any state may decay through the emission of a photon to a lower energy electronic state. Emission is termed fluorescence when no change in spin multiplicity is required for the transition ($\Delta S = 0$).^{63,72} Transitions involving a change in spin multiplicity ($\Delta S \neq 0$),^{63,72} are formally forbidden through the spin selection rule. Through spin orbit coupling however, the molecules can radiatively decay to a lower lying electronic state of differing spin multiplicity.^{63,72} The forbidden nature of these transitions explains the elongated timescales of such decays (milliseconds to seconds).³ Any emissive process involving a change in spin multiplicity is described as phosphorescence.^{63,72}

1.2.2.3 Internal Conversion and Intersystem Crossing

Population transfer between two electronic states can proceed with or without a change in spin multiplicity. Where no change in multiplicity occurs, the transition is termed internal conversion (IC, green dashed arrow in Figure 1.5). This conversion occurs at CIs on the PES of the molecule and is driven by the coupling of vibrational modes between the initially excited electronic state and lower lying electronic state.⁷⁷ The rate of coupling between the two electronic states (denoted K_{IC}) is dependent on the energy gap ΔE between the electronic states shown by

$$K_{\text{IC}} \propto e^{-\Delta E/h\nu}. \quad (1.16)$$

Where ν is the vibrational frequency,⁷⁸ given the dependence on ΔE , IC occurs at an increased rate when ΔE is small, as discussed in Section 1.2.1.5.

Intersystem crossing (ISC, yellow dashed arrow in Figure 1.5) is the transfer of population from one electronic state to another with a change in spin multiplicity. As described above with phosphorescence the forbidden nature of this process reduces the rate of such a transfer.^{3,63} ISC can become favoured for systems containing heavy atoms through the increase in spin-orbit coupling between singlet and triplet states.^{3,63} Furthermore El Sayed's rule states that the rate of ISC can be increased when the two electronic states involved consist of a change in molecular orbital type.^{79,80} For example a $^1\pi\pi^*$ to $^3n\pi^*$ would occur at an increased rate to that of $^1\pi\pi^*$ to $^3\pi\pi^*$.

1.2.2.4 Vibrational Relaxation

Solution-phase vibronic transitions impart both electronic and vibrational energy to a system (Section 1.2.1.3). This excess vibrational energy has the potential to be transferred in a non-radiative manner, either through intermolecular or intramolecular processes. Intramolecular vibrational redistribution (IVR) is the removal of vibrational energy from populated vibrational modes to modes with lower or equal energy within the same molecule. The total energy of the molecule is not reduced, just that the energy is now dispersed across different vibrational modes (a vibrational bath). The rate ($k_{i,\text{bath}}$) of such dispersion is given by Fermi's golden rule,^{63,81}

$$k_{i,\text{bath}} = \frac{2\pi}{\hbar} |V_{i,\text{bath}}|^2 \rho_m. \quad (1.17)$$

Here, $|V_{i,\text{bath}}|^2$ is the strength of the transition between states i and the *bath*, and ρ_m is the density of states that are accessible. Given that the rate depends not only on the coupling between states but also the density of states, IVR naturally happens faster as the vibrational states approach a continuum assuming a consistent transition strength.

IVR redistributes the energy within the molecule such that the overall energy of the molecule remains the same. With molecules in solution, a transfer of energy can be made from the solute to the solvent through intermolecular energy transfer (IET).⁸² The rate of IET (k_{IET}) can be described by the Landau-Teller formula for an oscillator in a bath, given by,⁸³

$$k_{\text{IET}} = \frac{2 \tanh(\beta\hbar\nu/2)}{m\beta\hbar\nu} \zeta(\nu). \quad (1.18)$$

Here β is defined as $1/k_{\text{b}}T$ where k_{b} is the Boltzmann constant and T is the temperature of the system. $\zeta(\nu)$ is the friction imparted by the solvent on the vibration for a given frequency ν with m being the mass of the solute molecule. This semi-classical approach treats the interaction of two particles A and B where A is a solvent molecule in a collision with a harmonic oscillator BC, a vibrational mode within the solute molecule, which is under repulsion from the solvent A. Due to the inverse relationship between k_{IET} and the vibrational frequency ν , lower frequency modes allow for an increased rate of energy transfer between the solvent and solute.

For vibrationally excited isolated molecules in vacuum, the inherent lack of solvent bath (unless under conditions of clustering) removes the possibility for IET to occur, as such only IVR will transfer energy through the molecule.

1.2.2.5 Photodissociation

A final form of relaxation, not shown on Figure 1.5 is through the dissociation of a molecule. If the shape of the PES allows, a molecule may break chemical bonds and split into fragments. The internal energy of the system is converted into translation energy of the two fragments.⁸⁴

1.3 Spectroscopic Investigations of Sunscreens

Macroscopic measurements such as SPF, critical wavelength and photostability allow for an overview of the whole formulation of a sunscreen or a particular UV filter.⁸⁵ Fundamentally, it is the ability of an individual molecule to absorb a photon and dissipate this absorbed energy that determines these properties; the methods of energy dissipation available to photoexcited molecules have been described above in Section 1.2.2. Given this, a molecular level understanding of the relaxation mechanisms involved within a UV filter is required.⁴⁴

To fully elucidate mechanisms that allow for the favourable properties presented in Section 1.1.3 molecules are studied in isolation (vacuum) or neat solvent. Furthermore, UV filters are large many-atom structures with many interactions possible either intramolecular, or intermolecular with the surrounding ingredients

within a formulation. To reduce the complexity further, smaller subunits of the main structure are studied first before molecular complexity is increased.⁴⁴ These subunits often contain the main chromophore (light absorbing unit), or areas of the molecule where the absorption occurs. This *bottom-up approach* has proved invaluable for the study of previous systems.^{86,87}

The following sections will highlight the previously performed work on both current UV filters two possible future classes of photoprotective molecules, mycosporine-like amino acids and cinnamates. Both mycosporine-like amino acid and cinnamate derivatives will form the results and discussions for Chapters 3-5 of this thesis, with the previous work described below being used to aid interpretation of the results.

Several of the UV filters in Figure 1.2 have been previously examined to ascertain their relaxation mechanisms following photoexcitation. UV filters such as oxybenzone, homosalate, avobenzone and menthyl anthranilate have been shown to undergo *enol-keto* tautomerisation following photoexcitation.⁸⁸⁻⁹¹ For oxybenzone this tautomerisation occurs with a lifetime of approximately 100 femtoseconds (fs) following this the majority of the electronic excited state population relaxes back to the *keto* ground electronic state through an accessible S_1/S_0 CI with a lifetime of 5.2 picoseconds (ps). The remaining population, approximately 8%, forms a *trans keto* structure which can return to the initial *enol* tautomer through hydrogen transfer in the ground electronic state. From the reported studies of oxybenzone by Baker *et al.*⁸⁸ excited state proton transfer provides an ideal mechanism for efficient relaxation of the electronic excited state, with the majority of the excited population reforming the initial starting structure. A second UV filter which also possesses the ability to transfer a hydrogen is menthyl anthranilate. Studies by Rodrigues *et al.*⁸⁷ on both menthyl anthranilate and its simpler chromophore methyl anthranilate show they both display the same dynamics. This result highlights the strength of the *bottom-up approach*, as a simplification of the aliphatic structures has not affected the photodynamics. For both menthyl and methyl anthranilate the hydrogen transfer between the amine and ketone is impeded by an energy barrier in the electronic excited state. This barrier traps the electronic excited state population preventing efficient recovery back to the ground electronic state, leading to excited state lifetimes in solution of $\gg 2$ nanoseconds (ns).⁹¹ The trapping of this electronic excited state population allows the competition between internal conversion and fluorescence, indeed fluorescence quantum yields of

menthyl anthranilates have been found to be 0.64.⁹² The reports of a high quantum yield of fluorescence are contrary to the ideal photodynamics of UV filters as long lived electronic state have the potential to transfer the excess energy to the surrounding molecules possibly feeding harmful side reactions.^{93–95}

1.3.1 Mycosporine-like Amino Acids

Section 1.1.2 discussed the human body's mechanism for protection against UVR. Likewise, algae and bacteria must also regulate their exposure to UVR.^{8,96,97} To facilitate this, such micro-, and macro-organisms produce a class of UVR absorbers called mycosporine/mycosporine-like amino acids (MAAs). Mycosporines consist of a cyclohexenone core while mycosporine-like amino acids are based on a cycloheximine core with both core structures commonly substituted with a methoxy and a glycine unit at position 2, and 3 respectively, as shown in Figure 1.6. Substitutions far removed from these two positions have little effect unless a large change in conjugation is encountered,⁹⁸ resulting in a change to the overall chromophore (highlighted in red in Figure 1.6).⁹⁸ MAAs present a promising form of future UV filter given their strong UVR absorption, with typical absorption coefficients in the region of $30,000 \text{ M}^{-1} \text{ cm}^{-1}$ similar to that of *E*-EHMC of $24,000 \text{ M}^{-1} \text{ cm}^{-1}$.^{97,99} Currently, approximately 30 MAAs have been isolated which, combined, cover the UVA and UVB regions of the electromagnetic spectrum.^{97,100,101} Different functionalisation on positions 1 and 3 not only allows for variability in the ground electronic state absorption spectrum of the MAA, but is necessary for widespread commercialisation, as natural source extraction and synthetic preparation yields only small quantities of natural MAAs (typically 15 steps, 1% of overall yield).^{97,102–104}

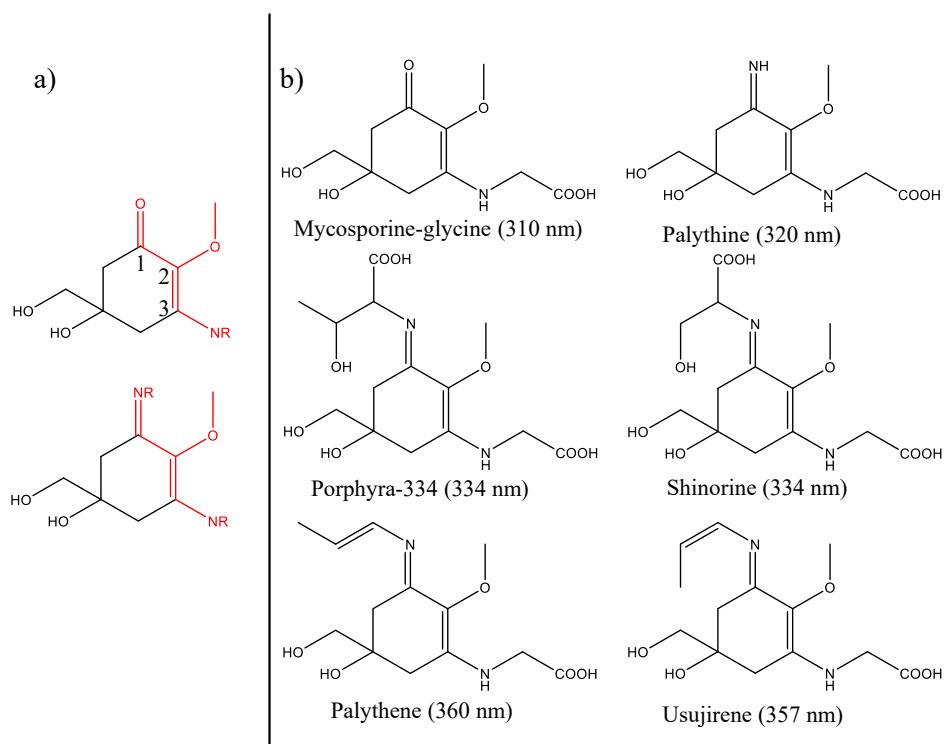


Figure 1.6 a) Core structures of mycosporine (top) and mycosporine-like amino acids (bottom). b) Common mycosporine and mycosporine-like amino acid structures along with their reported absorption maxima. Key positions have been numbered in the core structures to aid discussion.

1.3.1.1 Advances in MAA photochemistry

Given the aforementioned disadvantages of MAA synthesis and extraction, recently there has been impetus to develop simpler mimics of MAAs to allow for a largescale production for use in a cosmeceutical environment. Work by Losantos *et al.*¹⁰³ has explored the functionalisation of the core moieties of MAAs (shown in Figure 1.7) and their consequent excited state dynamics properties theoretically, through the use of CASSCF methodology (Section 1.5), in an effort to mimic the natural systems.

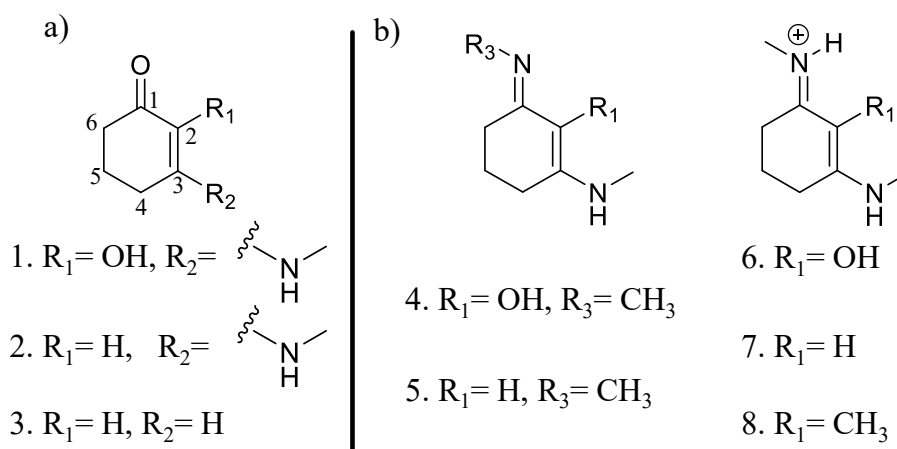


Figure 1.7 Chemical structures of systems studied by Losantos *et al.* a) cyclohexenone core structures, b) cyclohexenimine core structures; adapted from reference 103.

Importantly, the simpler chemical structures of these mimics reduces the complexity of organic synthesis compared to actual MAAs,^{102,104} while also increasing the percentage yield.¹⁰³

Employing a computational approach, Losantos *et al.* extracted key points along the minimum energy pathway (CIs and PES minima), for the core structures with differing functional groups, based upon the three cyclohexenone and five imine core structures shown in Figure 1.7. Their findings show that following photoexcitation to the second optically bright (note S_1 is optically dark), excited electronic state (S_2), MAA-inspired moieties that possess a cyclohexenone core prevent repopulation of the ground electronic state. The excited state population traverses through an S_2/S_1 CI before being trapped in the excited state minimum of the first excited electronic state (S_1). While Losantos *et al.* did locate a CI between the S_1 and ground electronic state (S_0), this is energetically inaccessible as it is located above the S_1 minimum. This is summarised by Figure 1.8.

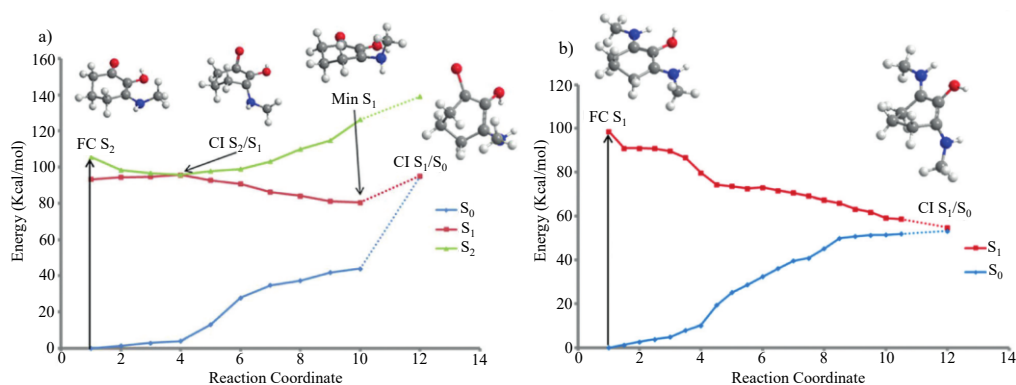


Figure 1.8 Calculated minimum energy pathways for systems studied by Losantos *et al.* a) structure 1, and b) structure 6, from Figure 1.7. Adapted from reference 103.

In contrast, MAA-inspired moieties that are formed of a cyclohexenimine core repopulate S_0 following photoexcitation, this time directly to the optically bright S_1 ; excited state population passes through an energetically accessible S_1/S_0 CI, as shown Figure 1.8. All the systems studied show that the geometry of the CI involves an out-of-plane movement for both substituents at positions 1 and 3 on the ring (see Figure 1.6). Furthermore, non-adiabatic molecular dynamics simulations conducted on molecules 6 and 8 (Figure 1.7) predict an S_1 lifetime of approximately 200 fs.¹⁰³ This lifetime is shorter than that of current UV filters such as avobenzone (Figure 1.3).^{88,90,91} The shorter excited state lifetime is beneficial to potential UV filters; the probability for competing (reactive) pathways within the UV filter itself, or side

reactions between the electronically excited sunscreen filter and additional compounds (within a commercial formulation) is minimised. These competing side reactions can also induce unfavourable reactions some of which have been known to cause skin irritation.^{50,105}

Given their findings regarding the differing core structures, Losantos *et al.* proceed to suggest 16 additional structures based upon the imine core moiety, each allowing for variation in the ground electronic state absorption to fully cover the UVA and UVB region of the electromagnetic spectrum. Losantos *et al.* also further explore the photostability and perform SPF measurements on mixtures of these systems.¹⁰³ These findings are in notable contrast to commercial formulations, as they demonstrate significant increases in SPF.

The previous study focussed on tracking the energy transfer within MAA-inspired structures using computational methods. Work by Conde *et al.*¹⁰⁶ uses photoacoustic calorimetry to follow the transfer of absorbed photon energy through intermolecular interactions between solute and solvent for two common MAAs: shinorine and porphyra-334 shown in Figure 1.6.^{106,107} Photoacoustic calorimetry provides information of energy transfer through the monitoring of pressure waves formed from both structural and thermal volume changes in the sample.^{108,109} These volume changes are initiated by a nanosecond pulsed laser. Through comparison with a known calorimetric standard, qualitative analysis of the energy transfer between the solute and solvent can be obtained.^{108,109} Photoacoustic calorimetry performed on both shinorine and porphyra-334 (both excited at 355 nm) showed equivalent values of the initial amplitude, between the solute and the reference sample, indigo carmine.¹¹⁰ This equivalence (between solute and standard) is an indication that the energy absorbed by the MAAs is rapidly released as heat to the surrounding solvent.¹⁰⁸ Conde *et al.* note that the conversion of this energy transfer (solute to solvent) is 96-98%,¹⁰⁶ leaving some residual energy trapped within the MAA which undergoes intersystem crossing to populate a triplet state. The authors confirm the presence of the triplet state for both shinorine and porphyra-334 with the use of laser flash photolysis;^{107,111} this triplet state accounts for the remaining energy trapped within the MAAs.

To corroborate their photoacoustic calorimetry measurements, Conde *et al.* performed steady-state experiments to fully describe the photostability and relaxation dynamics

of shinorine and porphyra-334. These results validate the photoacoustic calorimetry measurements with negligible fluorescence quantum yields determined, with values on the order of 10^{-4} . The rate of photodecomposition was found to be of the same magnitude, leading the authors to attribute a similar relaxation pathway as described for the MAA-inspired structures described by Losantos *et al.*¹⁰³

The authors close by placing their research in the wider field of natural sunscreens highlighting that their results strongly favour the use of both shinorine and porphyra-334 in an *in-vivo* environment as natural UV filters, even though a small proportion of the excess energy remains trapped as a triplet population with a significantly longer lifetime.^{106,107,112}

1.3.2 Cinnamates

A class of molecules that has the potential for further use in commercial formulations is cinnamates. Cinnamates consist of a phenyl ring adjoined to an acrylate moiety. The basic structure of a cinnamate is shown in Figure 1.9, along with the common chemical filter 2-ethylhexyl-*E*-4-methoxycinnamate (*E*-EHMC). *E*-EHMC is used as a UVB absorber with a maximum absorption wavelength around 300 nm in various solvents.⁸⁷ Cinnamates dissipate the energy gained from photoexcitation through an energetically accessible CI along a photoisomerisation pathway which leads to repopulation of the electronic ground state (S_0) either returning to the original *E* isomer or as a photoproduct in the *Z* isomeric form.

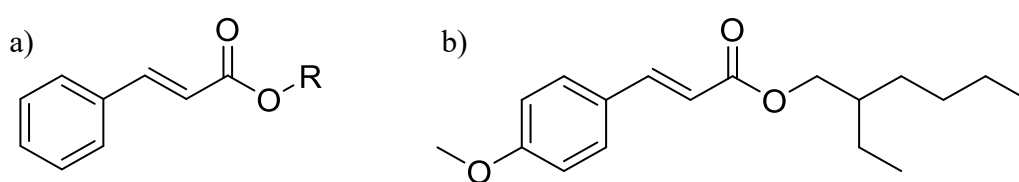


Figure 1.9 Chemical structures of a) a basic cinnamate and b) common UV filter 2-ethylhexyl-*E*-4-methoxycinnamate.

1.3.2.1 Advances in Cinnamate Photochemistry

The base structure of cinnamates (Figure 1.9a) allows for the addition of different functional groups, both around the phenyl ring and at the R group, which may affect the photodynamics. The effects of different functional groups and their positions has previously been studied by Promkatkaew *et al.*¹¹³ through the use of steady-state absorption and emission spectroscopy along with complementary computational methods. Promkatkaew *et al.* studied the effects of three functional groups (hydroxy,

nitro and fluoro) at each ring position (*ortho*, *meta* and *para*) with respect to the acrylate moiety for both the base methyl cinnamate (Figure 1.9, R= CH₃) and cinnamic acid structure (Figure 1.6, R= H). Their findings show that, for the hydroxy substituted cinnamates and cinnamic acids, there is a broad absorption band across the UVA and UVB regions, while the nitro and fluoro compounds show spectrally narrower peaks. Emission spectra were recorded for all the species studied with the emission being quenched by oxygen, from nitro and fluoro derivatives suggesting that the radiative decay involves a triplet state. In contrast, radiative decay persisted in the presence of oxygen for the hydroxy derivatives, suggesting the decay occurs through singlet states. Finally Promkatkaew *et al.* computed the PEC around the torsion of the double bond for each species, finding that the *meta* substituted derivatives have a barrier to photoisomerisation, consistent with previous reports on hydroxy and methoxy derivatives,^{114,115} compared to both the *ortho* and *para* which shows no barrier to isomerisation across the coordinate.¹¹³ The work by Promkatkaew *et al.* highlights the effect of differing substituent groups both on their ground state absorption profiles and on the relaxation dynamics.

Isomerisation as a relaxation pathway back to the ground electronic state provides a suitable pathway for UV filters, forming either the starting isomer or the isomeric form. Hanson *et al.*¹¹⁶ have studied the photoisomerisation of *E*-EHMC in both dilute solutions and thin films through the use of steady-state irradiation with a UVR simulator. From steady-state irradiation of the dilute solutions Hanson *et al.* finds that the absorbance decays before plateauing to a photostationary state within 109 seconds. The solutions retain 79% and 68% of the initial absorption for *E*-EHMC solvated methanol and cyclohexane respectively. The authors attribute this loss of absorption to formation of the *Z*-EHMC, which has a smaller absorption coefficient (12,600 M⁻¹cm⁻¹ compared to 24,000 M⁻¹cm⁻¹ of *E*-EHMC).⁹⁹ Furthermore, Hanson *et al.* are able to compute the quantum yield of *E*→*Z* photoisomerisation to be 0.37 ± 0.01 and 0.28 ± 0.01 in both methanol and cyclohexane respectively. In contrast, the *Z*→*E* photoisomerisation quantum yield was found to be 0.47 ± 0.06 and 0.60 ± 0.00 in methanol and cyclohexane.¹¹⁶ The authors rationalise the differences in the quantum yields between solvents through the polarity of methanol favouring the increased polarity of the *Z*-isomer thus stabilising it compared to the *E*-isomer.

Thin films of *E*-EHMC showed continuous degradation when exposed to UVR up to a maximum time delay of 3200 seconds. Along with the degradation, three new peaks become apparent following UVR irradiation. The authors assign two of these peaks (280 and 310 nm) to the presence of photocyclised dimers of *E*-EHMC.¹¹⁷ The third peak (400 nm) is shifted further into the UVA compared to that of *E*-EHMC. Hanson *et al.* are unable to fully resolve the chemical species responsible for the peak, but suggest that a complex mixture of dimers along with isomerisation are responsible from their HPLC and Mass spectrometry data.¹¹⁶ Finally Hanson *et al.* performed sensitised fluorescence experiments using a molecular probe, Singlet Oxygen Sensor Green (SOSG), to observe if the degradation products of the thin films could sensitise singlet oxygen. The SOSG fluorescence increased as *E*-EHMC was irradiated at 405 nm indicating that the unidentified products could sensitise singlet oxygen. This result is cause for concern due to the effects of reactive oxygen species (ROS) on biological processes.^{118,119}

Overall Hanson *et al.* show that the photostability of *E*-EHMC is dependent on the surrounding environment, between dilute solutions and concentrated thin films. In dilute solutions *E*-EHMC retains between 60 and 80 % of the initial absorbance as a photostationary state is formed between the *E* and *Z* isomers. For the thin films, irradiation with UVR shows no evidence of a photostationary state with degradation continuing up until the maximum measured time delay, with several new peaks being observed and attributed to the formation of dimers and additional photoproducts.^{116,117}

Many reports exist of ultrafast spectroscopy being used to study photoisomerisation pathways,¹²⁰⁻¹²³ including the dynamics of *E*-EHMC by Peperstraete *et al.*⁸⁷ who performed both transient electronic absorption spectroscopy (TEAS, discussed in Section 1.4.1) and gas-phase molecular beam experiments on *E*-EHMC and its simpler model methyl-*E*-4-methoxycinnamate (*E*-MMC). Focussing on their TEAS data, Peperstraete *et al.* show that both *E*-MMC and *E*-EHMC exhibit ultrafast relaxation from the initially populated excited electronic state back to the ground electronic state. Both *E*-MMC and *E*-EHMC relax to their respective ground electronic states (although some population converts to the *Z* isomer, *vide infra*) achieving a key principle required of UV filters. The authors confirm the presence of the *Z* isomer by comparing ¹H NMR spectra of *pre* and *post* irradiated samples, consistent with the reports of Hanson *et al.*¹¹⁶ that photoisomerisation forms the major relaxation

mechanism of *E*-EHMC. Molecular level spectroscopic investigations like this provide a detailed insight into the flow of energy in molecules following photoexcitation, and are a key step in understanding the role of molecular structure has in photoprotection.

1.4 Pump-Probe Spectroscopy

Spectroscopy has long been used to provide otherwise unattainable insight into the study of chemical processes.^{124,125} The use of spectroscopy to monitor the progress of fundamental chemical reactions began in the form of flash photolysis,^{126,127} a technique which still provides detailed insight into chemical processes as seen above.^{107,112} An initial flash of light (pump) activates the chemical reaction while the progression of the reaction is tracked through the absorption of a second pulse of light termed the probe. Limitations of such a system arose through the types of chemical reactions that could be studied and the temporal resolution available.

The invention of the laser in 1960 allowed for greater spectral resolution with its ability to produce monochromatic coherent light.¹²⁸ Coupled to this, the use of techniques such as mode locking allowed for greater temporal resolution up to femtosecond resolution (10^{-15} s).¹²⁹ The ability to generate fs pulses of light allowed for a revolution in the area of time-resolved spectroscopy: for the first time spectroscopists were able to probe molecular dynamics on a timescale comparable to molecular motions.¹³⁰ This ability was first demonstrated by Ahmed Zewail showing the photodissociation of isolated iodine cyanide.^{131,132} Such capabilities opened a new area of ‘Femtochemistry’ allowing for a greater understanding of molecular mechanisms and reaction dynamics.^{133,134}

1.4.1 Transient Electronic Absorption Spectroscopy

While a myriad of ultrafast spectroscopic techniques are capable of observing chemical dynamics, this thesis will focus on Transient Electronic Absorption Spectroscopy (TEAS).^{43,133,135} TEAS has been used to study the dynamics of a variety of different systems from key biological systems such as photosynthesis to charge transfer dynamics in perovskite semiconductors.^{136,137} TEAS provides an ideal technique for studying the dynamics of UV filters,^{88,91,138,139} The use of a broadband

probe allows for not only spectral features to be observed but the shifts in such features which can be used to infer dynamics of the systems under study.

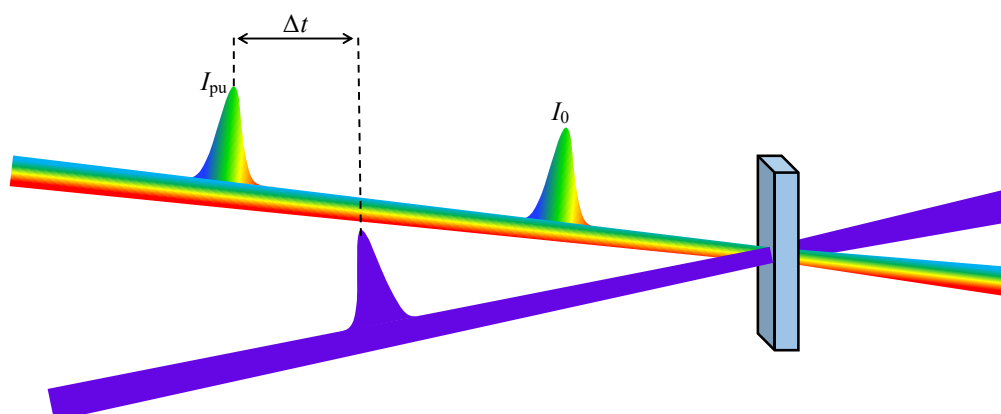


Figure 1.10 Schematic showing the pulse ordering used for transient absorption experiments conducted in this thesis. I_0 is the (intensity of the) first pulse to traverse through the sample before photoexcitation, shown in purple. The probe pulse, I_{pu} is then delayed by a time Δt before the passing through the sample.

Figure 1.10 shows the pulse ordering for transient absorption measurements. An ultrafast pump pulse, prepares the electronic excited state of the molecule. This is followed at a prescribed time delay (Δt) by the probe pulse which interrogates the molecule of interest through absorption, $I_{pu}(\lambda, t)$. The probe pulses used in this thesis are based on a broadband super continuum ranging from (320-720 nm). Changes in intensity of the probe pulse are described as changes in optical density (ΔOD , Equation 1.1), through comparison of the intensity of the probe pulse traversing photoexcited (pumped) sample denoted $I_{pu}(\lambda, t)$ and the intensity of the probe pulse traversing a non-photoexcited (unpumped) sample denoted $I_0(\lambda)$.

$$\Delta OD(\lambda, t) = \log \left[\frac{I_0(\lambda)}{I_{pu}(\lambda, t)} \right] \quad (1.19)$$

Each time delay produces a transient absorption spectrum (TAS), each TAS is composed of multiple features, either positive or negative in form, which are: ground state bleach (GSB), excited state absorption (ESA), stimulated emission (SE) and photoproduct absorption. Figure 1.11 shows how the combined signal from these processes manifest into each TAS.

What follows is an explanation of the origin of the signals observed in the TAS as these, and their evolution in time, will form the major part of the discussion in later Chapters.

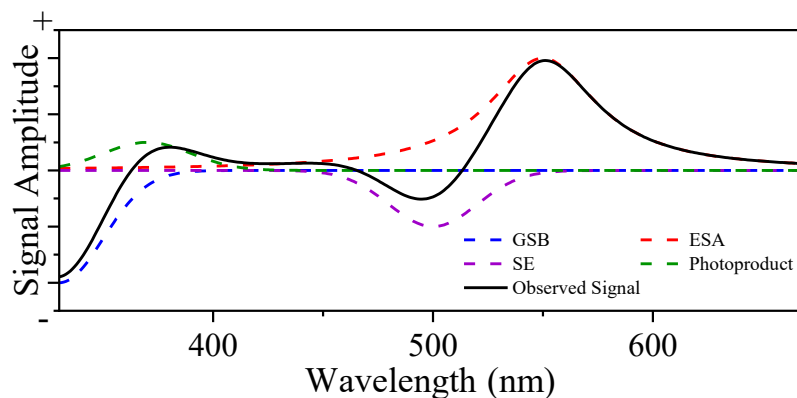


Figure 1.11 Four component signal of transient absorption spectra, added together they give the total observed signal (black trace).

1.4.1.1 Ground State Bleach (GSB)

Ground state bleach (blue dashed line in Figure 1.11) occurs as a consequence of the photoexcitation of the ground electronic state population. The excitation of population from the ground electronic state removes a proportion of the unpumped probe absorbance within that spectral region meaning, the intensity of the unpumped probe is greater than the pumped probe ($I_{\text{pu}}(\lambda_{\text{GSB}}, t) > I_0(\lambda_{\text{GSB}})$), leading to an observed negative signal. Evolution of the GSB can provide valuable insight into the relaxation dynamics: a complete GSB recovery would infer the molecule relaxes fully to its initial conditions, while incomplete recovery could be attributed to population remaining within an electronically excited state or destructive decay.

1.4.1.2 Excited State Absorption (ESA)

Molecules which are in higher lying states can also absorb light from the probe pulse and transition to even higher lying states if the transitions are allowed. If this occurs, it manifests as a positive signal (red dashed line, Figure 1.11) as the pumped probe light is depleted compared to the initial non-pumped probe pulse ($I_{\text{pu}}(\lambda_{\text{ESA}}, t) < I_0(\lambda_{\text{ESA}})$). A host of dynamical information can be extracted by monitoring the ESA as it evolves as a function of time, while the spectral shapes in each TAS can infer vibrational information from the IVR and IET processes.

1.4.1.3 Stimulated Emission (SE)

When the probe interacts with the photoexcited sample it can be absorbed as in ESA or it can induce the emission of a photon from the excited state to a lower electronic state. If the wavelengths of the probe region correspond to such a transition then a stimulated emission (SE) can be observed. In this case, the intensity of the pumped

probe pulse is greater than the non-pumped probe, generating an observed negative signal ($I_{\text{pu}}(\lambda_{\text{SE}}, t) < I_0(\lambda_{\text{SE}})$, purple dashed line in Figure 1.11). As with ESA, SE can provide vibrational information through the spectral shapes of the features in the TAS. Furthermore, because the probe region occupies energies relating to the electronic transitions SE can only be observed from an electronically excited state.

1.4.1.4 Photoproducts

Not all photochemical processes return to their initial starting position: often structural rearrangement occurs, such as photoisomerisation or photodissociation. These differing structures have the potential to give different ground state absorption profiles compared to the starting geometry. This, in turn allows for a change in the observed TAS. Typically, photoproduct (green dashed line) formation persists beyond the maximum pump-probe time delay and is observed along with a GSB feature.

1.5 Computational Chemistry

While computational chemistry is not the main discussion of this thesis, computational techniques have been used to aid discussions of results presented in the later Chapters. As such, a brief overview of the computational methods employed is given below.

Computational chemistry relies on solving the Schrödinger equation (Equation 1.1) to extract information for both the ground and excited electronic states, exact solutions require a full description of both the Hamiltonian operator and the wavefunction.¹⁴⁰ Molecular orbitals used in electronic wavefunctions are often approximated through a linear combinations of basis functions which mimic the atomic orbitals,¹⁴¹ further information on basis functions can be found in reference 141. Electronic state calculations for the ground electronic state can be considered routine for numerous systems, given a single electronic configuration.¹⁴² Challenges for electronically excited states calculations often arise from the need to consider numerous electronic configurations, as well as different ranged interactions, such as those discussed below. Intermolecular interactions (such as hydrogen bonding, clustering and aggregation) can also alter the excited electronic states of systems further to the intramolecular considerations which one encounters in vacuum. Polarizable continuum and conductor like screening models can be applied to account for the electrostatic nature of the solvent interaction.^{140,143,144} However, to fully capture the explicit nature of solvent interaction and systems such as those described above, particularly hydrogen bonding,

multiple solvation shells are regularly required along with one of the aforementioned models to achieve suitable levels of accuracy.^{130,135-137}

Ab initio methods make use of self-consistent field (SCF) methods and Hartree-Fock Slater determinants,¹⁴⁰ to define a full wavefunction for the system using a set of given orbitals and a prescribed number of electrons. A particular approach, known as complete active space self-consistent field (CASSCF), has advantages in finding CIs between excited states.^{68,148} The disadvantage of such a method is the computational cost associated with such calculations. CASSCF is also commonly employed with a Møller-Plesset perturbation (CASPT2) to aid the accuracy of calculation, however this does increase computational costs.¹⁴⁰ To avoid excessive computational cost, calculations often only involve key orbitals and electrons (often those located within chromophore molecule); reducing the number of orbitals and electrons considered reduces the quality of the result.^{142,149,150}

Additional techniques such as Density Functional Theory (DFT) provide solutions to the increased computational cost of quantum chemical methods by neglecting the many-electron wavefunction, through the knowledge that all properties of a molecule can be calculated by knowing the electron density of the molecule (Hohenberg-Kohn approach).¹⁵¹ This Hohenberg-Kohn approach relies upon knowing the perfect functional; an impossibility, as you would need to perfectly capture the electron density of the system. However, the Kohn-Sham equations allow calculations of the systems to be performed without the knowledge of the perfect functional, through the use of an exchange correlation to model the perfect functional of the system.¹⁵² Calculations of the excited electronic states can then be made through the perturbation of this result over time known as Time Dependent-DFT (TD-DFT).¹⁵³

1.6 Summary

In this Chapter we have discussed how the atmosphere both absorbs and transmits ultraviolet radiation (UVR). Transmitted UVR has been shown to act in both a beneficial and detrimental manner to natural photophysical processes. Following this, we discussed how the need for suitable molecules capable of providing protection from harmful UVR, and how two different classes of molecules, Mycosporine-like amino acids and cinnamates are being explored for future use in commercial

applications. A quantum mechanical interpretation for absorption and the relaxation mechanisms available to photoexcited molecules is given, before an overview of the experimental techniques utilised in the following Chapters of this thesis.

What follows is an in-depth description of the experimental setup, provided in Chapter 2 which paves the way for discussion of the thesis results in Chapters 3, 4 and 5. Chapter 3 utilises the *bottom-up* approach to elucidate the relaxation dynamics of MAAs. Chapter 4 focusses on the base methyl cinnamate and the effects of symmetric functionalisation. Following this, Chapter 5 describes unpublished work on natural MAAs, along with the effects of varying the positional substitution, again around a basic methyl cinnamate structure. Finally, a brief reflection on the advances made in the previous Chapters, as well as the future work made possible through these results will be discussed.

1.7 Bibliography

- 1 International Organization for Standardization, *ISO 21348 Definitions of Solar Irradiance Spectral Categories*, International Organization for Standardization, 2013.
- 2 J. P. D. Abbatt and M. J. Molina, *Annu. Rev. Energy Environ.*, 1993, **18**, 1–29.
- 3 R. C. Evans, P. Douglas and H. D. Burrows, *Applied Photochemistry*, 2014.
- 4 R. J. States and C. S. Gardner, *J. Atmos. Sci.*, 2000, **57**, 66–77.
- 5 Standard Solar Spectrum,
<https://www.pveducation.org/pvcdrom/appendices/standard-solar-spectra>,
(accessed 24 October 2018).
- 6 W. Domcke and A. Sobolewski, *Phys. Chem. Chem. Phys.*, 2010, **12**, 4897–4898.
- 7 S. Kataria, A. Jajoo and K. N. Guruprasad, *J. Photochem. Photobiol. B Biol.*, 2014, **137**, 55–66.
- 8 É. C. Schmidt, B. G. Nunes, M. Marschin and B. Z.L., *Photosynthetica*, 2010, **48**, 161–172.
- 9 A. T. Banaszak and M. P. Lesser, *Photochem. Photobiol. Sci.*, 2009, **8**, 1276–1294.
- 10 B. L. Diffey, *Phys. Med. Biol.*, 1991, **36**, 299–328.
- 11 K. L. How, H. A. Hazewinkel and J. A. Mol, *Vet. Q.*, 1995, **17**, 29.
- 12 M. J. McKenna and B. Murray, *Endocrinol. Diabetes A Probl. Approach*, 2007, **357**, 266–281.
- 13 R. E. Blankenship, *Molecular Mechanisms for Photosynthesis*, 2002.
- 14 M. Wacker and M. F. Holick, *Dermatoendocrinol.*, 2013, **5**, 51–108.
- 15 M. M. Caldwell, L. O. Björn, J. F. Bornman, S. D. Flint, G. Kulandaivelu, A. H. Teramura and M. Tevini, *J. Photochem. Photobiol. B Biol.*, 1998, **46**, 40–52.
- 16 F. R. de Gruijl, *Eur. J. Cancer*, 1999, **35**, 2003–2009.

- 17 D. F. Gleason and G. M. Wellington, *Nature*, 1993, **365**, 836–838.
- 18 B. E. Brown, *Coral Reefs*, 1997, **16**, 129–138.
- 19 G. M. Roberts and V. G. Stavros, *Chem. Sci.*, 2014, **5**, 1698.
- 20 C. E. Crespo-Hernández, B. Cohen, P. M. Hare and B. Kohler, *Chem. Rev.*, 2004, **104**, 1977–2019.
- 21 J. Borovansky and P. A. Riley, Eds., *Melanins and Melanosomes: Biosynthesis, Biogenesis, Physiological, and Pathological Functions*, Wiley Blackwell, 2011.
- 22 T. L. Diepgen and V. Mahler, *Br. J. Dermatology, Suppl.*, 2002, **146**, 7–10.
- 23 A. R. Young, *Phys. Med. Biol.*, 1997, **42**, 789–802.
- 24 J. D’Orazio, S. Jarrett, A. Amaro-Ortiz and T. Scott, *Int. J. Mol. Sci.*, 2013, **14**, 12222–12248.
- 25 S. Ito, K. Wakamatsu and H. Ozeki, *Pigment Cell Res.*, 2000, **13**, 103–109.
- 26 M. . Vincensi, M. D’Ischia, A. Napolitano, E. . Procaccini, G. Riccio, G. Monfrecola, P. Santoianni and G. Prota, *Melanoma Res.*, 1998, **8**, 53–58.
- 27 G. P. Pfeifer, Y. H. You and A. Besaratinia, *Mutat. Res. - Fundam. Mol. Mech. Mutagen.*, 2005, **571**, 19–31.
- 28 N. Kollias, R. M. Sayre, L. Zeise and M. R. Chedekel, *J. Photochem. Photobiol. B Biol*, 1991, **9**, 135–160.
- 29 D. E. Brash, *Photochem. Photobiol.*, 2015, **91**, 15–26.
- 30 R. P. Sinha and D.-P. Häder, *Photochem. Photobiol. Sci.*, 2002, **1**, 225–236.
- 31 B. A. Gilchrest and M. S. Eller, *J. Investig. Dermatology Symp. Proc.*, 1999, **4**, 35–40.
- 32 N. Agar and A. Young, *Mutantation Res.*, 2005, **571**, 121–132.
- 33 M. Brenner and V. J. Hearing, *Photochem. Photobiol.*, 2008, **84**, 539–549.
- 34 J. M. Sheehan, C. S. Potten and A. R. Young, *Photochem. Photobiol.*, 1998, **68**, 588–592.

- 35 S. Forestier, *J. Am. Acad. Dermatol.*, 2008, **58**, 133–138.
- 36 F. Urbach, *J. Photochem. Photobiol. B Biol.*, 2001, **64**, 99–104.
- 37 V. G. Stavros, *Nat. Chem.*, 2014, **6**, 955–956.
- 38 S. Schalka, V. M. S. dos Reis and L. C. Cucé, *Photodermatol. Photoimmunol. Photomed.*, 2009, **25**, 175–180.
- 39 B. L. Diffey, *Int. J. Cosmet. Sci.*, 1994, **16**, 47–52.
- 40 S. Q. Wang and H. W. Lim, Eds., *Principles and Practice of Photoprotection*, Springer Link.
- 41 E. L. Holt and V. G. Stavros, *Int. Rev. Phys. Chem.*, 2019, **38**, 243–285.
- 42 B. Diffey, *J. Photochem. Photobiol. B Biol.*, 2001, **64**, 105–108.
- 43 N. D. N. Rodrigues, M. Staniforth and V. G. Stavros, *Proc. R. Soc. A*, 2016, **472**, 20160677.
- 44 N. D. N. Rodrigues and V. G. Stavros, *Sci. Prog.*, 2018, **101**, 8–31.
- 45 J. F. Nash and P. R. Tanner, *Photodermatol. Photoimmunol. Photomed.*, 2014, **30**, 88–95.
- 46 B. Pruijm, L. Wright and A. Green, *Australas. J. Dermatol.*, 1999, **40**, 79–82.
- 47 B. L. Diffey, *J. Am. Acad. Dermatol.*, 2001, **45**, 882–885.
- 48 M. D. Horbury, E. L. Holt, L. M. M. Mouterde, P. Balaguer, J. Cebrián, L. Blasco, F. Allais and V. G. Stavros, *Nat. Commun.*, 2019, **10**, 1–8.
- 49 U. Osterwalder and B. Herzog, *Photochem. Photobiol. Sci.*, 2010, **9**, 470–481.
- 50 M. Avenel-Audran, L. Martin, H. Dutartre, C. Bernier, M. Jeanmougin, C. Comte, J. L. Peyron, L. Benkalfate, M. Michel, M. C. Ferrier-Lebouëdec, M. Vigan, J. L. Bourrain, A. Goossens and O. Outtas, *Arch. Dermatol.*, 2010, **146**, 753–757.
- 51 P. Collins and J. Ferguson, *Br. J. Dermatol.*, 1994, **131**, 124–129.
- 52 C. Szczurko, A. Domp martin, M. Michel, A. Moreau and D. Leroy, *Photodermatol. Photoimmunol. Photomed.*, 1994, **10**, 144–147.

- 53 M. E. Burnett and S. Q. Wang, *Photodermatol. Photoimmunol. Photomed.*, 2011, **27**, 58–67.
- 54 M. Krause, A. Klit, M. Blomberg Jensen, T. Søeborg, H. Frederiksen, M. Schlumpf, W. Lichtensteiger, N. E. Skakkebaek and K. T. Drzewiecki, *Int. J. Androl.*, 2012, **35**, 424–436.
- 55 M. Coronado, H. De Haro, X. Deng, M. A. Rempel, R. Lavado and D. Schlenk, *Aquat. Toxicol.*, 2008, **90**, 182–187.
- 56 C. A. Downs, E. Kramarsky-Winter, R. Segal, J. Fauth, S. Knutson, O. Bronstein, F. R. Ciner, R. Jeger, Y. Lichtenfeld, C. M. Woodley, P. Pennington, K. Cadenas, A. Kushmaro and Y. Loya, *Arch. Environ. Contam. Toxicol.*, 2016, **70**, 265–288.
- 57 K. L. Kinnberg, G. I. Petersen, M. Albrektsen, M. Minghlani, S. M. Awad, B. F. Holbech, J. W. Green, P. Bjerregaard and H. Holbech, *Environ. Toxicol. Chem.*, 2015, **34**, 2833–2840.
- 58 R. Danovaro, L. Bongiorno, C. Corinaldesi, D. Giovannelli, R. Danovaro, L. Bongiorno, C. Corinaldesi, D. Giovannelli, E. Damiani, P. Astolfi, L. Greci and A. Pusceddu, *Environ. Health Perspect.*, 2016, **116**, 441–447.
- 59 E. Schrödinger, *Ann. Phys.*, 1926, **384**, 361–376.
- 60 W. W. Parson, *Modern Optical Spectroscopy*, 2015.
- 61 P. Atkins and J. De Paula, *Atkins Physical Chemistry*, Oxford University Press, 10th edn., 2014.
- 62 M. Born and R. J. Oppenheimer, *Ann. Phys.*, 1927, **389**, 457–484.
- 63 P. Atkins and R. Friedman, *Molecular Quantum Mechanics*, Oxford University Press, 4th edn., 2005.
- 64 K. A. Peterson, *J. Chem. Phys.*, 1999, **111**, 7446–7458.
- 65 R. C. Hilborn, *Am. J. Phys.*, 1982, **50**, 982–986.
- 66 E. Condon, *Phys. Rev.*, 1926, **28**, 1182–1201.
- 67 E. Condon, *Phys. Rev.*, 1928, **32**, 858–872.

- 68 G. A. Worth and L. S. Cederbaum, *Annu. Rev. Phys. Chem.*, 2004, **55**, 127–158.
- 69 W. Domcke and G. Stock, *Theory of Ultrafast Nonadiabatic Excited-State Processes and their Spectroscopic Detection in Real Time*, 2007, vol. 100.
- 70 A. Devaquet, *Pure Appl. Chem.*, 1975, **41**, 455–473.
- 71 M. H. Farag, T. L. C. Jansen and J. Knoester, *J. Phys. Chem. Lett.*, 2016, **7**, 3328–3334.
- 72 P. Klán and J. Wirz, *Photochemistry of Organic Compounds: From Concepts to Practice*, Wiley, 1st edn., 2009.
- 73 A. Jablonski, *Nature*, 1933, **131**, 839–840.
- 74 K. Michael, *Discuss. Faraday Soc.*, 1950, 14.
- 75 J. R. Albani, *Structure and Dynamics of Macromolecules: Absorption and Fluorescence Studies*, 2011.
- 76 G. G. Stokes, *Philos. Trans. R. Soc. London*, 1852, **142**, 463–562.
- 77 G. S. Bedard, G. R. Fleming, O. L. J. Gijzeman and G. Porter, *Chem. Phys. Lett.*, 1973, **18**, 481–487.
- 78 R. Englman and J. Jortner, *Mol. Phys.*, 1970, **18**, 285–287.
- 79 M. A. El-Sayed, *J. Chem. Phys.*, 1963, **38**, 2834–2838.
- 80 M. Baba, *J. Phys. Chem. A*, 2011, **115**, 9514–9519.
- 81 E. Fermi, *Prog. Theor. Phys.*, 1950, **5**, 570–583.
- 82 J. Abmann, M. Kling and B. Abel, *Angew. Chemie - Int. Ed.*, 2003, **42**, 2226–2246.
- 83 J. C. Owrutsky, *Annu. Rev. Phys. Chem.*, 1994, **45**, 519–55.
- 84 T. A. A. Oliver, Y. Zhang, A. Roy, M. N. R. Ashfold and S. E. Bradforth, *J. Phys. Chem. Lett.*, 2015, **6**, 4159–4164.
- 85 B. L. Diffey, P. R. Tanner, P. J. Matts and J. F. Nash, *J. Am. Acad. Dermatol.*, 2000, **43**, 1024–1035.

- 86 N. D. N. Rodrigues, M. Staniforth, J. D. Young, Y. Peperstraete, N. C. Cole-Filipiak, J. R. Gord, P. S. Walsh, D. M. Hewett, T. S. Zwier and V. G. Stavros, *Faraday Discuss.*, 2016, **194**, 709–729.
- 87 Y. Peperstraete, M. Staniforth, L. A. Baker, N. D. N. Rodrigues, N. C. Cole-Filipiak, W.-D. Quan and V. G. Stavros, *Phys. Chem. Chem. Phys.*, 2016, **18**, 28140–28149.
- 88 L. A. Baker, M. D. Horbury, S. E. Greenough, P. M. Coulter, T. N. V Karsili, G. M. Roberts, A. J. Orr-Ewing, M. N. R. Ashfold and V. G. Stavros, *J. Phys. Chem. Lett.*, 2015, **6**, 1363–1368.
- 89 K. Y. Law and J. Shoham, *J. Phys. Chem.*, 1994, **98**, 3114–3120.
- 90 A. D. Dunkelberger, R. D. Kieda, B. M. Marsh and F. F. Crim, *J. Phys. Chem. A*, 2015, **119**, 6155–6161.
- 91 N. D. N. Rodrigues, N. C. Cole-Filipiak, M. D. Horbury, M. Staniforth, T. N. V. Karsili, Y. Peperstraete and V. G. Stavros, *J. Photochem. Photobiol. A Chem.*, 2018, **353**, 376–384.
- 92 A. Beeby and A. E. Jones, *Photochem. Photobiol.*, 2000, **72**, 10.
- 93 F. . Gsparro, *Photodermatol.*, 1985, **2**, 151–157.
- 94 S. K. Allen, A. Todd and J. M. Allen, *J. Photochem. Photobiol. B Biol.*, 1996, **32**, 33–37.
- 95 S. Afonso, K. Horita, J. P. Sousa E Silva, I. F. Almeida, M. H. Amaral, P. A. Lobão, P. C. Costa, M. S. Miranda, J. C. G. Esteves Da Silva and J. M. Sousa Lobo, *J. Photochem. Photobiol. B Biol.*, 2014, **140**, 36–40.
- 96 F. Garcia-Pichel and R. W. Castenholz, *Appl. Environ. Microbiol.*, 1993, **59**, 163–169.
- 97 W. M. Bandaranayake, *Nat. Prod. Rep.*, 1998, **15**, 159–172.
- 98 Q. Gao and F. Garcia-Pichel, *Nat Rev Microbiol*, 2011, **9**, 791–802.
- 99 S. Pattanaargson, T. Munhapol, P. Hirunsupachot and P. Luangthongaram, *J. Photochem. Photobiol. A Chem.*, 2004, **161**, 269–274.

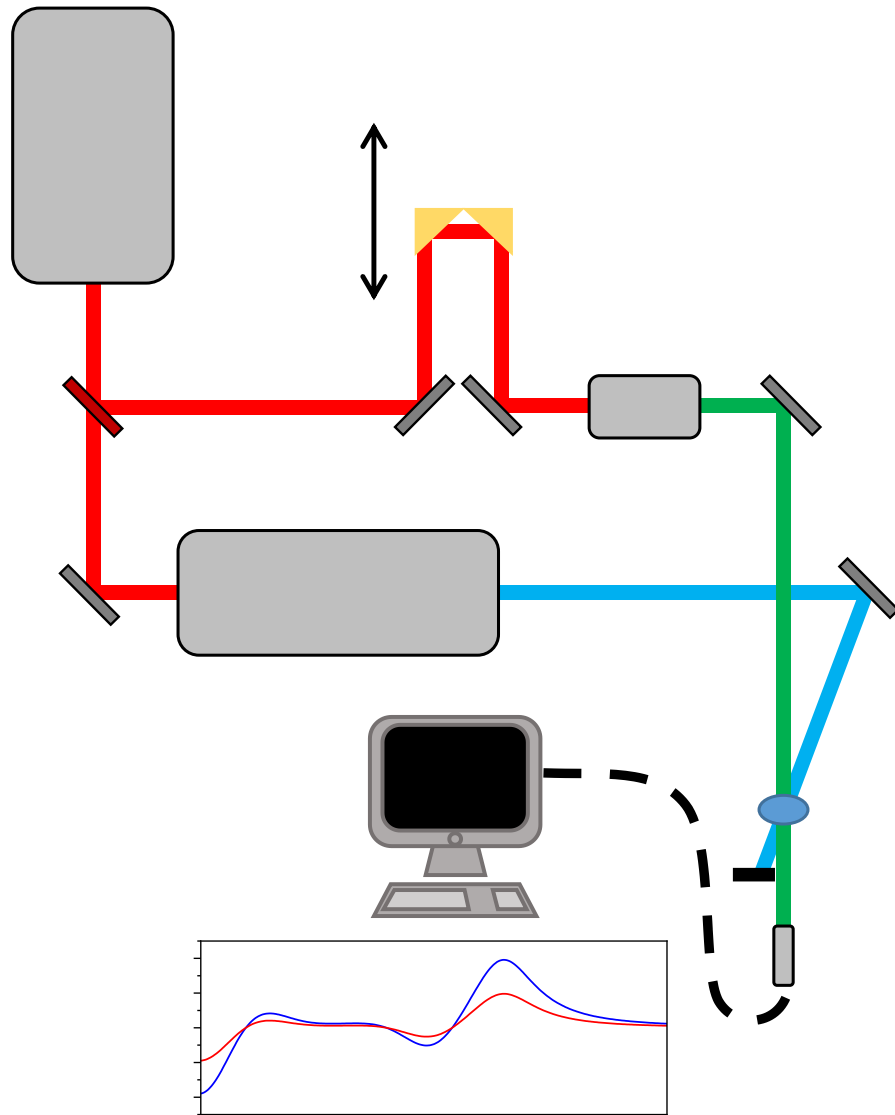
- 100 K. H. M. Cardozo, T. Guaratini, M. P. Barros, V. R. Falcao, A. P. Tonon, N. P. Lopes, S. Campos, M. A. Torres, A. O. Souza, P. Colepicolo and E. Pinto, *Comp. Biochem. Physiol. Part C Toxicol. Pharmacol.*, 2007, **146**, 60–78.
- 101 K. Whitehead and J. I. Hedges, *J. Photochem. Photobiol. B Biol.*, 2005, **80**, 115–121.
- 102 J. D. White, J. H. Cammack, K. Sakuma, G. W. Rewcastle and R. K. Widener, *J. Org. Chem.*, 1995, **60**, 3600–3611.
- 103 R. Losantos, I. Funes-Ardoiz, J. Aguilera, E. Herrera-Ceballos, C. García-Iriepa, P. J. Campos and D. Sampedro, *Angew. Chemie Int. Ed.*, 2017, **56**, 2632–2635.
- 104 J. D. White, J. H. Cammack and K. Sakuma, *J. Am. Chem. Soc.*, 1989, **111**, 8970–8972.
- 105 I. Karlsson, K. Vanden Broecke, J. Mårtensson, A. Goossens and A. Börje, *Contact Dermatitis*, 2011, **64**, 343–352.
- 106 F. R. Conde, M. S. Churio and C. M. Previtali, *Photochem. Photobiol. Sci.*, 2004, **3**, 960–967.
- 107 F. R. Conde, M. S. Churio and C. M. Previtali, *J. Photochem. Photobiol. B Biol.*, 2000, **56**, 139–144.
- 108 T. Gensch and C. Viappiani, *Photochem. Photobiol. Sci.*, 2003, **2**, 699–721.
- 109 L. G. Arnaut, R. A. Caldwell, J. E. Elbert and L. A. Melton, *Rev. Sci. Instrum.*, 1992, **63**, 5381–5389.
- 110 S. Abbruzzetti, C. Viappiani, D. H. Murgida, R. Erra-Balsells and G. M. Bilmes, *Chem. Phys. Lett.*, 1999, **304**, 167–172.
- 111 G. Porter and M. . Topp, *Proc. R. Soc. A Math. Phys. Eng. Sci.*, 1970, **315**, 163–184.
- 112 F. R. Conde, M. S. Churio and C. M. Previtali, *Photochem. Photobiol. Sci.*, 2007, **6**, 669–674.
- 113 M. Promkatkaew, S. Suramitr, T. Karpkird, S. Wanichwecharungruang, M. Ehara and S. Hannongbua, *Photochem. Photobiol. Sci.*, 2014, **13**, 583.

- 114 D. Shimada, R. Kusaka, Y. Inokuchi, M. Ehara and T. Ebata, *Phys. Chem. Chem. Phys.*, 2012, **14**, 8999–9005.
- 115 M. Promkatkaew, S. Suramitr, T. M. Karpkird, S. Namuangruk, M. Ehara and S. Hannongbua, *J. Chem. Phys.*, 2009, **131**, 224306.
- 116 K. M. Hanson, S. Narayanan, V. M. Nichols and C. J. Bardeen, *Photochem. Photobiol. Sci.*, 2015, **14**, 1607–1616.
- 117 P. Subramanian, D. Creed, A. C. Griffin, C. E. Hoyle and K. Venkataram, *J. Photochem. Photobiol. A Chem.*, 1991, **61**, 317–327.
- 118 C. Battie, S. Jitsukawa, F. Bernerd, S. Del Bino, C. Marionnet and M. Verschoore, *Exp. Dermatol.*, 2014, **23**, 7–12.
- 119 F. Poon, S. Kang and A. L. Chien, *Photodermatol. Photoimmunol. Photomed.*, 2015, **31**, 65–74.
- 120 J. Luo, Y. Liu, S. Yang, A. L. Flourat, F. Allais and K. Han, *J. Phys. Chem. Lett.*, 2017, **8**, 1025–1030.
- 121 A. Espagne, P. Changenet-Barret, P. Plaza and M. M. Martin, *J. Phys. Chem. A*, 2006, **110**, 3393–3404.
- 122 K. Heyne, O. F. Mohammed, A. Usman, J. Dreyer, E. T. J. Nibbering and M. A. Cusanovich, *J. Am. Chem. Soc.*, 2005, **127**, 18100–18106.
- 123 M. D. Horbury, L. A. Baker, N. D. N. Rodrigues, W.-D. Quan and V. G. Stavros, *Chem. Phys. Lett.*, 2017, **673**, 62–67.
- 124 J. F. W. Herschal, *Earth Environ. Sci. Trans. R. Soc. Edinburgh*, 1823, **9**, 445–460.
- 125 N. Bohr, *London, Edinburgh, Dublin Philos. Mag. J. Sci.*, 1913, **26**, 476–502.
- 126 R. G. W. Norrish and G. Porter, *Nature*, 1949, 164, 658.
- 127 G. Porter, *Am. Assoc. Adv. Sci.*, 1968, **160**, 1299–1307.
- 128 T. H. Maiman, *Phys. Rev. Lett.*, 1960, **4**, 564–566.
- 129 C. V. Shank and E. P. Ippen, *Appl. Phys. Lett.*, 1974, **24**, 373–375.

- 130 M. Dantus, R. M. Bowman and A. H. Zewail, *Nature*, 1990, **343**, 737–739.
- 131 N. F. Scherer, J. L. Knee, D. D. Smith and A. H. Zewail, *J. Phys. Chem.*, 1985, **89**, 5141–5143.
- 132 M. Dantus, M. J. Rosker and A. H. Zewail, *J. Chem. Phys.*, 1988, **89**, 6128–6140.
- 133 T. C. Weinacht and B. J. Pearson, *Time-Resolved Spectroscopy*, CRC Press, 2010.
- 134 M. Fushitani, *Annu. Reports Sect. 'C' (Physical Chem.)*, 2008, **104**, 272.
- 135 M. Staniforth and V. G. Stavros, *Proc. R. Soc. London A Math. Phys. Eng. Sci.*
- 136 M. Monti, J. M. Woolley, M. Staniforth, A. Wijesekara, S. X. Tao, R. M. I. Bandara, I. Jayawardena, A. Crocker, E. Griffin, S. R. P. Silva, R. A. Hatton and J. Lloyd-Hughes, in *Proc.SPIE*, 2019, vol. 10916.
- 137 R. Berera, R. van Grondelle and J. T. M. Kennis, *Photosynth. Res.*, 2009, **101**, 105–118.
- 138 L. A. Baker, M. D. Horbury and V. G. Stavros, *Opt. Express*, 2016, **24**, 10700.
- 139 L. A. Baker, M. D. Horbury, S. E. Greenough, F. Allais, P. S. Walsh, S. Habershon and V. G. Stavros, *J. Phys. Chem. Lett.*, 2016, **7**, 56–61.
- 140 S. M. Bachrach, *Computational Organic Chemistry*, 2006.
- 141 A. L. Parrill and K. B. Lipkowitz, Eds., *Reviews in Computational Chemistry Volume 30*, Wiley, 2006, vol. 15.
- 142 L. González, D. Escudero and L. Serrano-Andrés, *ChemPhysChem*, 2012, **13**, 28–51.
- 143 M. Cossi, V. Barone, B. Mennucci and J. Tomasi, *Chem. Phys. Lett.*, 1998, **286**, 253–260.
- 144 A. Klamt and G. Schüürmann, *J. Chem. Soc. Perkin Trans. 2*, 1993, **0**, 799–805.

- 145 M. A. P. Turner, M. D. Horbury, V. G. Stavros and N. D. M. Hine, *J. Phys. Chem. A*, 2019, **123**, 873–880.
- 146 T. J. Zuehlsdorff, P. D. Haynes, M. C. Payne and N. D. M. Hine, *J. Chem. Phys.*, 2017, **146**, 146–159.
- 147 F. Santoro, V. Barone, T. Gustavsson and R. Improta, *J. Am. Chem. Soc.*, 2006, **128**, 16312–16322.
- 148 A. Köhl and W. Domcke, *Chem. Phys.*, 2000, **259**, 227–236.
- 149 B. Roos and P. R. Taylor, *Chem. Phys.*, 1980, **48**, 157–173.
- 150 B. O. Roos, *Int. J. Quantum Chem.*, 1980, **18**, 175–189.
- 151 P. Honenberg and W. Kohn, *Phys. Rev.*, 1964, **136**, B864.
- 152 W. Kohn and L. J. Sham, *Phys. Rev.*, 1965, **140**, 1133.
- 153 R. E. Stratmann, G. E. Scuseria and M. J. Frisch, *J. Chem. Phys.*, 2002, **109**, 8218–8224.

2 Experimental



“If we knew what it was we were doing, it would not be called research, would it?”

Albert Einstein

2.1 Femtosecond Pulse Generation

2.1.1 Laser Operation

In order to generate femtosecond ($1 \text{ fs} = 10^{-15} \text{ s}$) laser pulses, one must first understand the basic principles of lasers (Light Amplification by Stimulated Emission of Radiation). The first laser was built by Theodore Maiman in 1960,^{1,2} with the underpinning theory of stimulated and spontaneous emission put forward by Albert Einstein in 1917.³ Lasers rely on the principles of absorption and emission (discussed in Chapter 1), particularly that of stimulated emission where the interaction of an incoming photon with the correct energy allows a transition to a lower lying energy level through the emission of a photon of the same energy and direction.⁴ The use of stimulated emission allows for the generation of a coherent monochromatic laser beam.^{3,5,6}

2.1.1.1 Population Inversion

For two levels of a molecule which have energies of E_1 and E_2 where $E_2 > E_1$, the population distribution is given by the Boltzmann distribution, Equation 2.1.

$$\frac{N_2}{N_1} = \frac{g_2}{g_1} e^{-\frac{(E_2-E_1)}{k_b T}} \quad (2.1)$$

Where N_2/N_1 is the ratio of the population in levels 1 and 2 with degeneracies g_2/g_1 , k_b is the Boltzmann constant and T is the temperature in Kelvin. For an electronic transition at room temperature in thermal equilibrium, $E_2 - E_1$ can be considered much larger than $k_b T$, thus the population of N_1 is much greater than that of N_2 . As the temperature increases, the populations equalise. The rate of population change, k , between the two levels for absorption, stimulated emission and spontaneous emission are given by the Einstein relations given, respectively by:⁷

$$k_{1 \rightarrow 2} = N_1 \rho_\nu B_{12}, \quad (2.2)$$

$$k_{2 \rightarrow 1} = N_2 \rho_\nu B_{21}, \quad (2.3)$$

$$k_{2 \rightarrow 1} = N_2 A_{21}. \quad (2.4)$$

Here ρ_ν is the density of photons interacting with the system, and B_{12} , B_{21} , A_{21} are constants termed the Einstein coefficients.⁷ When in an equilibrium state, the rate of

absorption will equal the sum of the rates of spontaneous and stimulated emission, given by,

$$N_1\rho_\nu B_{12} = N_2\rho_\nu B_{21} + N_2A_{21}. \quad (2.5)$$

For lasing to occur, the rate of stimulated emission must increase compared to the rates of spontaneous emission and absorption. Through Equation 2.5, it can be seen that an increase in N_2 , which will consequently lead to a decrease in N_1 , along with an increase in the photon density, ρ_ν will increase this rate.⁷

As discussed above, normal conditions do not allow for a population inversion, defined as when the population of the higher energy state is greater than that of the lower state (ie. $N_2 > N_1$). Such a condition is commonly achieved through pumping the system; giving energy to the system to promote absorption of electrons to a higher energy level. For a two level system such as the one described *supra*, one is only able to achieve equal populations in both states.⁷ As such, three and four level systems are employed to achieve population inversion, as shown in Figure 2.1. These additional levels allow for population inversion to be maintained between two levels. For example, in a four level system (Figure 2.1) pumping populates the E_4 state which then decays quickly to the E_3 state, the upper lasing level. Effectively all of the population of E_4 is transferred to E_3 with a lifetime of τ_{43} . From here, the lasing transition with lifetime τ_{32} can occur between states 3 and 2. To maintain a sufficient population of state E_3 , the lasing transition proceeds with a lifetime longer than τ_{43} . When population arrives in E_2 it is then transferred out of the level back to E_1 with a lifetime τ_{21} . To maintain a sufficient level of population inversion between states E_3 and E_2 , the lifetime of E_3 must be greater than that of E_2 ($\tau_{32} \gg \tau_{21}$).⁷

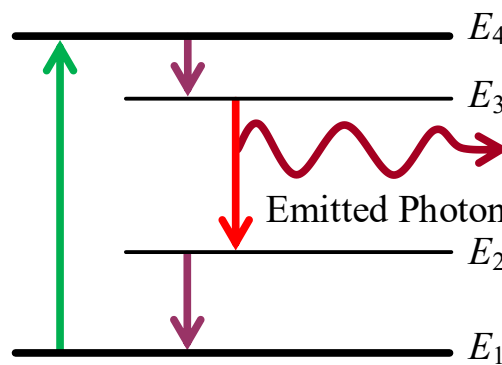


Figure 2.1 Schematic of a four level laser level system. Green arrows indicate pumping transitions, purple arrows represent nonradiative transitions and the red arrows depict the lasing transition.

For light propagating through a homogeneous material, the Einstein coefficients can be related to the intensity upon exit $I(x)$ for an initial intensity, I_0 , as given by⁷

$$I(x) = I_0 e^{-\alpha x} \quad (2.6)$$

Here α is an absorption coefficient that can be related to the Einstein coefficient for absorption, B_{12} , by:⁷

$$\alpha = \left(\frac{g_2}{g_1} N_1 - N_2 \right) \frac{B_{12} h \nu_{12} n}{c}. \quad (2.7)$$

Where h and c are Planck's constant and the speed of light respectively, n is the refractive index of the medium and, ν_{12} , is the frequency of the transition between the two levels. For any medium, the terms, $(B_{12} h \nu_{12} n)/c$, and g_2/g_1 , are constant. If $N_2 > N_1$, as is the case for population inversion, then α will be negative. Applying this result to Equation 2.6, the intensity of light increases exponentially as it traverses the material.⁷

2.1.1.2 Optical Cavities

Up until this point, we have only considered amplification of the photon number within a medium following a single pass through the material. Multiple passes through the amplifying medium, or 'gain medium', provide higher intensities which are required for nonlinear processes discussed in Section 2.2. To facilitate this, the gain medium is placed in an optical cavity. For a simple Fabry-Perot cavity,⁷ such as the one shown in Figure 2.2 the total gain, G , in a complete round trip of the cavity can be given in the following manner:

$$G = R_1 R_2 e^{2(k-\gamma)L} \quad (2.8)$$

Here R_1 and R_2 are the reflectivity of the mirrors, k is the gain coefficient of the medium and γ the loss coefficient, for a cavity of length L . To ensure lasing, $G > 1$.⁷ This leads to the threshold coefficient for gain, k_{th} , to be:

$$k_{th} = \gamma + \frac{1}{2L} \ln\left(\frac{1}{R_1 R_2}\right) \quad (2.9)$$

For any cavity like the one shown in Figure 2.2, there are only certain frequency (or modes) which are supported by the cavity, termed cavity modes. As light bounces back

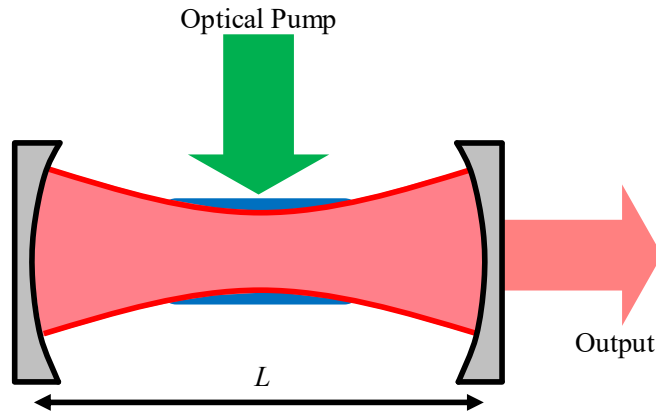


Figure 2.2 Pictorial representation of Fabry-Perot cavity of length L .

and forth between the mirrors interference occurs, generating standing waves which satisfy the condition for the frequency, ν :

$$\nu = \frac{pc}{2L} \quad (2.10)$$

where p is an integer. The separation of modes in the cavity is given by $\Delta\nu = c/2L$, and laser emission will only occur at these distinct frequencies separated by $\Delta\nu$. Of these supported frequencies, only those that fall within the envelope of the lasers lineshape function, $g(\nu)$ will propagate, depicted by Figure 2.3. This lineshape is influenced by inhomogeneous effects such as collisions between photons and phonons, and homogeneous effects such as crystal lattice imperfections in solid state lasers.⁷⁻¹⁰

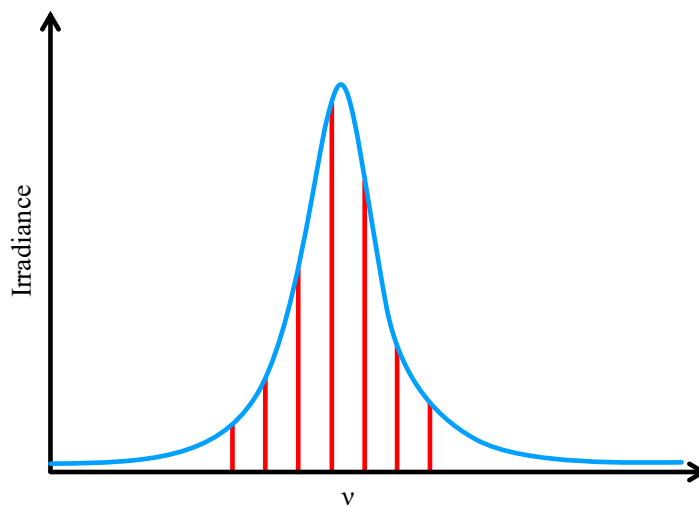


Figure 2.3 Laser cavity modes (red lines) which can oscillate within the envelope of the laser lineshape $g(\nu)$ (blue line).

2.1.2 Mode Locking

Lasers, such as those described above will output radiation as a continuous wave source. To allow access to dynamical information on the ultrafast timescales, this continuous wave must be converted to give pulses of light.¹¹ Mode locking is a technique by which ultrashort fs laser pulses can be generated through the superposition of multiple modes within a laser cavity.^{7,12} As discussed above, laser cavities can only support modes at discrete frequencies within the envelope of the laser lineshape.⁷ When multiple modes propagate, the intensity output from the cavity is no longer constant as a function of time. This variability is due to a dependence on the

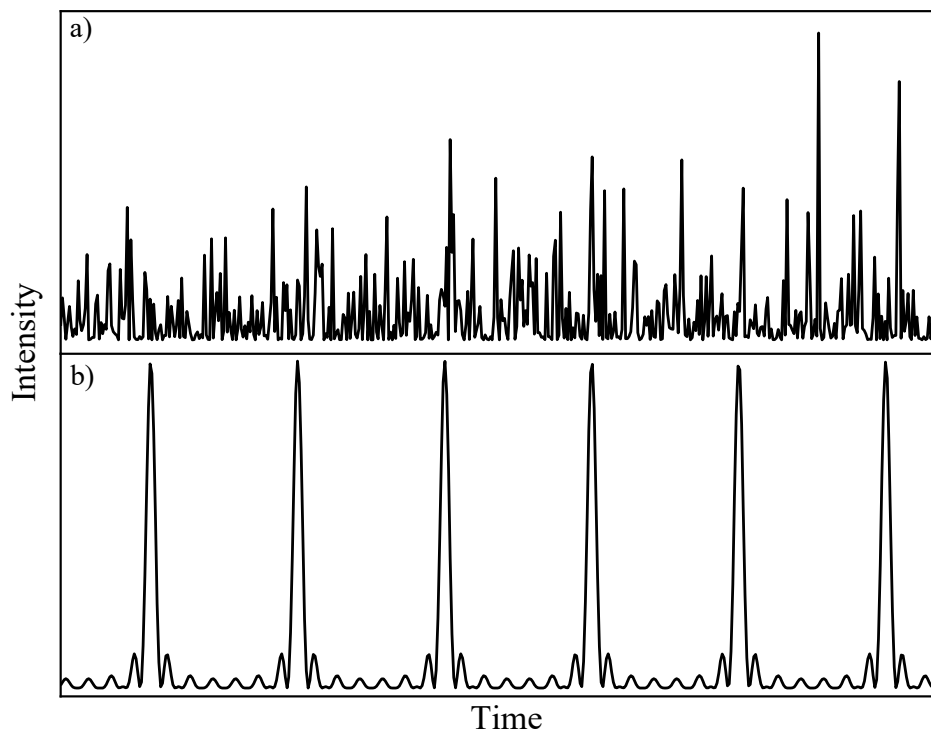


Figure 2.4 Plots of the intensity versus time for the first 6 modes with a) random phase, b) fixed phase relationship.

phase mismatch between differing modes leading to constructive and destructive interference.⁷ For a random phase relationship between the modes, the output intensity shows a random oscillation as a function of time, as given in Figure 2.4a. Where there is a fixed phase relationship, the time dependence gives periodic repetition, shown by Figure 2.4b.

For N number of modes oscillating within a cavity, the output of the electric field can be described by:

$$E(t) = \sum_{n=0}^{N-1} A_n e^{-i(\omega_n t + \varphi_n)}. \quad (2.11)$$

Where A_n , ω_n and φ_n is the amplitude, angular frequency and the phase of the n^{th} mode respectively. For a fixed phase relationship, φ , and assuming that the amplitude of each mode is equal (A_0), Equation 2.11 can be written as:

$$E(t) = A_0 e^{i\varphi} \sum_{n=0}^{N-1} e^{-i\omega_n t} \quad (2.12)$$

For Ti:sapphire laser systems, which provided the laser pulses for the transient electronic absorption experimental setup for the entirety of this thesis work, mode locking is maintained through the Kerr lens effect.¹³⁻¹⁵ For an intense electric field the refractive index, n , of a material becomes dependent on the intensity of light applied, such that

$$n = n_0 + n_2 I. \quad (2.13)$$

Here, n_0 is the initial refractive index, n_2 is the second order refractive index and I , is the intensity of the electric field.¹³⁻¹⁵ Through this phenomenon and the nature of a Gaussian beam intensity distribution, the beam observes a non-uniform refractive index across its radius as it traverses the medium, causing the beam to focus.¹⁶ The intense mode-locked field is focussed further while the weaker intensity of the continuous wave remains unperturbed. Designing the cavity in such a way to support the high intensity fields of the mode locked laser pulse over the continuous wave field allows for the spatial separation of the beams.¹⁵ Further to the self-focussing induced by the Kerr effect, the pulse will also be affected by a phase shift as it passes through the medium. This phase change broadens the frequency spectrum of the laser pulse through self-phase modulation (SPM) while keeping the time domain constant.^{15,17} Production of laser pulses in the manner described provides a robust and well characterised method of generation and is used in many commercial systems.

2.1.3 Chirped Pulse Regenerative Amplification

While the techniques discussed above can generate pulses of light with energies up to nanojoules,¹⁸ higher energy laser pulses are often needed for nonlinear optical processes such as frequency conversion (Section 2.2). As such, methods of amplification are often used to produce laser pulses with energies of millijoules and above.^{19,20} One such method is that of Chirped Pulse Regenerative Amplification (CPA).^{15,21,22} In CPA, one laser pulse of the initially generated pulse train is temporally stretched by a factor of 10000 times using a pair of diffraction gratings to avoid

nonlinear effects and damage to the optical elements. The pulse is allowed into the regenerative amplifier through a Pockels cell,[†] Figure 2.5a. This pulse is then passed through the amplifier multiple times to generate the maximum peak power before being released through a second Pockels cell.^{15,21–23} Finally, the laser pulse is recompressed using a second pair of diffraction gratings to retrieve the same temporal pulse width as before the amplification. This process is shown pictorially in Figure 2.5; using this technique it is possible to generate fs laser pulses ranging in energy from 3-15 mJ.^{15,21–23}

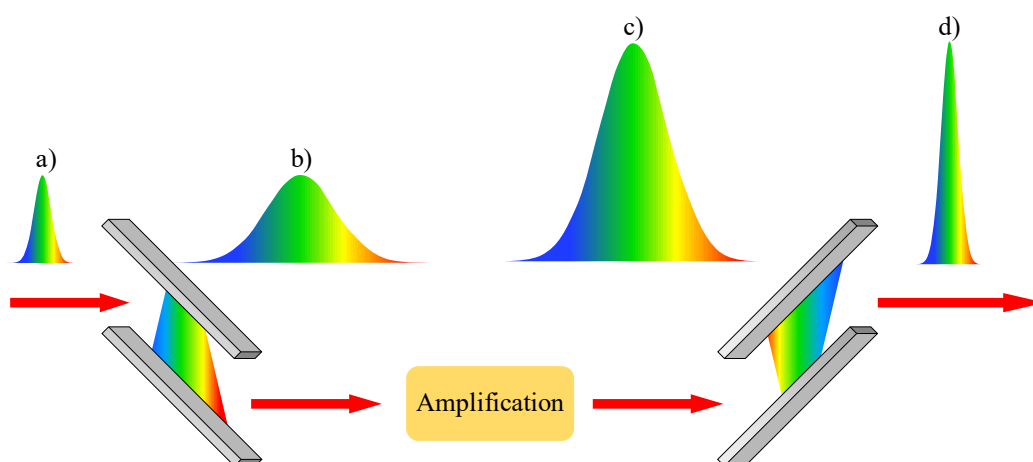


Figure 2.5 Pictorial representation of Chirped Pulse Amplification. a) Pulse enters the regenerative amplifier and is temporally stretched. b) Input pulse now stretched before amplification and enters the regenerative amplifier through the Pockels cell (not shown). c) The amplified stretched pulse exits the regenerative amplifier through the Pockels cell (not shown). d) Pulse is now amplified and recompressed leaving the laser system.

2.2 Nonlinear Optical Processes

The use of Ti:sapphire lasers allow for the generation of ultrashort laser pulses and high powers. However, the emission is centred on 800 nm, far away from the UV region required to photoexcite biomolecules utilised in photoprotection, as discussed in Chapter 1. As such, conversion from the near infrared (800 nm) to visible and UV regions of the electromagnetic spectrum is necessary for both the pump and probe pulses.

When light illuminates a medium, a secondary electric field, referred to as the polarisation density, P , is induced through the material. This polarisation density is linearly proportional to the applied electric field, E , given by:

[†] Pockels cell are electro-optic devices which, when an electric field is applied, changes the polarisation angle of the crystal allowing for laser pulses to be let in and out of the amplification stage based on the polarisation of the light.^{7,15}

$$P = \varepsilon_0 \chi E(t). \quad (2.14)$$

Where ε_0 is the dielectric constant and χ the linear susceptibility of the given material.^{16,24} For light of a sufficient electric field strength, the susceptibility of the material is no longer linear and can be expanded to include higher order terms (Equation 2.15); here $\chi^{(n)}$ describes the order of susceptibility with $\chi^{(1)}$ being the linear susceptibility shown in Equation 2.14.^{16,24}

$$\chi = \chi^{(1)} + \chi^{(2)}E(t) + \chi^{(3)}E^2(t) + \dots \quad (2.15)$$

This expansion of the nonlinear susceptibility can be combined with Equation 2.14 to give,

$$P = \varepsilon_0 [\chi^{(1)}E(t) + \chi^{(2)}E^2(t) + \chi^{(3)}E^3(t) + \dots] \quad (2.16)$$

From now on, we shall only discuss the second order of susceptibility, as this is the term utilised for the frequency conversion in this thesis.

2.2.1 Frequency Conversion

Using the second order susceptibility allows for the generation of different wavelengths through an optical medium which has an asymmetric crystal structure.¹⁶ The second order polarisation $P^{(2)}$ can be written as:¹⁶

$$P^{(2)} = \varepsilon_0 \chi^{(2)} E^2(t). \quad (2.17)$$

For two distinct electric fields of angular frequencies ω_1 and ω_2 , the total field can be described by:¹⁶

$$E(t) = E_1 \cos[\omega_1 t] + E_2 \cos[\omega_2 t]. \quad (2.18)$$

Combining Equations 2.18 and 2.17 yields the second order polarisation as a function of two input frequencies ω_1 and ω_2 , the key terms are displayed in Figure 2.6. Each term corresponds to a differing physical process for $P^{(2)}$.[‡] As shown in Figure 2.6 the two waves ω_1 and ω_2 can combine to give the second harmonic of either incident wave, shown in panel a) of Figure 2.6 for ω_1 explicitly, as well as either as the difference or sum of the frequencies (panels b and c in Figure 2.6 respectively). The

[‡] The complete expansion yields a term for the optical rectification given by $1/2 (E_1^2 + E_2^2)$.¹⁶

fourth nonlinear optical process to consider is optical parametric generation where a single input ω_1 generates two beams ω_2 and ω_3 .¹⁶ For all four cases, the phase of the input and output beams must be matched for the three waves such that the net phase between the beams is zero, i.e. $\Delta\varphi = \varphi_1 - \varphi_2 - \varphi_3 = 0$.¹⁶ Figure 2.6 shows the four processes along with energy level diagrams of the conversions; solid lines represent the ground states while dashed lines represent virtual states.¹⁶

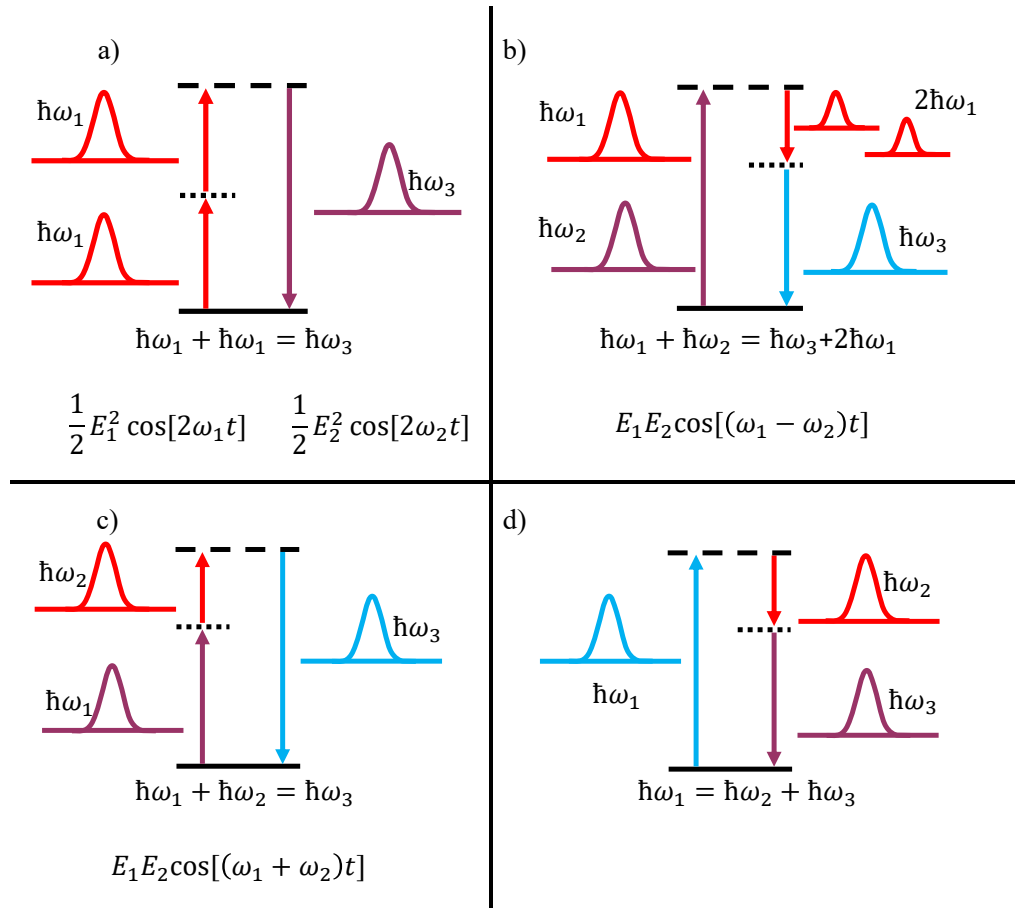


Figure 2.6 Nonlinear optical processes and their corresponding terms in the second order polarisation density, Equation 2.17. a) Second harmonic generation of either ω_1 (or ω_2). b) Difference frequency generation between ω_1 and ω_2 . c) Sum frequency generation between ω_1 and ω_2 . d) Optical parametric generation of ω_2 and ω_3 . Trigonometric terms below each process correspond to the expansion of Equation 2.17 with Equation 2.18.

2.2.2 Optical Parametric Amplification

Optical parametric amplification (OPA) allows for frequency conversion to generate a broad range of wavelengths. OPAs use optical parametric generation to produce two beams termed signal and the idler, ω_s , and, ω_i , respectively from the input beam termed the pump, ω_p . In a nonlinear optical crystal, the input pulse populates a virtual state from which stimulated emission occurs through interaction with a second input termed the seed pulse. This stimulated emission from the virtual state through the

interaction with the seed pulse consequently amplifies the seed pulse, and creates a second pulse termed idler such that its frequency ω_i is given by $\omega_i = \omega_p - \omega_s$. It is then the seed pulse which becomes the signal pulse on exit of the OPA.

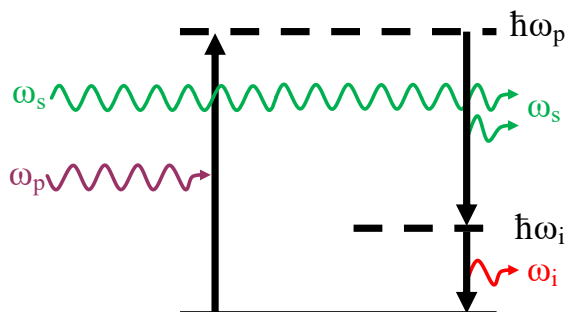


Figure 2.7 Energy level diagram for optical parametric amplification. Virtual states are shown by the dashed lines.

2.2.3 Super Continuum Generation

As shown above, the nonlinear susceptibility of materials can be used to generate a range of monochromatic beams. By exploiting the higher order susceptibilities within materials, a broadband super continuum (a laser pulse containing a wide range of wavelengths) can also be generated. This phenomenon requires the use of high intensity light conditions, which as discussed already is provided by fs laser pulses.^{25,26} The threshold power, P_{SCG} , required to generate such a super continuum can be given by:^{25,27}

$$P_{SCG} = \frac{\lambda^2}{2\pi n_0 n_2} \quad (2.19)$$

Here, λ is the central wavelength, and n_0 and n_2 are the linear and nonlinear refractive indices seen before in Equation 2.12. Both the Kerr lens effect and SPM are again utilised here to generate a stable continuum. As the beam focuses into the crystal the Kerr lensing increases, this feeds back further enhancing the intensity. The increase in intensity enables a higher order nonlinear optical process, generating the super continuum.

2.3 Transient Electronic Absorption Spectroscopy Setup

Thus far we have discussed the underlying principles required to produce fs laser pulses utilised in pump-probe experiments. We also described how nonlinear optics allows for the conversion of the near infrared wavelength output by the laser, to wavelengths more suited for the study of biological chromophores. What follows is an

in-depth description of the transient electronic absorption setup constructed and used to collect the data presented in Chapters 3, 4 and 5.

2.3.1 Laser Details

The laser system employed in the experiments is commercially available from Newport Spectra-Physics. Femtosecond laser pulses are generated by a Mai Tai SP oscillator producing 40 fs pulses in an 84 MHz pulse train, centred on 800 nm with a bandwidth of 60 nm. One in every 84,000 of these pulses are used to seed a Spitfire Ace-PA regenerative amplifier outputting at a 1 KHz repetition rate. This amplifier consists of two amplification stages: the first is a multiple pass configuration and this is followed by a single pass amplification stage. These two amplification stages allow for laser pulse energies of 13 mJ to be generated. Each amplification stage is pumped by an Ascend 60 Q-switched diode pumped solid state laser, outputting 35 W of average power in a 1 KHz pulse train centred on 527 nm.

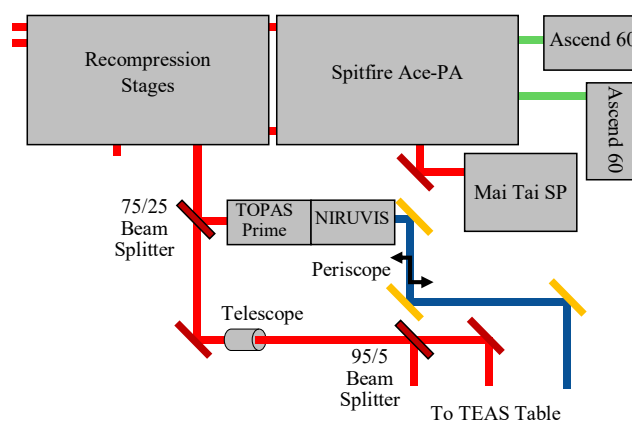


Figure 2.8 Schematic of commercially available laser system along with a portion of the beam path used for TEAS experiments. Red lines indicate 800 nm light, green lines correspond to 527 nm light and blue lines show the output of the TOPAS/NIRUVIS.

After the amplification stages, the beam is split into four equal beams, each directed to an independent external compressor allowing for separate recompressions for the multiple experiments available in the laboratory. One of these outputs (3.5 W average power, with 40 fs pulses centred at 800 nm operating at 1 KHz repetition rate, Figure 2.8) is used to generate the pump and probe pulses for the transient electronic absorption spectroscopy (TEAS) experiments. From here on the 800 nm beam will be termed the fundamental beam.

The fundamental beam is divided 75/25 *via* a beam splitter: the reflected 75% (≈ 2.5 W) is directed into an optical parametric amplifier (OPA, TOPAS PRIME

NIRUVIS) while the remaining 25% is reduced from an initial diameter of 12 mm to 8 mm through a reflective telescope to allow for easier control. This beam is then further split through the use of a 95/5 beam splitter to provide two beams of approximately 950 mW and 50 mW; these two beams are used to generate the harmonic pump and white light probe respectively. The overall layout described is shown schematically in Figure 2.8. Through optical parametric amplification the fundamental is converted into the required wavelength. Figure 2.9 shows the experimental design of the Transient Absorption table. Each of these three beams will now be discussed independently.

2.3.2 Pump Beam Generation

For photoexcitation, the pump beam is generated by two different methods. Firstly through the use of an OPA or secondly, harmonic generation from the fundamental beam; both of these will now be discussed.

2.3.2.1 Harmonic Generation

The displayed transient absorption setup has the capability to provide photoexcitation through both the second and third harmonic (400 and 267 nm, respectively) of the fundamental. This is achieved through either one or two beta-barium borate (β -BaB₂O₄, BBO, Figure 2.9) crystals. Two photons of 800 nm generate 400 nm (through second harmonic generation, Figure 2.6a) using one BBO and then a second BBO is used to generate the third harmonic of the fundamental (267 nm) through the combination of 800 nm and 400 nm photons (using sum frequency generation, Figure 2.6c)). Filtering of the required wavelength is achieved through the use of dielectric mirrors to remove residual 800 nm and generated 400 nm light if 267 nm is required.

2.3.2.2 TOPAS

Harmonic generation allows two distinct wavelengths to be generated (400 and 267 nm). Through the use of an OPA (TOPAS Prime, NIRUVIS, Figure 2.8) tunability of the photoexcitation wavelength across the ultraviolet region (UVR) and visible ranges is achieved. The OPA is pumped by 75% of the 3.5 W fundamental output of the laser, which then undergoes various nonlinear processes (discussed above in Section 2.2.1) to produce the signal and idler pulses (See Section 2.2.2). These pulses can then be converted further to give the required wavelengths through the methods described in Section 2.2.1. By applying the correct filtering the signal, idler and the required

wavelength generated through OPA can be separated. All of the crystal positions and filtering is computer controlled through the TOPAS software.

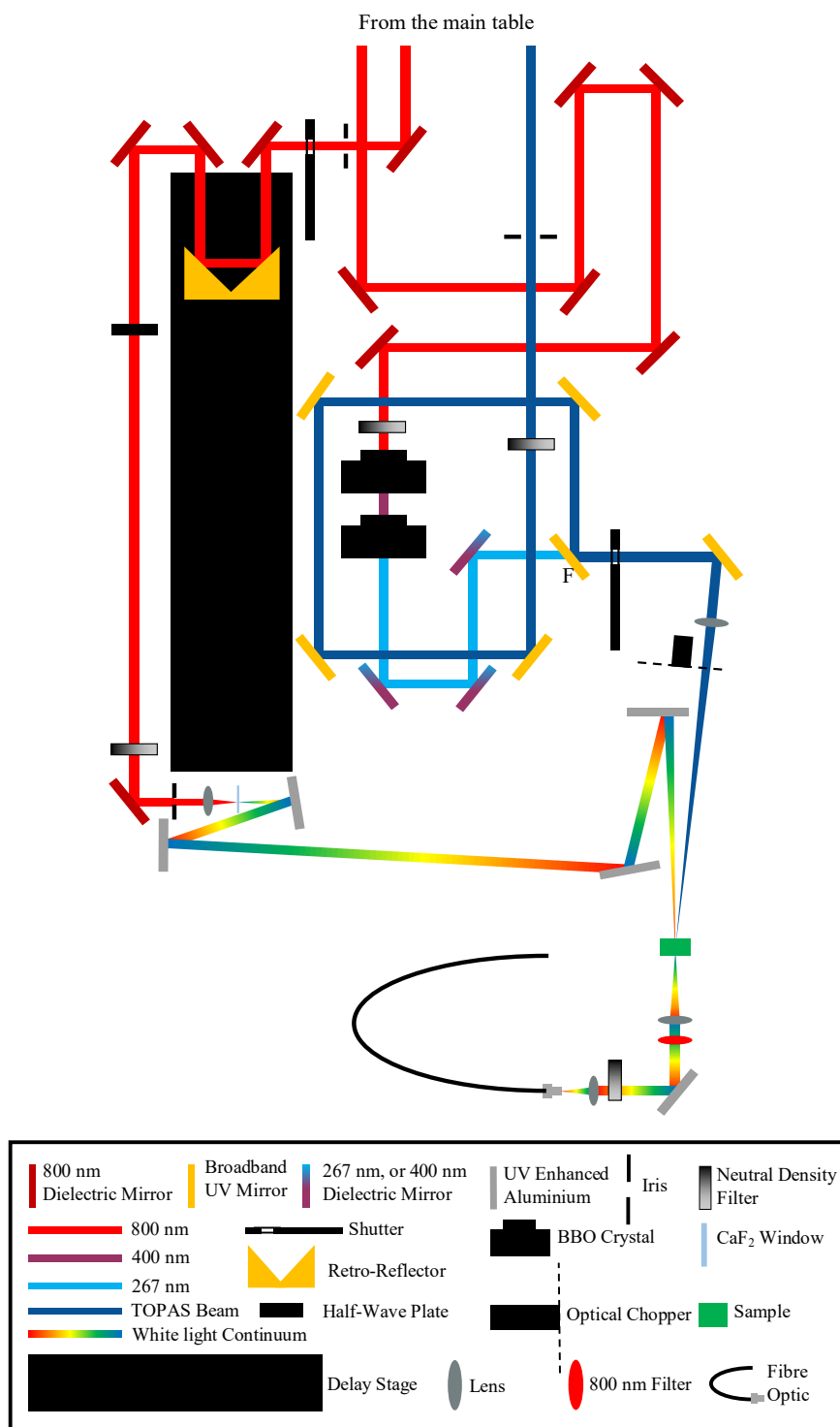


Figure 2.9 Schematic of transient electronic absorption setup. F donates that this mirror is located on a flip mount.

2.3.3 Probe Beam Generation

Probe pulses are generated using 50 mW of the fundamental, which is first reflected onto a translation stage (Newport M-IMS500CCHA) mounted with a hollow gold retro-reflector to allow pump-probe time delays up to 3 ns. The fundamental beam is then passed through a half wave plate to rotate the polarisation for measurements to be taken at magic angle (54.7°) with respect to the pump polarisation. This angle of polarisation between pump and probe pulses is used to minimise artefacts from molecular rotation.^{27,28} With the beam now in the correct polarisation, a super continuum can be generated by focussing the 800 nm fundamental beam into a calcium fluoride (CaF_2) window using a Z-cavity, shown in Figure 2.10.

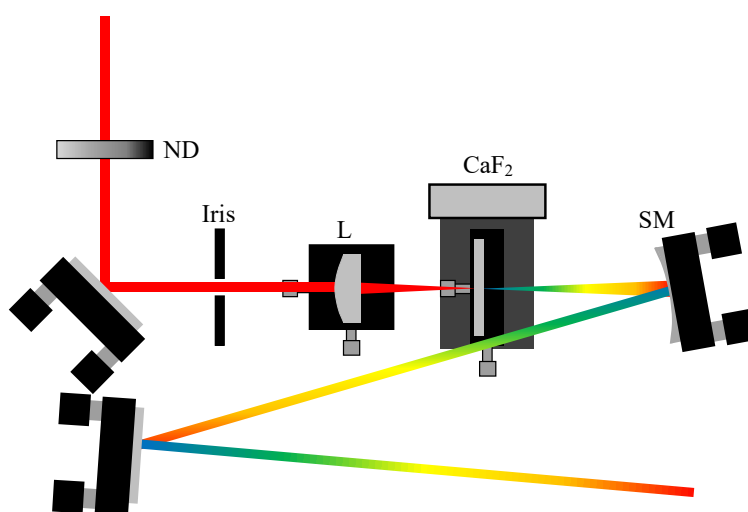


Figure 2.10 Schematic of the optical setup showing the Z cavity for white light generation.

In the Z-cavity the beam is attenuated using a variable neutral density (ND) filter and irised to select the central part of the beam, before being focussed by the 50 mm plano-convex lens (L) into the 1 mm thick CaF_2 window. Subsequent to this, the super continuum is collimated using a 50 mm concave spherical mirror (SM), before being passed to the sample interaction region. Due to the damage threshold of CaF_2 being below the power required for super continuum generation (Equation 2.19),²⁹ vertical translation of the crystal is required to ensure a stable spectrum and prevent damage to the crystal.^{30,31} This is achieved through mounting the CaF_2 window on a motorised Newport stage (MFA-PPD), allowing vertical translation of the crystal within the focal plane of the lens. The speed of the translation was optimised to maintain a stable continuum with a final value of 0.075 mms^{-1} . Other materials, such as sapphire, have damage thresholds above the power for continuum generation. However CaF_2 provides the deepest cut off for continuum generation allowing probe energies down

to 280 nm to be generated.²⁵ Stability and overall spectral profile of the generated spectrum was optimised through the size of the iris and the input power through the variable ND filter. Figure 2.11 shows the generated spectrum and image of the beam for differing input powers for a fixed iris size of approximately 3 mm.

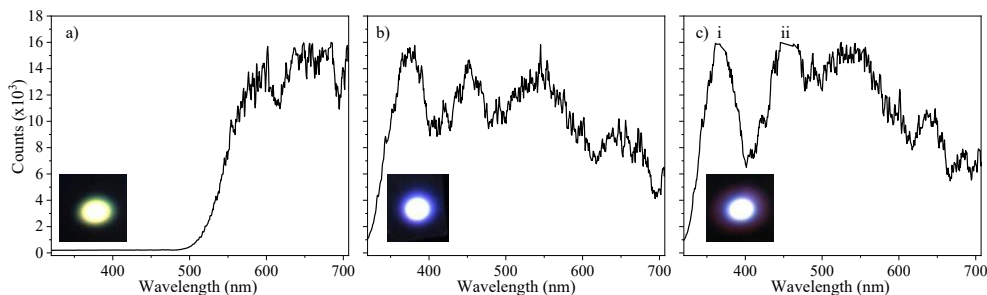


Figure 2.11 Spectral profiles of the generated super continuum for differing powers for an input beam diameter of 3 mm: a) under pumped, b) optimal c) over pumped. i and ii in panel c) denote where the spectrometer has reached saturation. Inserts show the beam profile in each spectrum.

As can be seen in Figure 2.11a, input powers just above the generation power (termed under pumping), of the crystal provides a shorter continuum bandwidth. Optimum pumping of the crystal such as that observed in Figure 2.11b) yields a stable continuum with a good beam quality. Increasing the power further (termed over pumping) into the crystal gives roughly the same spectral profile as the optimised power, however the beam profile is less homogenous. The spectra shown in Figure 2.11 are taken through the fibre coupled spectrometer, as such there is a dependence of the probe spectrum on the fibre used and the mirrors used in the beam path. All the mirrors used are ThorLabs UV enhanced Aluminium to reflect the broadest observable super continuum.

2.3.4 Sample Interaction

2.3.4.1 Pump-Probe Interaction

A schematic of the sample interaction geometry is shown in Figure 2.12. Pump pulses are focussed through a lens (L1) to a focal plane past the sample location (S) to give a pump beam diameter of approximately 500 μm at the sample region. A concave spherical mirror is used to limit the chromatic aberration of probe pulse. The 100 mm focal length, gives a beam diameter on average of 60 μm across the probe spectrum. Both the pump and probe beam diameter are measured through knife edge measurements at the sample region. The pump beam is larger than the probe beam at the sample to ensure that a uniform photoexcited area is interrogated with the probe pulse.

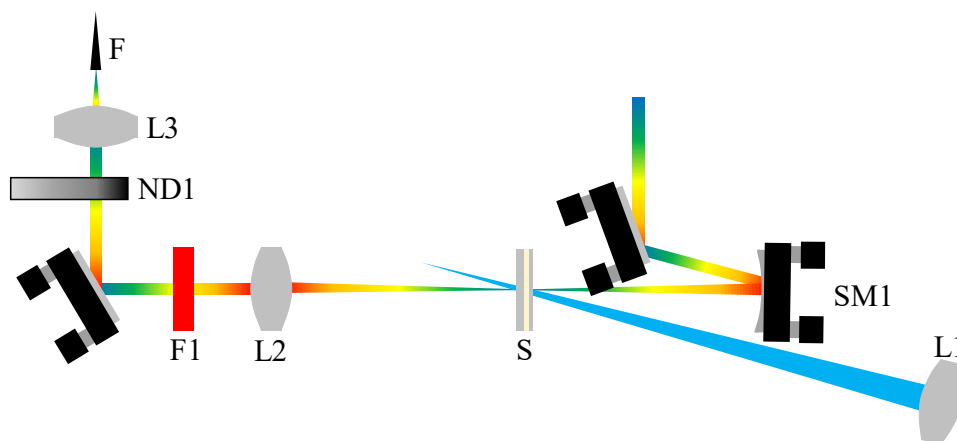


Figure 2.12 Schematic for sample interaction and probe collection. Shown is the pump focussing lens (L1), sample (S), probe focussing spherical mirror (SM1), probe collimation lens (L2), 0° 800 nm dielectric (F1), variable neutral density filter (ND1), focussing lens (L3), and launch into the fibre optic (F).

Post sample interaction probe pulses are collimated through a 100 mm focal length lens (L2) and then passed through a 0° 800 nm dielectric filter (F1) to prevent the residual 800 nm fundamental beam from reaching the spectrometer, which would saturate the spectrometer, leading to damage of the CCD array. Probe light is further attenuated, if necessary using a variable neutral density filter (ND1) before focussing into the tip of the fibre using a lens with 50 mm focal length (L3). The crossing angle between pump and probe beam is held at approximately 4° to minimise temporal effects from geometric alignment; a large crossing angle between pump and probe decreases the temporal resolution.²²

2.3.4.2 Group Velocity Dispersion

For a spectrally broadband pulse, such as that for the probe pulse, each wavelength will travel through any given medium at different speed due to the observed difference in the material's refractive index, given by the Sellmeier equation.³²

$$n^2(\lambda) = 1 + \sum \frac{B_i \lambda^2}{\lambda^2 - C_i} \quad (2.19)$$

Here n is the refractive index, λ the wavelength and B_i and C_i are termed Sellmeier coefficients which vary from material to material.³² This effect can provide advantages such as compression of pulses through prisms, allowing the slower moving shorter wavelengths, to approach the leading longer wavelengths.^{15,31} In the setup shown above (Figure 2.9) all probe wavelengths travel approximately the same distance. As such, the super continuum probe does not arrive at the sample interaction region

simultaneously for each wavelength, introducing a chirp to the experimental data. The chirp can be seen as a difference in time zero (time delay where the pump and probe arrive simultaneously at the sample, $t_0(\lambda)$), as a function of probe wavelength, Figure 2.13.

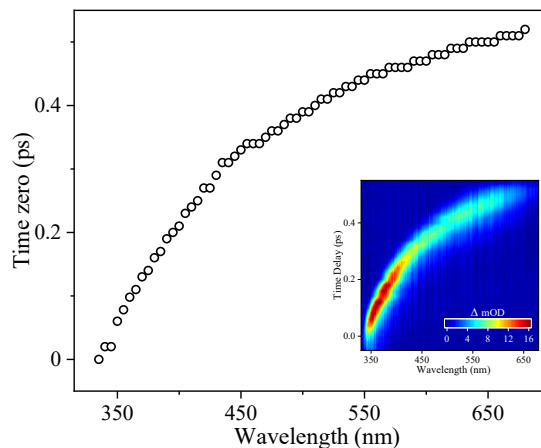


Figure 2.13 Plot of central wavelength for Gaussians fitted to the solvent response of neat dioxane photoexcited at 270 nm with a 100 μm path length. Insert shows the data used for the fitting in the form of a false colour heat map.

2.3.4.3 Instrument Response

As seen above in Figure 2.13 the pump-probe interaction in neat solvent gives rise to a multiphoton absorption around time zero which provides, to a first approximation the cross correlation between the pump and probe pulses.^{31,33,34} The cross correlation between the pump and probe is then fitted to a Gaussian function to extract the full width half maximum (FWHM) of the cross correlation. A plot of the FWHM of the cross correlation as a function of probe wavelength is shown in Figure 2.14. From the graph, it can be seen that an instrument response of 100 fs is achieved across the probe region for the sample thickness of 100 μm .

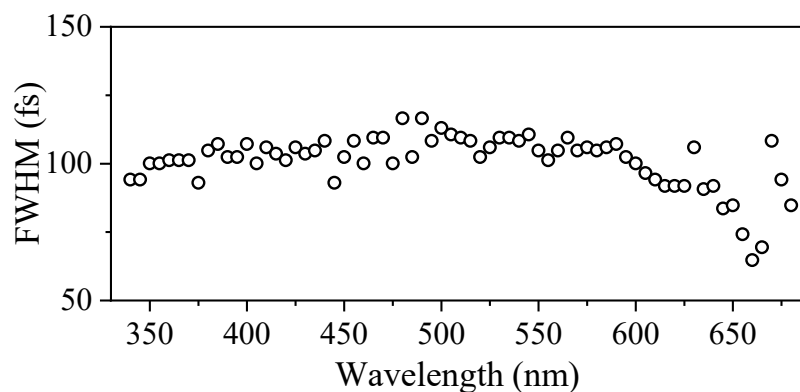


Figure 2.14 Plot of FWHM for the cross correlation between pump and probe as a function of probe wavelength. Data was obtained from photoexcitation of neat dioxane at 270 nm using a sample thickness of 100 μm .

2.3.4.4 Sample Delivery

Samples are prepared as solutions of 25 to 50 ml at suitable concentrations in the desired solvent and placed in a sample reservoir. The increased solution volume allows for dilution of any photoproducts formed. Samples are then circulated through a Harrick flow cell using a diaphragm pump (SIMDOS 02) at sufficient rate to ensure a fresh sample is interrogated with each pump-probe pulse pair. CaF₂ windows are used to seal the Harrick flow cell with a 1 mm thick window used before the sample and a 2 mm thick window used after the sample as the beams propagate through. Sample thicknesses can be varied through the use of PTFE spacers ranging in size from 12 to 950 μm ; a photo depicting the flow of liquid through the pump and Harrick cell is shown in Figure 2.15. For samples of small volumes or those that aggregate on the CaF₂ windows, the samples are translated in the focal plane of the white light continuum to ensure fresh sample is exposed to each pump-probe pulse pair. The translation is achieved by two perpendicularly mounted motorised stages (MFA-PPD, Figure 2.15). To ensure that sample degradation throughout the data acquisition had minimal effects on the measurements described in Chapters 3, 4 and 5, signal intensities were recorded both before and after the measurements and compared.

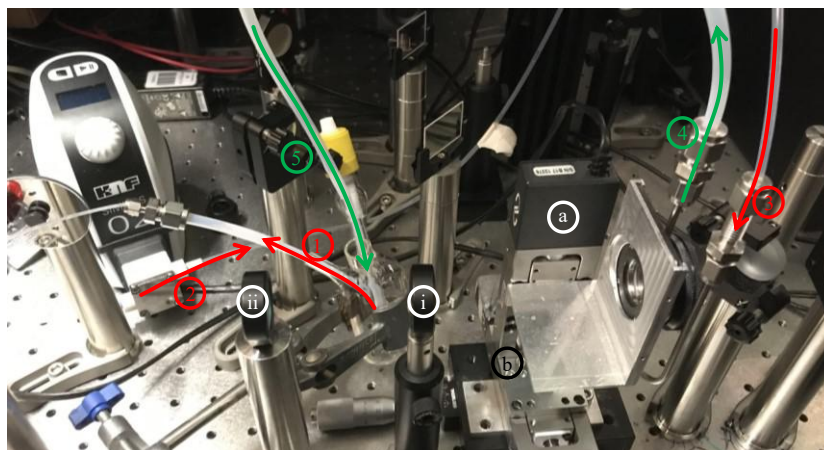


Figure 2.15 Pictorial representation of sample recirculation: 1. Sample is taken out of the reservoir, 2. Sample is passed through the diaphragm pump, 3. Sample is passed through the Harrick cell from the bottom to the top, to allow air pockets to escape, 4. Sample is then removed from the cell and passed back to the reservoir (5). a) Motorised stage for vertical sample translation b) Motorised stage for horizontal sample translation. Also visible is the collimating lens (i) and the 0° degree 800 nm dielectric (ii).

2.3.5 Data Collection and System Control

Probe spectra are acquired on a fibre coupled Avantes, Avaspec-ULS1650F spectrometer. The spectrometer triggers at 1 KHz, while the chopper (Figure 2.9) blocks every other pump pulse from reaching the sample. This method allows the

spectrometer to receive unpumped (pump blocked) and pumped (pump open) probe pulses back to back in corresponding pairs.

The system is controlled through a custom made LabVIEW virtual instrument (VI). The design of the VI is such that once the spectrometer has recorded the maximum acquisitions possible (2500), data is then read and removed from the spectrometer memory allowing for a different pump-probe time delay to be recorded. The VI then calculates the change in optical density (ΔOD) in the following manner:

$$\Delta OD = \log \left[\frac{I_0(\lambda)}{I_{pu}(\lambda, t)} \right] \quad (2.20)$$

In the above equation, $I_0(\lambda)$ is the wavelength dependent intensity of an probe pulse which has passed through a unpumped sample and $I_{pu}(\lambda, t)$, is the wavelength dependent intensity of the probe pulse passing through a pumped sample at a given time delay. As discussed above, pump-probe time delays are generated through an optical delay line. For data acquisition, pump-probe time delays are inputted as a text file into the VI which then converts this delay to stage position in millimetres. The VI randomly selects a time delay and the intensities of the probe pulses are acquired by the spectrometer. This randomisation reduces the effects of signals drifting over time, which may be caused by pump-probe misalignment or drifts in the laser power. Finally, a comparison system removes erroneous transient absorption spectra (TAS) through evaluation of the unpumped probe and a saved spectrum prior to the scan starting. If a spectrum is found to vary significantly compared to the reference, *i.e.* the counts differ from the reference spectrum by $\pm 5\%$, the time delay is repeated up to a maximum of 5 times before the scan continues.

2.4 Data Processing

Transient absorption measurements provide the ability to qualitatively assign molecular dynamics through visual inspection of spectral shifts along with comparison to literature and chemical intuition. For example, the presence of a ground state bleach (GSB) at maximum pump-probe time delays, allows the postulation that the recovery to the ground state is not 100%. A quantitative analysis can also be performed through applying a fitting procedure to the experimental data to assign lifetimes to the decays of the spectral features.

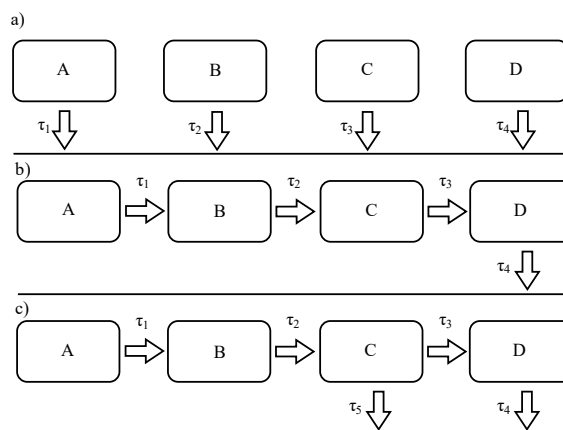


Figure 2.16 Models for: a) Parallel fitting procedure, where all components are populated immediately after photoexcitation. b) Sequential fitting procedure, where component A is the initially populated state following photoexcitation. c) Visual representation of branched dynamics from state C either decaying through state D or directly back to the ground state. Solid black lines represent the ground state.

The choice of the fitting model is crucial to understanding of the dynamical process observed. For transient absorption data, typically either single wavelength transients are taken and analysed or a global fitting model is used. For global fitting, two main types of models are used: (1) a parallel model or (2) a sequential model, depicted in Figure 2.16.³⁵ For a parallel model (Figure 2.16a), one assumes that the dynamical processes begin simultaneously from the initially populated state at photoexcitation. This model works well for systems in which there are multiple pathways originating at the same time. The sequential model, shown in Figure 2.16b, assumes that the processes follow along a chain, with the first being the decay from the initially photoexcited state through different states (labelled B, C and D in Figure 2.16), ultimately with the final decay (say) being back to the ground electronic state. A final model which could be used is a hybrid of both (1) and (2) and involves population decaying to a given state, which subsequently decays *via* branching of the population, *i.e.* the dynamics first follow a sequential model which then transitions to a parallel model branching from this populated state (Figure 2.16c). The sequential model is utilised for the fitting of all the data shown in Chapters 3-5. By choosing such a model we have made the assumption that the decay of the system occurs with no branching, parallel or reverse dynamics.³⁵ Further justification for the use of a sequential model is provided by the difference in the lifetimes with which distinct dynamical processes occur. As discussed in Chapter 1, the dynamical processes in solution occur at different lifetimes (intersystem crossing has a larger lifetime than internal conversion for example). An example of this is a situation where following photoexcitation the

excited electronic state undergoes a geometry rearrangement, which then subsequently undergoes internal conversion back to the ground electronic state. Both of these processes would occur with differing lifetimes in a sequential manner, rather than a parallel model where by the lifetime of internal conversion and the geometry arrangement are described as happening simultaneously.

2.4.1 Global Fitting Analysis

Global analysis of the data is performed in the TIMP package in the R programming language using the Glotaran interface.^{36,37} The experimental TAS, Φ can be described as a superposition of i components of the intensity of the signal $c_i(t)$ and its spectral component $\epsilon_i(\lambda)$,³⁵

$$\Phi = \sum_1^i c_i(t)\epsilon_i(\lambda). \quad (2.21)$$

For a multi-component model (where each component is a particular feature in the TAS), the signal intensity of each component $c_i(t)$ can be given as a vector, $c(t) = [c_1(t) \cdots c_i(t)]^T$. The change in the components as a function of time can then be described by the differential equation,

$$\frac{d}{dt} c(t) = Kc(t) + j(t). \quad (2.22)$$

Here K is an $i \times i$ matrix for which the off diagonal elements represent the decay between each spectral component ($A \rightarrow B \rightarrow C$), and the diagonal elements represent the overall decay for each component. For a parallel model, only the diagonal elements would be non-zero, while a sequential model has the off diagonal elements non-zero. $j(t)$ is a vector of i components corresponding to the population of each compartment such that $j(t) = IRF(t)[j_1(t) \cdots j_i(t)]$, where $IRF(t)$ is the instrument response function.³⁵ The $\epsilon_i(\lambda)$ term in Equation 2.21 models the spectral component of the data, where each spectrum decays with the associated lifetime given by the $c_i(t)$ function. The spectral components are given by the sum of skewed Gaussian components, for each value of i .^{36,38}

Initial parameters of the data are estimated through visual inspection of the data using the Glotaran interface.³⁷ These parameters include the number of decays i and their estimated lifetimes τ_i . Parameters for the instrument response and group velocity dispersion are also provided which TIMP models as a 3rd order polynomial.^{36,37} The

initial parameters allows for the generation a first fit of the data. This fit is then iterated through a partitioned variable projection algorithm.³⁶ Convergence of the fit to the experimental data is monitored using a finite difference approach for the gradient.³⁹ Errors in each lifetime are calculated through the linear approximation returning the standard errors of one standard deviation. Using this fitting procedure, the data can be described by the sum of exponentials contained in, $c_i^{EADS}(t)$, and evolutionary associated difference spectra, such that:

$$TAS_{fit}(t, \lambda) = \sum_{i=1}^l c_i^{EADS}(t)EADS_i(\lambda). \quad (2.23)$$

The EADS calculated here report on the spectral features. The changes between the spectral features can be used to assign dynamical processes. The overall quality of the fit is evaluated through the residuals (difference between fit and the data).

2.4.2 Chirp Correction

For a clearer visual display of the data in the form of false colour heat maps, the program Kinetics Observed After Light Absorption (KOALA), was used to correct for the chirp across the probe spectrum.⁴⁰ KOALA applies Equation 2.24 to the experimental data to correct for the group velocity dispersion across the probe spectrum.

$$t_0(\lambda) = ABP + GDD \left(\frac{2\pi c}{\lambda} \right) + \frac{1}{2} TOD \left(\frac{2\pi c}{\lambda} \right)^2 \quad (2.24)$$

The program first defines a unique time zero, $t_0(\lambda)$, at each probe wavelength for a threshold absorbance defined by the user. This $t_0(\lambda)$ is then plotted as a function of probe wavelength as shown in Figure 2.13; the threshold is set to be the maximum absorbance. This plot is then fit with Equation 2.24 to determine the absolute phase, group delay dispersion and third order dispersion given by ABP , GDD and TOD respectively. The absorbance values are then re-assigned to the time delays given by Equation 2.24. As only discrete time delays are able to be experimentally measured, linear interpolation is used to obtain the values for $t_0(\lambda)$. Figure 2.17 shows the effect of chirp correction on the instrument response of dioxane.

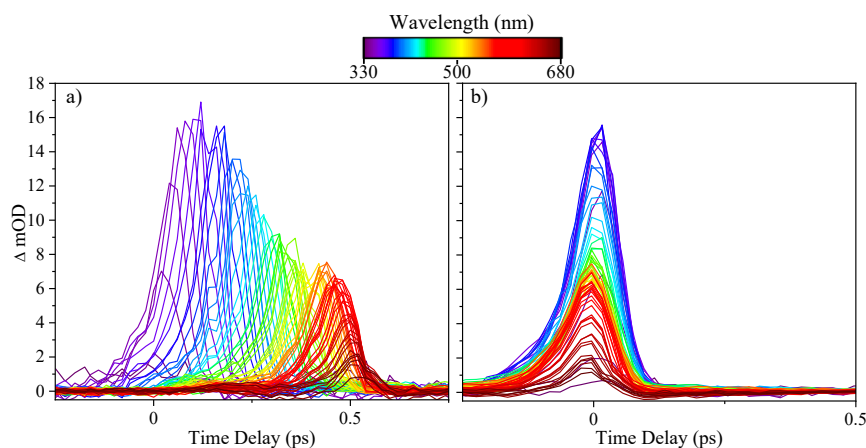


Figure 2.17 a) Plot of raw experimental transients showing how the peak signal as a function of probe wavelength changes, b) Plot of chirp corrected transients showing how each wavelength component now arrives simultaneously at $\Delta t = 0$.

2.5 Summary

In this Chapter, we have discussed the generation of fs pulses and how using nonlinear optical effects these fs pulses are transformed for use as the pump and probe pulses. We have then described the experimental setup and characterised the instrument response and dispersion of the instrumentation. Finally we considered the different fitting methods available to extract dynamical insights from 2-Dimensional spectroscopic data. These methods have been used throughout the following Chapters to describe the dynamics of multiple systems.

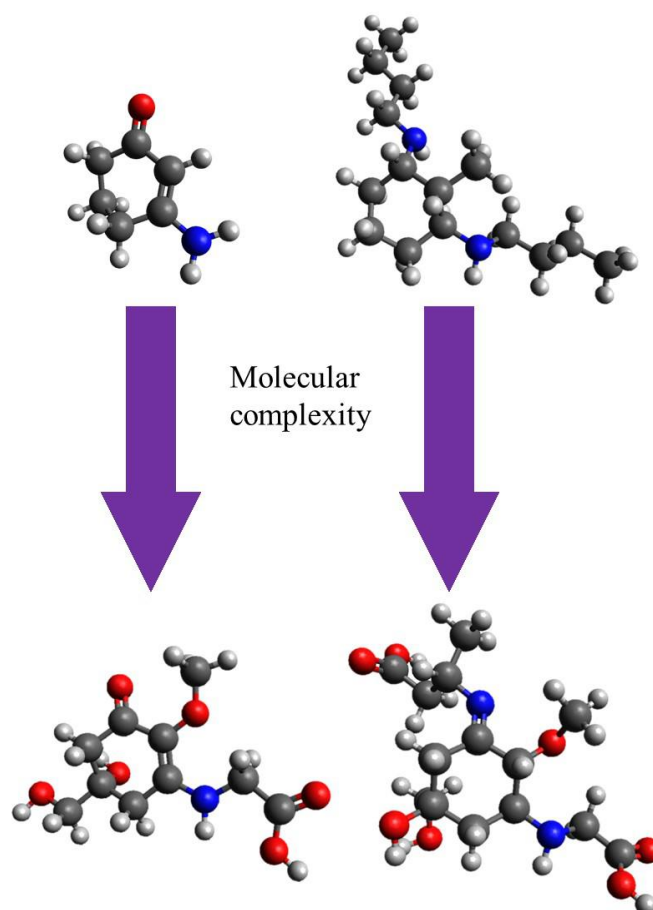
2.6 Bibliography

- 1 T. H. Maiman, *Phys. Rev. Lett.*, 1960, **4**, 564–566.
- 2 T. H. Maiman, *Nature*, 1960, **187**, 493–494.
- 3 A. Einstein, *Phys. Zeitschrift*, 1917, **18**, 167–183.
- 4 P. Atkins and J. De Paula, *Atkins Physical Chemistry*, Oxford University Press, 10th edn., 2014.
- 5 A. Einstein, *Verhandlungen der Dtsch. Phys. Gesellschaft*, 1916, **18**, 318–323.
- 6 R. C. Evans, P. Douglas and H. D. Burrows, *Applied Photochemistry*, 2014.
- 7 J. Wilson and J. Hawkes, *Optoelectronics: An Introduction*, Prentice Hall, 3rd edn., 1998.
- 8 N. Mermilliod, R. Romero, I. Chartier, C. Garapon and R. Moncorge, *IEEE J. Quantum Electron.*, 1992, **28**, 1179–1187.
- 9 W. W. Rigrod, *IEEE J. Quantum Electron.*, 1978, **14**, 377–381.
- 10 L. A. Pakhomycheva, E. A. Sviridenkov, A. F. Suchkov, K. V Titova and S. S. Churliov, *JETP Lett*, 1970, **12**, 43–45.
- 11 R. Berera, R. van Grondelle and J. T. M. Kennis, *Photosynth. Res.*, 2009, **101**, 105–118.
- 12 H. A. Haus, *IEEE J. Sel. Top. QUANTUM Electron.*, 2000, **6**, 1173–1185.
- 13 J. Kerr, *London, Edinburgh, Dublin Philos. Mag. J. Sci.*, 1875, **50**, 446–458.
- 14 J. Kerr, *London, Edinburgh, Dublin Philos. Mag. J. Sci.*, 1875, **50**, 337–348.
- 15 C. Rulliere, *Femtosecond Laser Pulses Principles and experiments*, Springer, New York, 2nd edn., 2004.
- 16 P. E. Powers and J. W. Haus, *Fundamentals of Nonlinear Optics*, Taylor Francis Group, 2nd edn., 2006.
- 17 G. P. Agrawal and N. A. Olsson, *IEEE J. Quantum Electron.*, 1989, **25**, 2297–2306.
- 18 W. Demtröder, Ed., *Laser Spectroscopy: Basic Concepts and Instrumentation*,

- Springer, Berlin, 3rd edn.
- 19 P. Maine, D. Strickland, P. Bado, M. Pessot and G. Mourou, *IEEE J. Quantum Electron.*, 1988, **24**, 398–403.
 - 20 F. Röser, T. Eidam, J. Rothhardt, O. Schmidt, D. N. Schimpf, J. Limpert and A. Tünnermann, *Opt. Lett.*, 2007, **32**, 3495.
 - 21 D. Strickland and G. Mourou, *Opt. Commun.*, 1985, **55**, 447–449.
 - 22 J.-C. Diels and W. Rudolph, *Ultrashort Laser Pulse Phenomena: Fundamentals, Techniques, and Applications on a Femtosecond Time Scale*, Elsevier Science & Technology, 2nd edn., 2006.
 - 23 E. Treacy, *IEEE J. Quantum Electron.*, 1969, **5**, 454–458.
 - 24 C. Li, *Nonlinear optics: Principles and applications*, Springer Link, 2016.
 - 25 M. Bradler, P. Baum and E. Riedle, *Appl. Phys. B Lasers Opt.*, 2009, **97**, 561–574.
 - 26 P. L. Baldeck, P. P. Ho and R. R. Alfano, *Rev. Phys. Appliquée*, 1987, **22**, 1677–1694.
 - 27 P. J. M. Johnson, V. I. Prokhorenko and R. J. D. Miller, *Opt. Express*, 2009, **17**, 21488.
 - 28 R. Lakowicz, Joseph, *Principles of Fluorescence Spectroscopy*, 3rd edn., 2006.
 - 29 S. Laimgruber, H. Schachenmayr, B. Schmidt, W. Zinth and P. Gilch, *Appl. Phys. B Lasers Opt.*, 2006, **85**, 557–564.
 - 30 I. Buchvarov, A. Trifonov and T. Fiebig, *Opt. Lett.*, 2007, **32**, 1539–1541.
 - 31 U. Megerle, I. Pugliesi, C. Schrieffer, C. F. Sailer and E. Riedle, *Appl. Phys. B Lasers Opt.*, 2009, **96**, 215–231.
 - 32 G. Ghosh, *J. Am. Ceram. Soc.*, 1997, **36**, 1540–1546.
 - 33 M. Ziólek, M. Lorenc and R. Naskrecki, *Appl. Phys. B Lasers Opt.*, 2001, **72**, 843–847.
 - 34 M. Rasmusson, A. N. Tarnovsky, E. Åkesson and V. Sundström, *Chem. Phys.*

- Lett.*, 2001, **335**, 201–208.
- 35 I. H. M. Van Stokkum, D. S. Larsen and R. Van Grondelle, *Biochim. Biophys. Acta - Bioenerg.*, 2004, **1657**, 82–104.
- 36 K. M. Mullen and I. H. M. van Stokkum, *J. Stat. Softw.*, 2007, **18**, 1–46.
- 37 J. J. Snellenburg, S. P. Liptonok, R. Seger, K. M. Mullen and I. H. M. van Stokkum, *J. Stat. Softw.*, 2012, **49**, 1–22.
- 38 I. H. M. Van Stokkum, *IEEE Trans. Instrum. Meas.*, 1997, **46**, 764–768.
- 39 G. H. Golub and V. Pereyra, *SIAM J. Numer. Anal.*, 1973, **10**, 413–432.
- 40 M. P. Grubb, A. J. Orr-Ewing and M. N. R. Ashfold, *Rev. Sci. Instrum.*, 2014, **85**, 064104.

3 Photoprotection Properties of Mycosporine Amino Acid Motifs



This Chapter is based on the following publication:

J. M. Woolley, M. Staniforth, M. D. Horbury, G. W. Ritchings, M. Wills and V. G. Stavros, Unravelling the Photoprotection Properties of Mycosporine Amino Acid Motifs, *J. Phys. Chem. Lett.*, 2018, **9**, 3043–3048.

Synthesis of samples was performed by Professor Martin Wills, Department of Chemistry, University of Warwick.

Calculations displayed in Table 3.2 were performed by Dr Gareth W. Ritchings, Department of Chemistry, University of Warwick.

3.1 Introduction

Identification of new UV filters for use in commercial formulations has resulted in the use of naturally inspired systems to help derive safer UV filters. As discussed in Chapter 1, one such class receiving attention are mycosporines and mycosporine-like amino acids (herein referred to as MAAs).^{1,2} MAAs exhibit a strong absorption band in the UV region of the electromagnetic spectrum. MAAs share a common cyclohexenone or cyclohexenimine core, with their additional functional groups determining their specific absorption maximum. While many articles exist exploring the presence and extraction of MAAs,³⁻⁷ experimental information pertaining to their ultrafast photochemistry is absent. This information, along with complementary studies of longer (nanosecond) temporal duration,⁸⁻¹⁰ can provide important insight into the molecules' ability to provide photoprotection.

Recent theoretical work, discussed in detail in Chapter 1, has explored the excited state potential energy landscape of a selection of model MAA analogues.¹¹ These studies indicate that upon photoexcitation of molecules containing a cyclohexenone core, the excited state population traverses the excited state potential before becoming trapped within the excited state minimum. For those that have a cyclohexenimine core, photoexcitation to the first excited state is followed by rapid relaxation along an out of plane flexing motion, leading to an accessible conical intersection (CI) promoting ground state repopulation, consistent with previous theoretical studies on a common MAA palythine.¹²

To shed further insight into these excited state decay pathways, time-resolved transient electronic absorption spectroscopy (TEAS) combined with a molecular *bottom-up* approach,¹³ was employed to study simplified chromophore subunits (i.e. motifs) of MAAs. The systems chosen to act as analogues are 3-aminocyclohex-2-en-1-one (termed ACyO) and (Z)-N-(3-(butylamino)-2-methylcyclohex-2-en-1-ylidene)butan-1-aminium 4-methylbenzenesulfonate (termed NN) both shown in Figure 3.1. These molecules present similar core structures to that of MAAs and similar species have been explored computationally for their photoprotection capabilities.¹¹

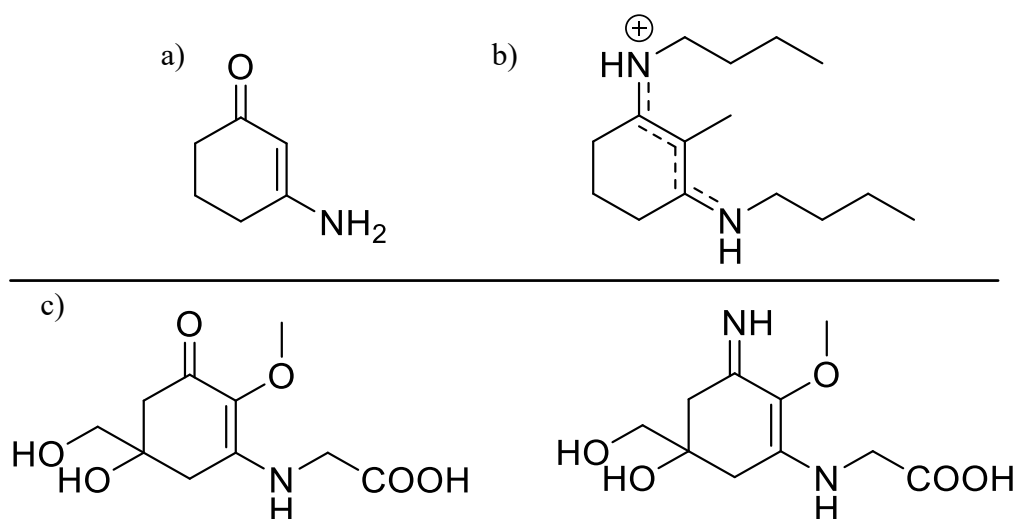


Figure 3.1 Structures of a) 3-aminocyclohex-2-en-1-one termed ACyO, b) (Z)-N-(3-(butylamino)-2-methylcyclohex-2-en-1-ylidene)butan-1-aminium 4-methylbenzenesulfonate termed NN, c) two common MAAs mycosporine-glycine (left) and palythine (right).

3.2 Experimental Methodology

3.2.1 Synthesis and Characterisation

Samples of ACyO were obtained from Alfa Aesar (95% purity) and used without any further purification. NN was synthesised by Professor Martin Wills (Department of Chemistry, University of Warwick), following a previously reported procedure,¹¹ briefly described here. 1 mM of 2-methyl-1,3-cyclohexanedione and 1 mM *p*-toluenesulfonic acid monohydrate were added to 10 ml of *n*-butylamine (all Sigma-Aldrich) and then refluxed under N₂ for 48 hours. The resulting solution was concentrated under vacuum and purified through crystallization from CH₂Cl₂ and washed with sequential washes of *n*-hexane. Samples were confirmed through comparison with previously reported ¹H NMR spectra.

3.2.2 Experimental Details

A complete explanation of the laser pulse generation and data collection utilised in these measurements is described in Section 2.3; particular details relating to these measurements are detailed below. Samples of both ACyO and NN were dissolved at 10 mM concentrations in acetonitrile (Sigma Aldrich >99%) and methanol (fisher scientific >99%). Excitation wavelengths were chosen as the absorption maximum for each solvent corresponding to 272 nm and 285 nm for acetonitrile and methanol respectively for ACyO and 328 nm in both solvents for NN. A pump fluence of 0.3 mJcm⁻² and a sample path length of 100 μm was used for all TEAS experiments.

All steady-state UV/Vis measurements were performed on a LAMBDA 850 spectrophotometer, using a quartz cuvette with a 1 cm path length.

3.2.3 Calculations

Calculations were performed by Dr Gareth W. Ritchings (Department of Chemistry, University of Warwick) in Molpro using 2 state-averaged CASSCF with a 6-31G* basis set for ACyO only.¹⁴ The CASSCF calculations used an active space of 8 electrons in 6 orbitals, the four occupied orbitals being the 3 π -orbitals as well as the lone pair perpendicular to the CO bond and the 2 unoccupied orbitals being the π^* orbitals. Configuration interaction singles calculations indicated that the excited states contained mainly contributions from these orbitals, with none from the second lone pair on the oxygen (parallel to the CO bond).

3.3 Results

3.3.1 Sample Characterisation

Presence of NN after synthesis was confirmed through ¹H NMR and UV/Vis spectra shown in Figure 3.2, against a previous reports.¹¹

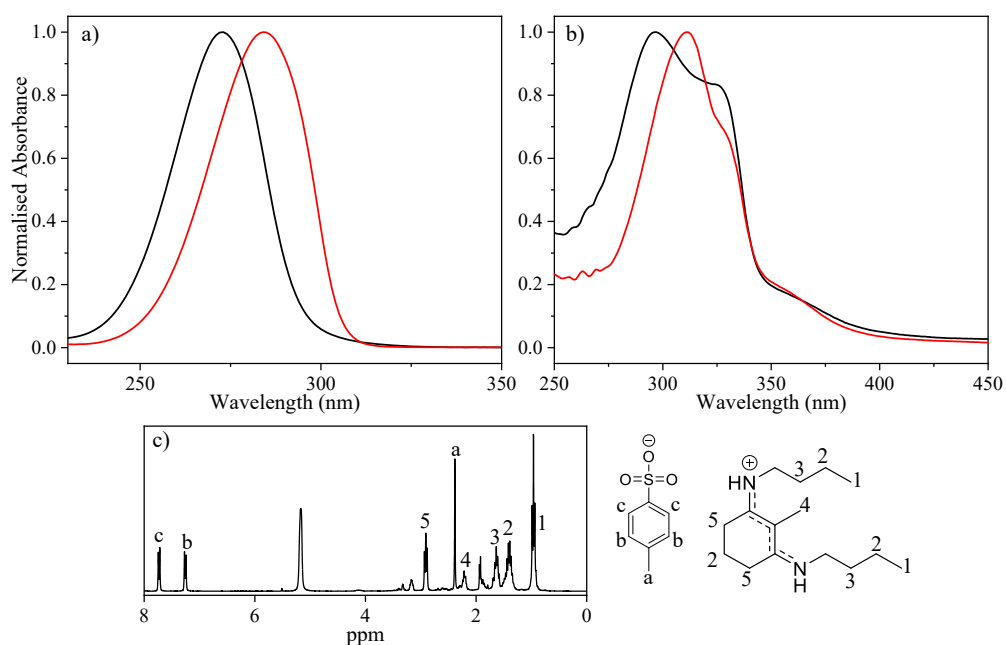


Figure 3.2 Steady-state UV/Vis spectra of a) ACyO in acetonitrile (black) and methanol (red), b) NN in acetonitrile (black) and methanol (red), c) ¹H NMR of NN and TsO⁻ counter ion in deuterated methanol.

3.3.2 Transient Electronic Absorption Spectroscopy Measurements

Collected transient absorption spectra (TAS) for ACyO in both solvents is displayed in Figure 3.3. There are evident differences between the two false colour heat maps. In acetonitrile (Figure 3.3a) an aprotic polar solvent, upon photoexcitation at the absorption maximum ($\lambda_{\text{max}} = 272$ nm) the initial TAS (pump-probe time delay, $\Delta t < 6$ ps) displays a broad excited state absorption (ESA) spanning from 340 to 600 nm. As Δt increases, the ESA feature begins to blue-shift and narrow, centering at 370 nm with increased intensity. This feature persists to the maximum available Δt of the measurements, 2.5 ns. The TAS of ACyO in methanol (Figure 3.3b, $\lambda_{\text{max}} = 285$ nm), a polar protic solvent, displays markedly different features to those of the ACyO in acetonitrile. After initial photoexcitation, the first feature is an intense ESA peaked at 350 nm which is short lived ($\Delta t < 1$ ps). Finally, a second, less intense ESA feature centred at 400 nm grows in after $\Delta t \sim 10$ ps, which then persists to the maximum Δt of 2.5 ns.

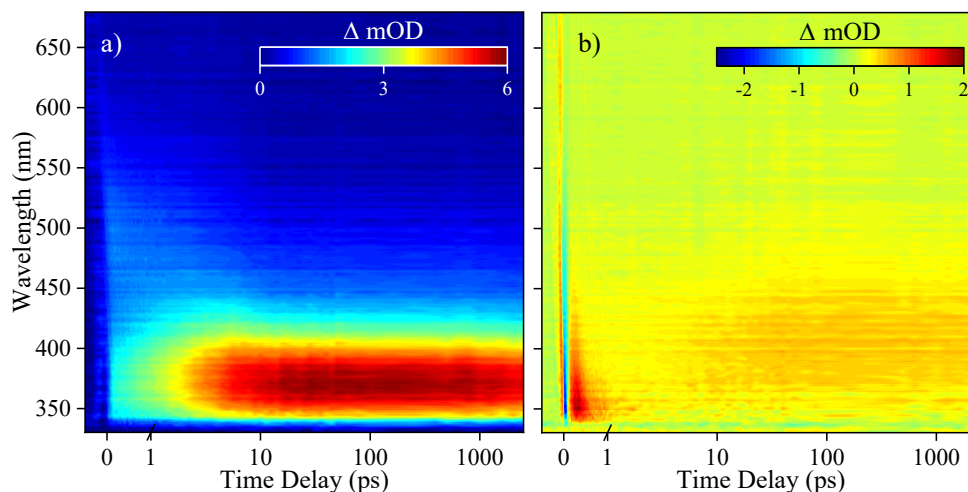


Figure 3.3 False colour heat maps of TAS of 10 mM ACyO in a) acetonitrile excited at 272 nm and b) methanol excited at 285 nm. The pump-probe time delay is plotted linearly from -0.5 ps to 1 ps and then logarithmically to 2.5 ns.

In contrast to ACyO, the TAS of NN photoexcited at 328 nm do not (visibly) display a dependence on solvent, as evidenced in Figure 3.4. The TAS in each solvent show an ESA centred at 350 nm which initially extends to 400 nm, then narrows and returns to baseline within 15 ps. Mildly visible in the TAS is a ground state bleach (GSB) centred at 340 nm at early time (< 1 ps), along with a stimulated emission (SE) from 350 nm to the end of the probe region (680 nm). A weak absorption is also visible for

the maximum Δt (2.5 ns) centred at 390 nm. These latter features are more apparent in the evolution associated difference spectra (EADS), Figure 3.5, discussed below.

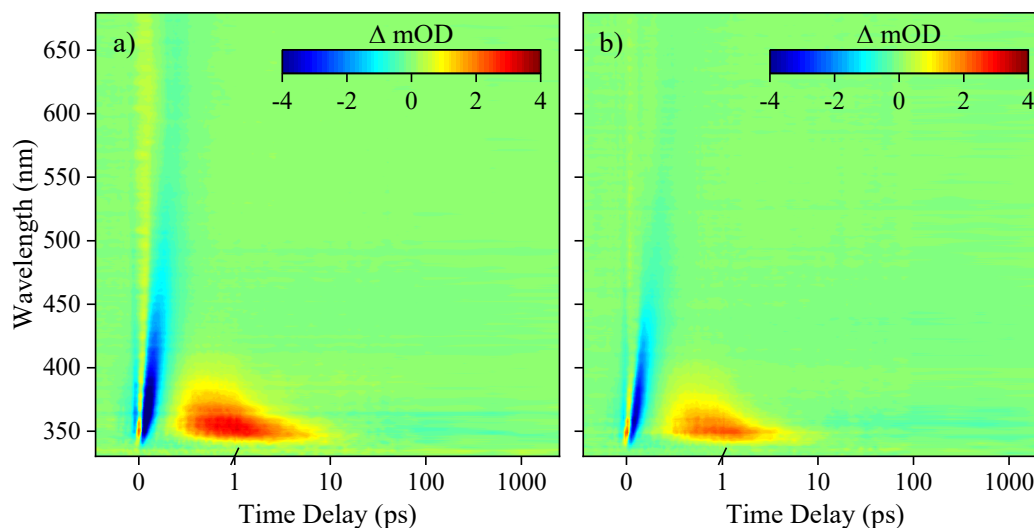


Figure 3.4 False colour heat maps of TAS of 10 mM NN following photoexcitation at 328 nm in a) acetonitrile and b) methanol. The pump-probe time delay is plotted linearly from -0.5 ps to 1 ps and then logarithmically to 2.5 ns.

3.4 Discussion

For both motifs (ACyO and NN) dynamical information was extracted through a global sequential fitting model ($A \xrightarrow{\tau_1} B \xrightarrow{\tau_2} C \xrightarrow{\tau_3} D$), performed in Glotaran.^{15,16} The extracted lifetimes, τ_n , describing the time scale for each step in the relaxation process, are shown in Table 3.1. The corresponding EADS are also shown in Figure 3.5. The quality of each fit was evaluated through the associated residuals displayed in Figure S3.1 of the supporting information of this Chapter. Further information pertaining to the fitting procedure (along with a description of the origin of the residuals) is available in Section 2.4.

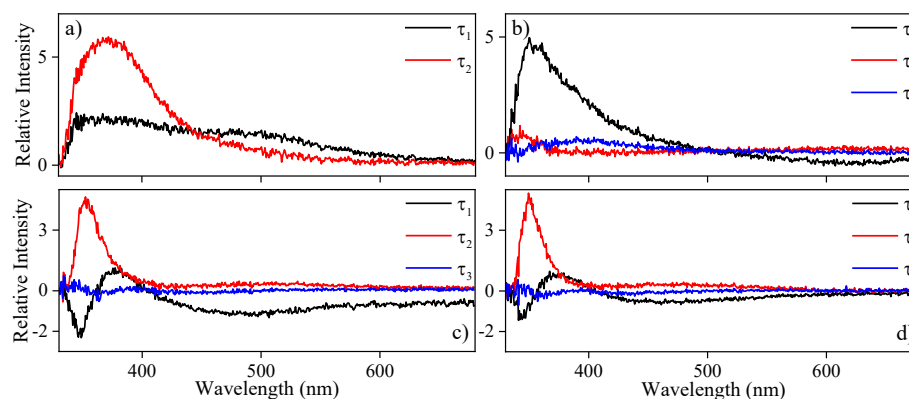


Figure 3.5 EADS for the TAS of ACyO and NN. a) ACyO in acetonitrile photoexcited at 272 nm. b) ACyO in methanol photoexcited at 285 nm. c) NN in acetonitrile photoexcited at 328 nm. d) NN in methanol photoexcited at 328 nm.

Table 3.1 Lifetimes and associated errors (2σ) extracted from the global sequential fit for ACyO and NN in acetonitrile and methanol.

	τ_1	τ_2	τ_3
ACyO			
acetonitrile	2.80 ps \pm 200 fs	\gg 2.5 ns	-
methanol	330 fs \pm 50 fs	3.40 ps \pm 300 fs	\gg 2.5 ns
NN			
acetonitrile	440 fs \pm 50 fs	2.49 ps \pm 50 fs	\gg 2.5 ns
methanol	680 fs \pm 50 fs	1.52 ps \pm 100 fs	\gg 2.5 ns

Beginning the discussion with ACyO, *ab initio* calculations have shown that excitation at the absorption maximum, a $^1\pi\pi^*$ transition,¹⁷ leads to population of the first singlet excited state (S_1). From the EADS presented in Figure 3.5a, we see that the broad ESA described by τ_1 at early time is sensibly consistent with a vibrationally hot S_1 population that undergoes vibrational energy transfer, both intramolecular and intermolecular (to the solvent), with a lifetime of $\tau_1 \approx 3$ ps. The now narrower EADS associated with τ_2 is assigned to vibrationally cold population trapped within the minimum of the S_1 excited state, which persists beyond the temporal duration of the experiment ($\Delta t = 2.5$ ns). This explanation is in keeping with recent theory calculations mapping the potential energy surface of the excited state of cyclohexenone units,¹¹ which indicate that as the molecule moves along the S_1 potential energy surface from the initially populated Franck-Condon region, sufficient energy is lost to the surrounding solvent environment such that the excited state population is energetically removed from the CI and thus trapped on the S_1 minimum.¹¹ Confidence in this comparison is given through complementary calculations (Table 3.2). Importantly, the CASSCF calculations at critical points along the S_1 surface (S_1 minimum and S_1/S_0 CI) reveal that mild modifications to the geometric structure appear to have little effect on the electronic structure, adding credence to the comparison between the present experiment and previous theory.¹¹ While these calculations agree with both our overall

Table 3.2 Calculated energies for the critical points for ACyO along the S_1 surface.

Vertical Excitation (eV)	S_1 Minimum (eV)	S_1/S_0 CI (eV)
4.03	3.54	3.58

assignment of the observed photodynamics and the previous studies.¹¹ They do also show that the energy gap between the calculated S_1 minimum and the S_1/S_0 conical intersection is found to be small (≈ 0.04 eV). Given this small energy barrier it is plausible that given the excess energy of 0.5 eV from the vertical excitation to the S_1 minimum that the excited state population has the potential to surmount the energy barrier and access the CI. However, as evidenced in the TAS there is clear evidence of vibrational cooling following photoexcitation either intramolecular or intermolecular to the surrounding solvent environment indicating a transfer of energy from the initial vibrationally hot solute to the surrounding solvent bath. Additionally, these calculations were performed in a vacuum environment devoid of solvent interactions which may alter the relative energies between the critical points. Calculations performed by Losantos *et al.* employing a polarizable continuum model to model the solvent environment show that the barrier to the CI is ≈ 0.2 eV.¹¹

ACyO in methanol displays different features in the TAS at early Δt and requires three lifetimes to model the TAS. The corresponding EADS are shown in Figure 3.5b. The first EADS associated with τ_1 (330 fs), which has an ESA feature peaking at 350 nm, can likely be attributed to a fast geometry relaxation on S_1 , along with any solvent rearrangement. With regards to the second EADS, associated with τ_2 (3.4 ps), this is attributed to the excited state population vibrationally cooling, *via* vibrational energy transfer, as it traverses along the excited state potential, ultimately finding its way to the minimum of the S_1 . This population persists with a lifetime (τ_3) greater than the maximum Δt of our experiment.

Two points are worthy of note with regards to the EADS collated for ACyO in methanol. Firstly, the EADS associated with τ_3 is far less intense than the EADS associated with τ_1 (when using an aprotic solvent, the opposite is the case). This is likely due to the stronger perturbations to the electronic structure, induced by the protic solvent, which will inevitably modify the transitions described by the ESA accordingly. Secondly, the need for an intermediate (τ_2) dynamical component again highlights the perturbation induced by the protic solvent. One could speculate that following evolution from the Franck-Condon region, the excited state population encounters a region on the potential energy surface where the ESA drops considerably, or there is a ESA *and* SE in competition (we see evidence of the latter in the EADS (τ_1)). This leads to almost base-line recovery in the TAS for ACyO in methanol (Figure

3.3b) observed between 1-5 ps (i.e. during vibrational energy transfer); this competition of ESA and SE could also artificially reduce τ_1 over the region. Once out of this region, the SE decreases, or the ESA increases (or both) across this spectral region.

We finally conclude our discussion on the ACyO data by noting that for both aprotic and protic solvents, we would anticipate radiative decay from a long-lived excited state. However, none was observed. The calculated gas-phase transition dipole moment between the S_1 minimum and ground electronic state (S_0) was determined to be 0.0019 Debye, which sensibly agrees with the absence of any (measurable) fluorescence signature.

Global fitting of NN in acetonitrile and methanol required three lifetimes with associated EADS shown in Figure 3.5; the lifetimes are also shown in Table 3.2. The EADS associated with τ_1 (\approx 500 fs in both solvents) consist of a GSB centred on 340 nm and an ESA peaking at 375 nm along with a shallow SE (approximately 400-680 nm). The dynamical processes responsible for this EADS are assigned to NN undergoing a fast geometry relaxation on S_1 , along with excited state population traversing through the S_1/S_0 CI. The lifetime (τ_1) for this EADS compares judiciously to dynamical calculations reported for similar type systems.¹¹ One might expect the SE to red-shift, as the excited-state population traverses the S_1 potential energy surface on route to the CI. Such a red-shift is potentially observable from the TAS, however the presence of the ESA at early times (positive feature at 375 nm) and its evolution as excited state population moves towards the CI, likely obscures this red-shift. This limits our ability to confidently track population-flow along the S_1 surface. The second EADS associated with lifetime τ_2 (2.49 ps in acetonitrile and 1.52 ps in methanol) is attributed to vibrational cooling of the vibrationally hot S_0 state. From the TAS in Figure 3.4, this is clearly manifested as a characteristic blue-shift of the absorption feature, as the ESA returns to baseline.^{18,19} The decreased lifetime for vibrational cooling in methanol compared to that to acetonitrile (1.52 to 2.49 ps) could be attributed to the hydrogen bonding between solute and solvent, with methanol being both a hydrogen bond acceptor and donator, compared to acetonitrile which is only a hydrogen bond acceptor. Additionally the charged nature of NN may also contribute to this decrease in lifetime through increased interactions with the solvent. The final EADS associated with lifetime τ_3 describes the evolution of a weak ESA. This ESA

may be reconciled by invoking a long-lived triplet state, or the appearance of a photoproduct.^{10,20}

3.5 Conclusions

To summarize, the excited state dynamics of ACyO in both aprotic (acetonitrile) and protic (methanol) solvents show that a long-lived S_1 state persists beyond the maximum Δt of the experiment and is assigned a lifetime $\gg 2.5$ ns. At early time delays, the spectral responses differ between ACyO in acetonitrile and methanol, the former showing vibrational cooling to a minimum of the S_1 potential in 2.8 ps while in the latter, the initial lifetime of 330 fs is attributed to geometry relaxation and solvent rearrangement, followed by vibrational cooling within 3.4 ps, again leading to a long-lived population in the S_1 minimum. This is consistent with our own, as well as previously reported theoretical work.¹¹ Combined, this suggests that excited state properties of cyclohexenone-based systems prevent effective repopulation of the electronic ground state on an ultrafast timescale due to the S_1/S_0 CI being energetically inaccessible (Table 3.2). These dynamical processes are shown schematically in Figure 3.6a.

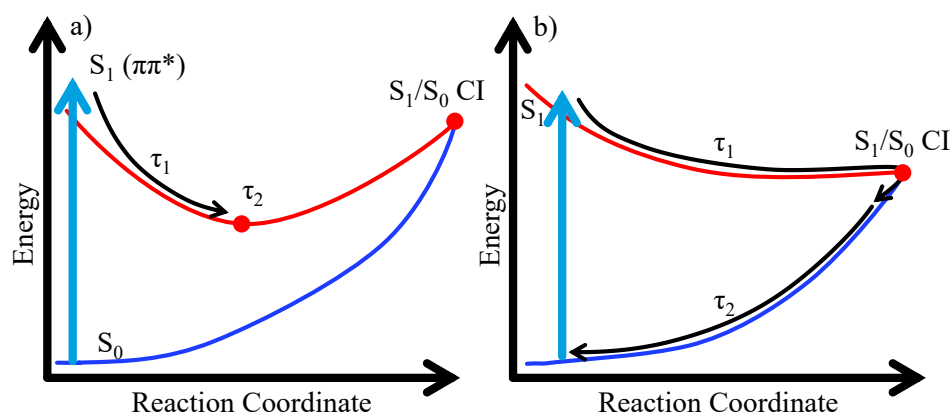


Figure 3.6 Schematic of potential energy surfaces for a) ACyO and b) NN. Note τ_3 for NN has been omitted for clarity.

These results imply that cyclohexenone-based systems should perform poorly as a photoprotective molecule due to the long-lived excited state, increasing the likelihood for potentially harmful photochemical reactions.²¹ However, prior studies on gadusol, mycosporine-glycine, and mycosporine-glutaminol-glucoside, all of which have a cyclohexanone core, demonstrate a high level of photostability.²²⁻²⁴ This is likely due to the absence of a localized energy minimum in the S_1 state before the S_1/S_0 CI, as

seen in gadusol,²⁵ and evidenced in the present studies on NN. Therefore, the photostability of cyclohexenone-based systems seems to be due to additional functional groups present, rather than an intrinsic property of the cyclohexanone core. We add here the potential importance of the methoxy group at the *ortho* position as many MAAs possess this functionality at this position.² Such a finding therefore lends itself to further studies exploring the degree of functionalisation (as well as the nature of the functionalities) required to induce photostability to the cyclohexanone core.

In comparison, NN displays electronic excited state dynamics which are largely independent of solvent environment. From the initial photoexcited population, the system returns to a vibrationally hot S_0 state in ≈ 500 fs. Once in the vibrationally hot S_0 state, the timescales for vibrational relaxation, *via* intermolecular energy transfer to the solvent, do display a dependence upon the solvent environment. The timescale for this vibrational relaxation is shorter in methanol (1.52 ps), a hydrogen bonding donor and acceptor, compared to acetonitrile (2.49 ps), which is only a hydrogen bonding acceptor. Interestingly, this correlates well with recent work by Koizumi *et al.*, which demonstrates that hydrogen bonding to the solvent (water) plays a vital role in vibrational relaxation of porphyrin-334.²⁶ This is once again shown schematically in Figure 3.6b. The remaining photoexcited population persists for the duration of the experiment, either as a populated triplet state or through the formation of a (likely low quantum yield) photoproduct. We emphasise once more that the short timescales for vibrational energy transfer in NN may be a consequence of its charged nature, which will inevitably influence NN-solvent interaction. Importantly, the presently reported dynamics of NN show promising properties as a future species of UVR absorbing compound.

3.6 Supporting Information

3.6.1 Fitting Residuals

Extracted fitting residuals from TAS of ACyO and NN, collected when fitting with a multi-step sequential model.

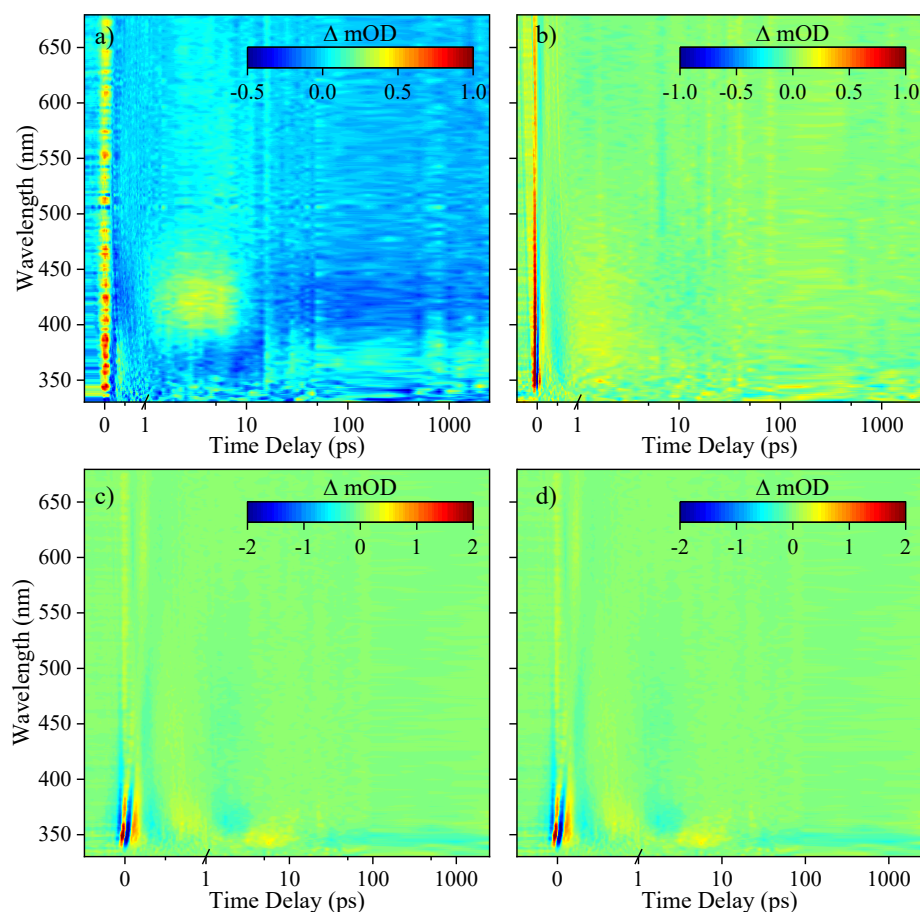


Figure S3.1 False colour heat maps of fitting residuals for ACyO and NN. a) ACyO in acetonitrile excited at 272 nm. b) ACyO in methanol excited at 285 nm. c) NN in acetonitrile excited at 328 nm. d) NN in methanol excited at 328 nm. The pump-probe time delay is plotted linearly from 0.5 ps to 1 ps and then logarithmically to 2.5 ns.

3.6.2 Power Dependencies

Power dependencies of ACyO and NN show a linear dependence across the spectral features of the TAS. These measurements were achieved by varying the TOPAS output power and taking a 10 nm integration window across a particular spectral window at a given pump-probe time delay. Each TAS displays a linear relationship to the incident pump power ($\log(\text{signal})$ vs. $\log(\text{power})$ plots), strongly suggesting single photon induced dynamics.

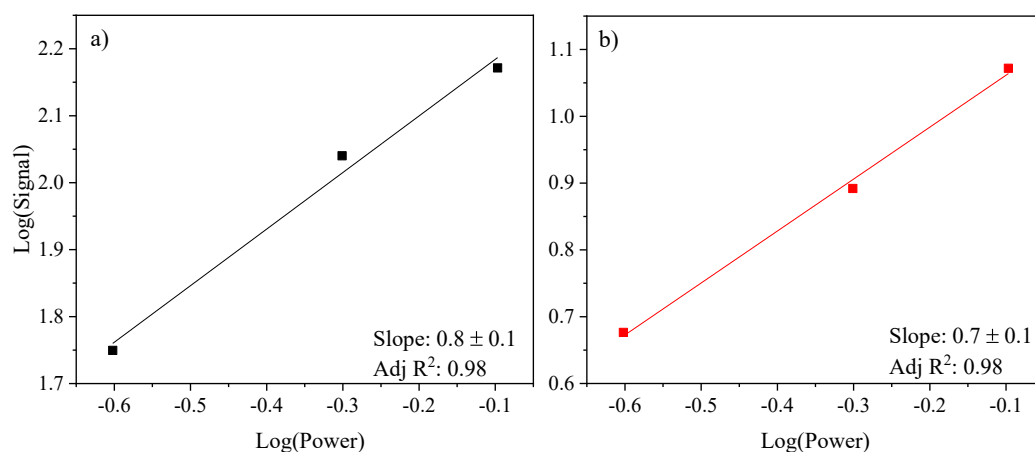


Figure S3.2 Power dependencies for the integrated intensity for ACyO in: a) Acetonitrile following excitation at 272 nm; 10 nm integration window, 365-375 nm, at $\Delta t = 1$ ns. b) Methanol following excitation at 285 nm; 10 nm integration window, 395-405 nm, at $\Delta t = 1$ ns.

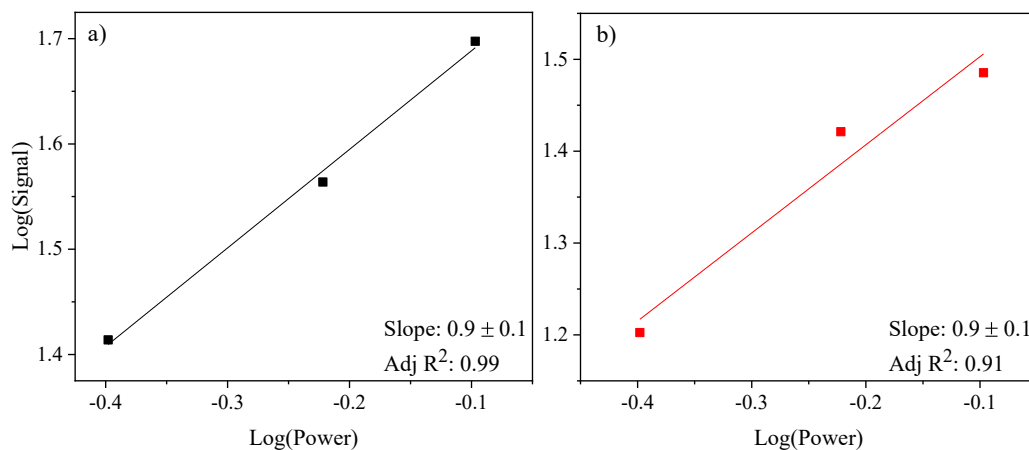


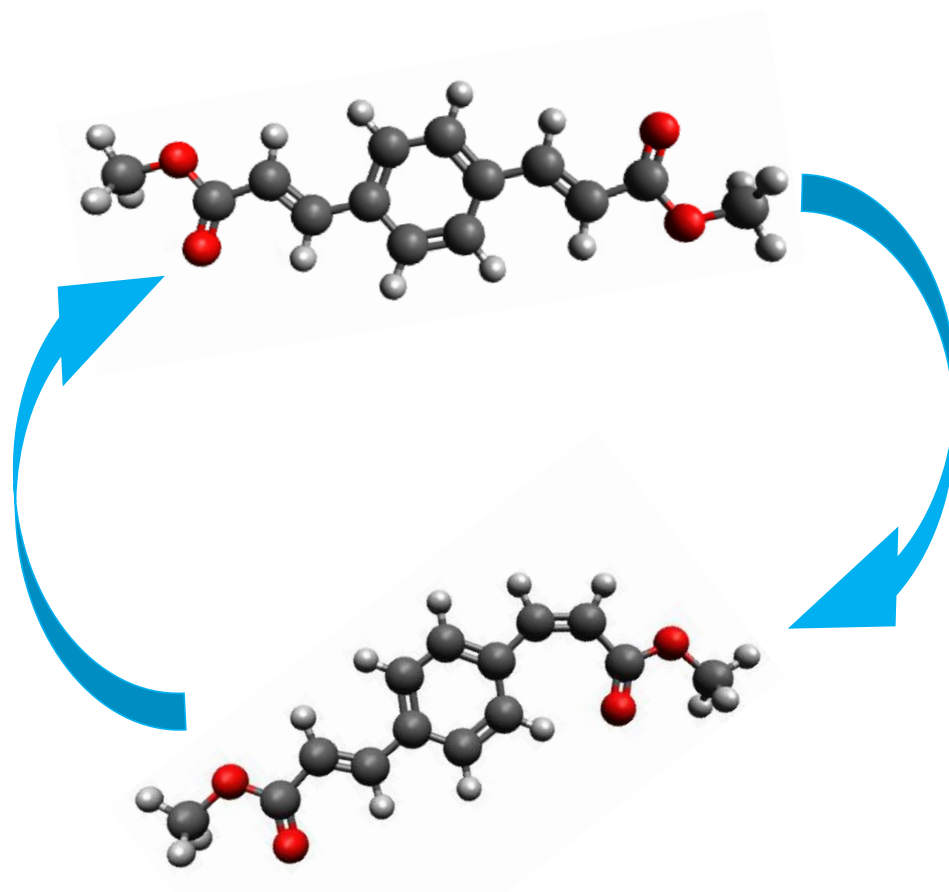
Figure S3.3 Power dependencies for the integrated intensity for NN following excitation at 328 nm for the integrated intensity of a 10 nm window, 345-355 nm at $\Delta t = 1$ ps a) acetonitrile and b) methanol.

3.7 Bibliography

- 1 W. M. Bandaranayake, *Nat. Prod. Rep.*, 1998, **15**, 159–172.
- 2 Q. Gao and F. Garcia-Pichel, *Nat Rev Microbiol*, 2011, **9**, 791–802.
- 3 R. P. Sinha, M. Klisch and D. H., *J. Photochem. Photobiol. B Biol.*, 1998, **1344**, 83–94.
- 4 J. M. Shick and W. C. Dunlap, *Annu. Rev. Physiol.*, 2002, **64**, 223–262.
- 5 E. W. Schmidt, *ChemBioChem*, 2011, **12**, 363–365.
- 6 A. R. Osborn, K. H. Almabruk, G. Holzwarth, S. Asamizu, J. LaDu, K. M. Kean, P. A. Karplus, R. L. Tanguay, A. T. Bakalinsky and T. Mahmud, *Elife*, 2015, 1–15.
- 7 F. Garcia-Pichel and R. W. Castenholz, *Appl. Environ. Microbiol.*, 1993, **59**, 163–169.
- 8 R. Losantos, D. Sampedro and M. S. Churio, *Pure Appl. Chem.*, 2015, **87**, 979–996.
- 9 F. R. Conde, M. S. Churio and C. M. Previtali, *Photochem. Photobiol. Sci.*, 2004, **3**, 960–967.
- 10 F. R. Conde, M. S. Churio and C. M. Previtali, *Photochem. Photobiol. Sci.*, 2007, **6**, 669–674.
- 11 R. Losantos, I. Funes-Ardoiz, J. Aguilera, E. Herrera-Ceballos, C. García-Iriepa, P. J. Campos and D. Sampedro, *Angew. Chemie Int. Ed.*, 2017, **56**, 2632–2635.
- 12 D. Sampedro, *Phys. Chem. Chem. Phys.*, 2011, **13**, 5584–6.
- 13 G. M. Roberts and V. G. Stavros, *Chem. Sci.*, 2014, **5**, 1698.
- 14 H. J. Werner, P. J. Knowles, G. Knizia, F. R. Manby and M. Schütz, *Wiley Interdiscip. Rev. Comput. Mol. Sci.*, 2012, **2**, 242–253.
- 15 K. M. Mullen and I. H. M. van Stokkum, *J. Stat. Softw.*, 2007, **18**, 1–46.
- 16 J. J. Snellenburg, S. P. Laptanok, R. Seger, K. M. Mullen and I. H. M. van Stokkum, *J. Stat. Softw.*, 2012, **49**, 1–22.

- 17 X. X. Sui, L. Li, Y. Zhao, H. G. Wang, K. M. Pei and X. Zheng, *Spectrochim. Acta - Part A Mol. Biomol. Spectrosc.*, 2012, **85**, 165–172.
- 18 N. A. Anderson, S. H. Pullen, L. A. Walker II, J. J. Shiang and R. J. Sension, *J. Phys. Chem. A*, 1998, **102**, 10588.
- 19 J. M. L. Pecourt, J. Peon and B. Kohler, *J. Am. Chem. Soc.*, 2001, **123**, 10370–10378.
- 20 M. D. Horbury, L. A. Baker, N. D. N. Rodrigues, W.-D. Quan and V. G. Stavros, *Chem. Phys. Lett.*, 2017, **673**, 62–67.
- 21 N. D. N. Rodrigues, M. Staniforth and V. G. Stavros, *Proc. R. Soc. A*, 2016, **472**, 20160677.
- 22 M. Moliné, E. M. Arbeloa, M. R. Flores, D. Libkind, M. E. Farías, S. G. Bertolotti, M. S. Churio and M. R. van Broock, *Radiat. Res.*, 2011, **175**, 44–50.
- 23 E. M. Arbeloa, S. G. Bertolotti and M. S. Churio, *Photochem. Photobiol. Sci.*, 2011, **10**, 133–42.
- 24 R. P. Rastogi and A. Incharoensakdi, *Photochem. Photobiol. Sci.*, 2014, **13**, 1016–1024.
- 25 R. Losantos, M. S. Churio and D. Sampedro, *ChemistryOpen*, 2015, **4**, 155–160.
- 26 K. Koizumi, M. Hatakeyama, M. Boero, K. Nobusada, H. Hori, T. Misonou and S. Nakamura, *Phys. Chem. Chem. Phys.*, 2017, **19**, 15745–15753.

4 Symmetric Functionalisation Effects on the Photoisomerisation Pathway of a UV Filter



This Chapter is based on the following publication:

J.M. Woolley, J.S. Peters, M.A.P. Turner, G.J. Clarkson, M.D. Horbury and V.G. Stavros, The Role of Symmetric Functionalisation on Photoisomerisation of a UV Commercial Chemical Filter, *Phys. Chem. Chem. Phys.*, 2019, **21**, 14350-14356.

Synthesis of *p-E,E*-DPD was performed by Mr Jack S. Peters and Dr Guy J. Clarkson, Department of Chemistry, University of Warwick.

Calculations displayed in Table 4.1 were performed by Mr Matthew A.P. Turner Department of Chemistry, University of Warwick.

4.1 Introduction

Current UV filters such as those discussed in Chapter 1 have been selected due to their absorbance of UVR thus preventing the exposure of human cells to dangerous levels of UVR. 2-ethylhexyl-E-4-methoxycinnamate (*E*-EHMC) is one such molecule that is currently approved for use both in the EU and US.^{1,2} Both *E*-EHMC and its mimic methoxy methyl cinnamate provide the required photoprotection through photoisomerisation. Photoisomerisation has been shown to be an efficient excited state relaxation mechanism for a variety of nature-based molecular systems,³ and the photodynamics of *E*-EHMC have also been previously explored.⁴ These studies have shown that, following UV excitation to the first excited electronic (S_1) state, *E*-EHMC undergoes ultrafast relaxation, repopulating the ground electronic (S_0) state through an energetically accessible S_1/S_0 conical intersection (CI), with a portion forming *Z*-EHMC.⁴⁻⁷ The formation of *Z*-EHMC is cause for concern as recent studies suggest its adverse effects on human liver cells.⁸ These reports follow a growing trend of UV filters with harmful photoproducts, both to humans and also to the environment, triggered by photoexcitation.⁸⁻¹¹ As such, there is mounting impetus to develop ‘safer’ UV filters for use in formulations, such as variants/derivatives of current commercial UV filters.

The work in this Chapter takes current knowledge on photoisomerisation in these cinnamate systems one step further. It assesses the influence of symmetric functionalisation of cinnamates through the addition of a second methyl acrylate moiety onto the base cinnamate, methyl cinnamate (highlighted in red, Figure 4.1). This gives rise to (potentially) three distinct geometric isomers: dimethyl 3,3'-(1,4-phenylene)(2*E*,2'*E*)-diacrylate, dimethyl 3,3'-(1,4-phenylene)(2*Z*,2'*E*)-diacrylate and dimethyl 3,3'-(1,4-phenylene)(2*Z*,2'*Z*)-diacrylate, henceforth termed *p*-*E*,*E*-DPD, *p*-*E*,*Z*-DPD and *p*-*Z*,*Z*-DPD respectively and all shown in Figure 4.1 along with the ground state absorption profiles in differing solvents.

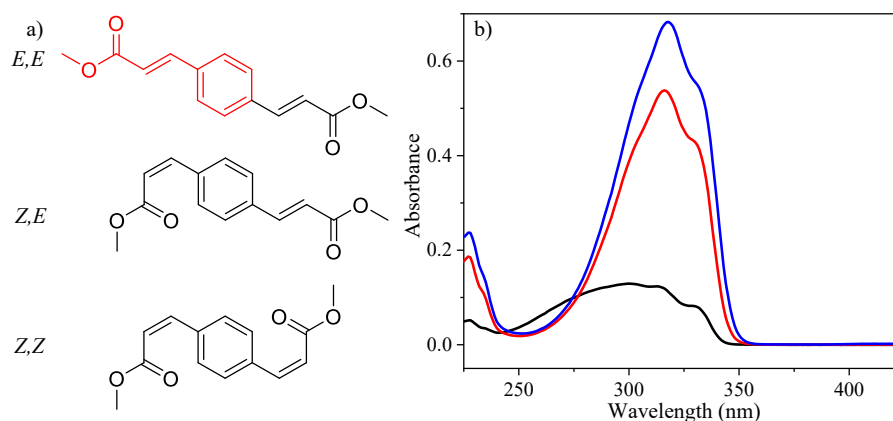


Figure 4.1 a) Three possible structures of DPD with the base methyl cinnamates structure highlighted in red, b) steady-state UV/Vis absorption spectra for *p-E,E*-DPD in various solvents, blue: ethanol, red: acetonitrile (10 μ M concentration) and black: cyclohexane (< 10 μ M).

4.2 Experimental Methodology

4.2.1 Synthesis and Characterisation

DPD was prepared using a method adapted from the literature,¹² by Mr Jack, S. Peters and Dr Guy J. Clarkson (Department of Chemistry, University of Warwick). 5 drops of dimethylformamide (99.8% purity, Sigma-Aldrich) were added to a mixture of 1 g *p*-phenylenediacrylic acid (97% purity, Sigma-Aldrich) and 10 ml thionyl chloride (97% purity, Sigma-Aldrich) and was refluxed overnight. The mixture was allowed to cool and the excess of thionyl chloride was removed at reduced pressure to give a yellow powder. 50 ml of methanol (99% purity, Alfa-Aesar) was added gradually to the powder, which started to reflux due to the exothermic nature of the reaction. The mixture was refluxed for 4 hours and then the solid was isolated via filtration. The reaction mixture was analysed using thin layer chromatography with dichloromethane (DCM, 99.8% purity, Sigma-Aldrich) as an eluent, which showed that the starting material had been consumed and that multiple new spots were visualised under UV irradiation. The mixture was recrystallized using a 2:1 solution of DCM and petrol (Sigma-Aldrich), to form a light-yellow crystalline product. The resulting compound was analysed using ^1H , NMR displayed in Figure 4.2.

4.2.2 Experimental Details

A detailed explanation of the laser pulse generation and data collection utilised in these measurements is described in Section 2.3; thus only particular details relating to these measurements are given below. Samples of *p-E,E*-DPD were dissolved at 1 mM concentrations in cyclohexane, acetonitrile (both fisher scientific >99%) and ethanol

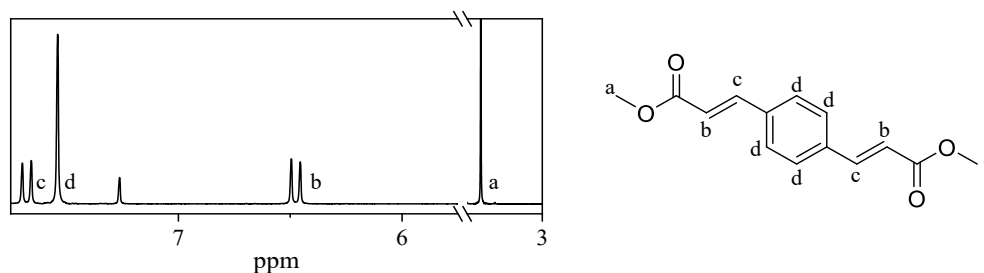


Figure 4.2 ¹H NMR of synthesised product *p*-*E,E*-DPD.

(VWR >99%). Excitation wavelengths were chosen in two locations for each solvent corresponding to distinct features in the UV/Vis spectrum; in cyclohexane, the sample was excited at 315 nm and 329 nm, in acetonitrile at 317 nm and 327 nm, and 318 nm and 329 nm when solvated in ethanol. A sample path length of 100 μm was used for all Transient Electronic Absorption Spectroscopy (TEAS) experiments, with pump fluence of 0.25 mJcm^{-2} .

Steady-state UV/Vis and steady-state measurements were taken on a Cary 60 at ~ 10 μM concentrations in ethanol and acetonitrile, and < 10 μM in cyclohexane (Figure 4.1). Steady-state irradiation (of varying times, up to a maximum of 2 hours) measurements were taken using a Horiba FluoroLog-3, with an 8 nm slit width centred on the TEAS excitation wavelength and irradiation power equal to that of solar irradiance. Samples (each 10 mM, < 10 mM in cyclohexane) for ¹H NMR analysis were irradiated for 1 hr using the full available power of the Xenon lamp at the TEAS excitation wavelength using an 8 nm slit width. Samples were then dried of solvent and subsequently dissolved in deuterated chloroform for ¹H NMR analysis. A quartz cuvette with a 1 cm path length was used for UV/Vis, steady-state irradiation and ¹H NMR irradiation measurements.

4.2.3 Calculations

The calculations reported here for DPD were performed by Mr Matthew A.P. Turner (Department of Chemistry, University of Warwick). Structures of DPD were generated for all three isomers (*E,E*, *E,Z*, *Z,Z*), using Visual Molecular Dynamics,¹³ with the molefactory plugin. Each of these structures underwent a geometry optimization within density functional theory (DFT) using a cc-pVTZ basis set and PBE0 functional,^{14,15} using the NWChem software.¹⁶ Following this, vertical excitations using time-dependant DFT (TD-DFT) calculations were conducted on the optimized geometries of the *E,E*, *E,Z* and *Z,Z* forms. Again, the level of theory was

cc-pVTZ/PBE0 and the NWChem software was employed, generating the vertical excitation energies along with the oscillator strengths for each transition. For all calculations, a conductor-like screening model (COSMO) was used to replicate the effect of the solvent.^{17,18} The default COSMO implicit solvent model for each environment within NWChem was used, the descriptors of which are based on the Minnesota Solvent Descriptor Database.¹⁹

4.3 Results

4.3.1 Sample Characterisation

The dominant product of the synthesis was found to be *p-E,E*-DPD, determined through analysis of the ¹H NMR spectra. Computed structures predict that the lowest energy structure is the *E,E*-isomer, showing good agreement with the structure assigned through the ¹H NMR shown in Figure 4.2. Table 4.1 shows the calculated energy difference between the three isomers, along with the first singlet vertical excitations of each isomer in each solvents.

Table 4.1 Energies of the three possible geometric isomers of DPD, relative to the energy of *p-E,E*-DPD, along with first singlet excitation (vertical) energies and transition oscillator strengths, in acetonitrile, ethanol and cyclohexane.

Solvent	Isomer	<i>E,E</i>	<i>E,Z</i>	<i>Z,Z</i>
Acetonitrile	Ground state difference relative to <i>p-E,E</i> -DPD (eV)	0	0.27	0.54
	Vertical excitation energies (eV/nm)	3.79/327	3.80/326	3.81/325
	Transition oscillator strength	1.30	1.17	1.08
Ethanol	Ground state difference relative to <i>p-E,E</i> -DPD (eV)	0	0.27	0.55
	Vertical excitation energies (eV/nm)	3.76/330	3.80/326	3.81/325
	Transition oscillator strength	1.31	0.94	0.80
Cyclohexane	Ground state difference relative to <i>p-E,E</i> -DPD (eV)	0	0.35	0.58
	Vertical excitation energies (eV/nm)	3.80/326	3.81/325	3.81/325
	Transition oscillator strength	1.28	1.16	1.06

4.3.2 Steady-State Spectroscopy Measurements

Steady-state irradiation spectra of *p-E,E*-DPD in each solvent are displayed in Figure 4.3 taken at solar irradiance (approximately 50 μW) centred on the maximum absorption for each solvent; 318, 317 and 315 nm for ethanol, acetonitrile and cyclohexane, respectively. From the overall spectral shape of the spectra presented in Figure 4.3 there is a dependence on the solvent polarity. The most polar environment, ethanol, shown in Figure 4.3a shows a narrower absorption profile at the blue edge of the spectrum compared to the absorption profile in cyclohexane, the least polar environment, shown in Figure 4.3b. This change in absorption profile indicates that the energies or transition dipole moments of electronic excited states is affected by changes to the solvent polarity. However, from our calculations all the excitations are $\pi\pi^*$ in character showing that this shifting of the electronic states has little effect in the explored dynamics. All the steady-state irradiation spectra show a depletion of the initial main peak before plateauing following 20 minutes (1200 seconds) of irradiation. This plateauing and the formation of isosbestic point suggests the formation of a photoequilibrium between two species. Accompanying this depletion is a small shift in the absorption to higher energy. To further prove the existence of this photoequilibrium, and to determine whether the isomerisation involves one double bond (i.e. to generate the *p-E,Z*-DPD) or both double bonds (to generate the *p-Z,Z*-DPD), ^1H NMR of the irradiated samples was performed. The samples were irradiated for 1 hr at the absorption maximum ($\lambda_{\text{max}} = 318, 317$ and 315 nm, for ethanol, acetonitrile and cyclohexane respectively) and the resulting ^1H NMRs for each solvent

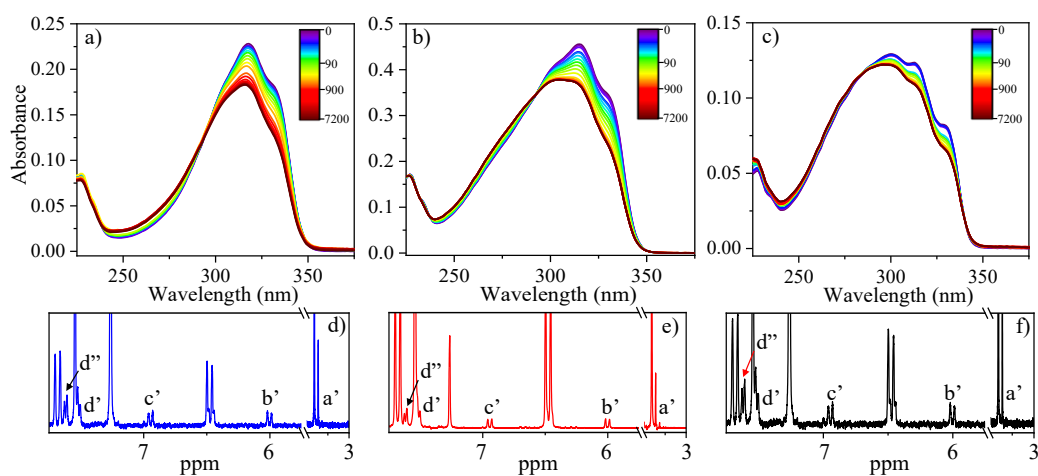


Figure 4.3 Steady-state irradiation spectra of *p-E,E*-DPD for each solvent with the colour bar indicating irradiation time in seconds, alongside NMR of irradiated samples following 1 hour of irradiation in each solvent: a) and d) ethanol; b) and e) acetonitrile; finally c) and f) cyclohexane. Assignments of peaks are associated with those of Figure 4.2.

Symmetric Functionalisation Effects on the Photoisomerisation Pathway of a UV Filter | Results

are displayed in Figure 4.3. All three of the solvents show the formation of new hydrogen environments attributed to $E \rightarrow Z$ isomerisation. The peaks c' and b' showing 13 Hz splitting, and the formation of d' and d'' indicate that the sample is unsymmetrical with respect to the substituents, consistent with p - E,Z -DPD and not p - Z,Z -DPD.

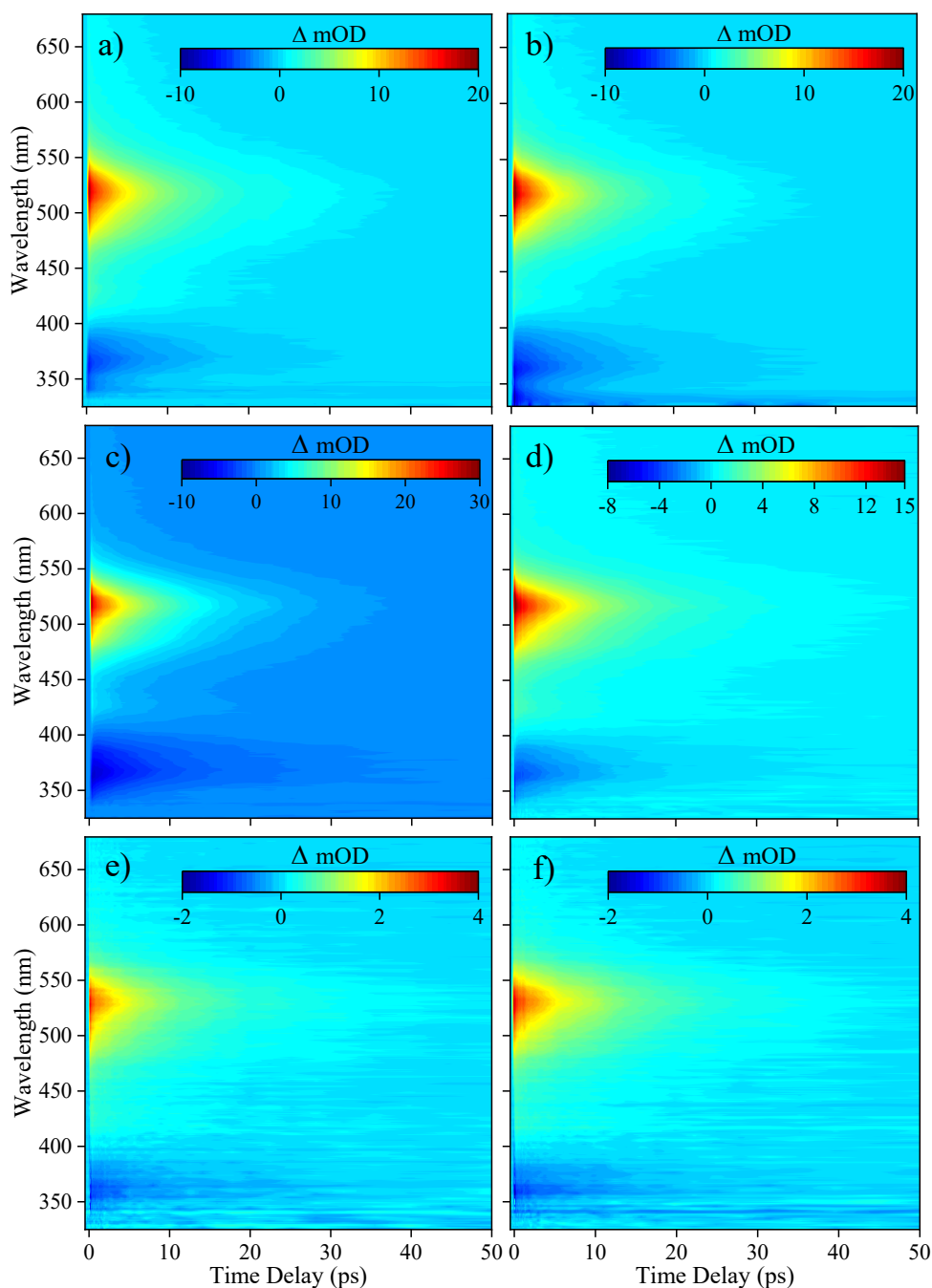


Figure 4.4 False colour heat maps for TAS of p - E,E -DPD in ethanol: a) excited at 318 nm and b) excited at 329 nm, acetonitrile c) excited at 317 nm and d) excited at 327 nm and cyclohexane e) excited at 315 nm and f) excited at 329 nm.

4.3.3 Transient Electronic Absorption Spectroscopy Measurements

Collected transient absorption spectra (TAS) of *p-E,E*-DPD in the three solvents is displayed as false colour heat maps in Figure 4.4. All TAS show the same two main features: a stimulated emission (SE) centred at 375 nm and a strong excited state absorption (ESA) centred at 525 nm. Also of note here is that a small ESA persists to the maximum temporal duration of the experiment (2.5 ns), along with a ground state bleach feature (GSB); both of which are not immediately apparent in the heat maps; for clarity Figure 4.5 shows TAS taken at $\Delta t = 2.5$ ns in each solvent at associated photoexcitation wavelengths.

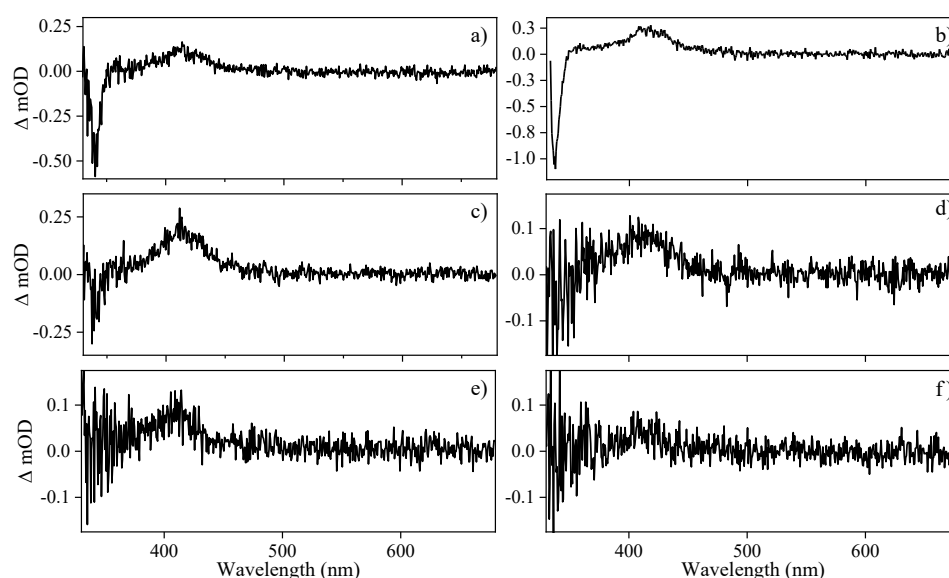


Figure 4.5 TAS taken at 2.5 ns pump probe delay of *p-E,E*-DPD in solvated in a) ethanol, excited at 318 nm and b) excited at 329 nm, c) acetonitrile, excited at 317 nm and d), excited at 327 nm and e) cyclohexane, excited at 315 nm and f) cyclohexane, excited at 329 nm.

4.4 Discussion

To quantitatively assign lifetimes to the reported TAS features, a global fit across all wavelengths (330 – 680 nm), using a sequential model ($A \xrightarrow{\tau_1} B \xrightarrow{\tau_2} C \xrightarrow{\tau_3} D$), was performed using the Glotaran software package.^{20,21} The associated residuals from the fitting model are displayed in Figure S4.1 of the supporting information in this chapter. The extracted lifetimes and evolutionary associated difference spectra (EADS) shown in Table 4.2 and Figure 4.6 respectively. Further detailed explanation of the fitting procedure is discussed in Section 2.4.

As described above, the dominant product was found to be *p*-*E,E*-DPD and is shown through NMR (Figure 4.2), which agrees favourably with the calculated structures predicting that the lowest conformation is the *E,E* isomer (Table 4.1). From the reported lifetimes given in Table 4.2 and associated EADS presented in Figure 4.6, we can now discuss the reported TAS (Figure 4.5), with reference to the schematic shown in Figure 4.7 depicting the dynamical processes in operation, and drawing on insight from comparative studies (with associated lifetimes, also shown in Table 4.2) of *E*-EHMC.⁴

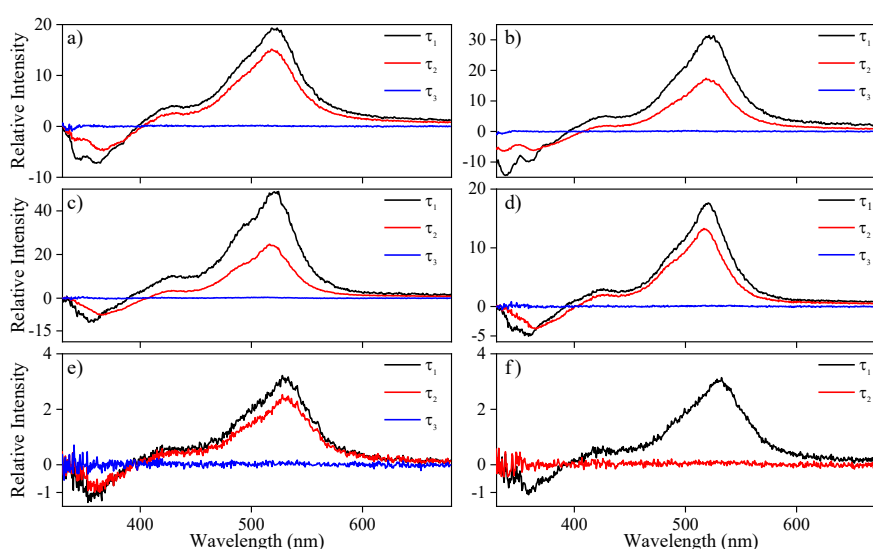


Figure 4.6 EADS for the TAS of *p*-*E,E*-DPD in ethanol: a) excited at 318 nm and b) excited at 329 nm, acetonitrile c) excited at 317 nm and d) excited at 327 nm and cyclohexane e) excited at 315 nm and f) excited at 329 nm.

Table 4.2 Lifetimes and associated errors (2σ) extracted from the global sequential fitting of *p*-*E,E*-DPD and previously reported values *E*-EHMC, in methanol and cyclohexane. Lifetimes for *E*-EHMC are also shown for comparison. ^a Taken from reference 4.

Solvent/ Excitation wavelength (nm)	τ_1 (fs)	τ_2 (ps)	τ_3 (ns)
<i>p</i> - <i>E,E</i> -DPD			
ethanol (318 nm)	400 ± 50	8.28 ± 0.05	$\gg 2.5$
ethanol (329 nm)	190 ± 50	7.82 ± 0.05	$\gg 2.5$
acetonitrile (317 nm)	90 ± 50	7.73 ± 0.05	$\gg 2.5$
acetonitrile (327 nm)	190 ± 50	8.70 ± 0.05	$\gg 2.5$
cyclohexane (315 nm)	480 ± 50	10.34 ± 0.15	$\gg 2.5$
cyclohexane (329 nm)	-	10.08 ± 0.10	$\gg 2.5$
<i>E</i> -EHMC ^a			
methanol (308 nm)	260 ± 90	1.10 ± 0.30	$\gg 2.0$
cyclohexane (290 nm)	600 ± 100	1.80 ± 1.20	$\gg 2.0$

Photoexcitation to the initially populated S_1 ($^1\pi\pi^*$) state, leads to population traversing out of the Franck-Condon region with a lifetime of τ_1 . Notably, τ_1 for acetonitrile is significantly shorter than that of either ethanol or cyclohexane, as has previously been reported for similar systems.^{3,22} Also worthy of note is the lack of a lifetime for cyclohexane photoexcited at 329 nm attributed to moving out of the Frank-Condon. This fs lifetime, τ_1 , may (likely) encompass any geometry rearrangement of solute and surrounding solvent. As with similar systems, this geometry rearrangement is not thought to involve a change in the electronic state, with the minimal differences between the first and second EADS.^{23,24} τ_2 then describes the evolution of excited state population, as it moves towards an S_1/S_0 CI along the $E \rightarrow Z$ isomerisation coordinate, and then funnels through this CI. This latter step leads to effective repopulation of the ground (S_0) state. This assignment is consistent with the previous report of cinnamates and in particular that of E -EHMC.^{4,25}

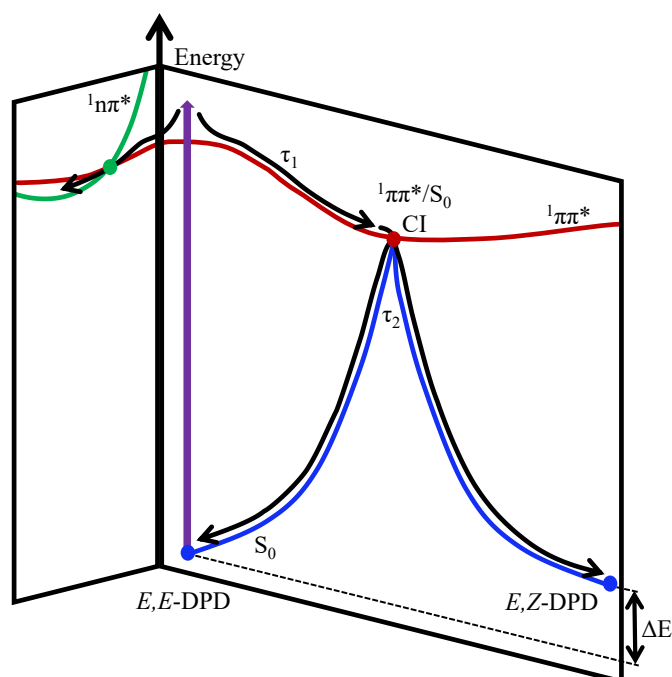


Figure 4.7 Schematic of relaxation for photoexcited p - E , E -DPD, showing the progression of τ_1 and τ_2 . We add that τ_3 (not shown) would correspond to population trapped in the p - E , Z -DPD and $^1n\pi^*$ state.

Previous reports on photoisomerisation have identified the presence of an ESA feature at long time delays,^{3,4,22,25–27} attributed to the formation of the corresponding geometric isomer; in the present case, this would correspond to p - E , Z -DPD (or p - Z , Z -DPD). This may be the case here, evidenced through the incomplete ground state bleach recovery of p - E , E -DPD (negative feature <350 nm; see Figure 4.5). However, the positive feature centred on 400 nm points towards a long-lived excited

state, which would also restrict ground state bleach recovery. We attribute this long-lived excited state to either an $^1n\pi^*$ or triplet state. We draw confidence that this is due to an ESA and not photoproduct formation, given that neither *p-E,Z*-DPD or *p-Z,Z*-DPD isomer is likely to absorb beyond 400 nm, based on the calculations and the steady-state irradiation spectra showing no feature growth over 2 hrs (Figure 4.3). Both the ESA and GSB features in the TAS, persist to $\Delta t = 2.5$ ns and are assigned a lifetime of τ_3 .

It is evident from steady-state irradiation measurements and the calculated transition oscillator strengths that the geometric isomer *p-E,Z*-DPD has a weaker absorbance < 350 nm than the *p-E,E*-DPD (*cf.* Figure 4.3, 0 and 7200 seconds irradiation). Given the TAS represents a difference spectrum (See Chapter 1 for more information), it is unsurprising that a negative feature is observed in the TAS. Further evidence, *via* ^1H NMR data (Figure 4.3), of isomerisation from *p-E,E*-DPD \rightarrow *p-E,Z*-DPD is given in the formation of several new hydrogen environments particularly those with 13 Hz splitting. However, there is no absorption of either isomer at wavelengths greater than 350 nm evident in the steady-state measurements, pointing to a different origin of the positive feature in the TAS >400 nm. This relatively small ESA is likely due to either a $^1n\pi^*$ or a triplet state. Several reports have suggested the presence of $^1n\pi^*$ states playing a role within relaxation of similar systems.^{28–30} The possibility of the absorption feature, being due to a radical cation species, generated *via* a step-wise two-photon ionisation, was considered (as seen for similar species),^{22,31,32} but dismissed due to the linear power dependence of the feature, as shown the power studies presented in Figure 4.8. Finally the absorption of a triplet state was also considered as the feature around 400 nm. However, this was also dismissed due to the overall

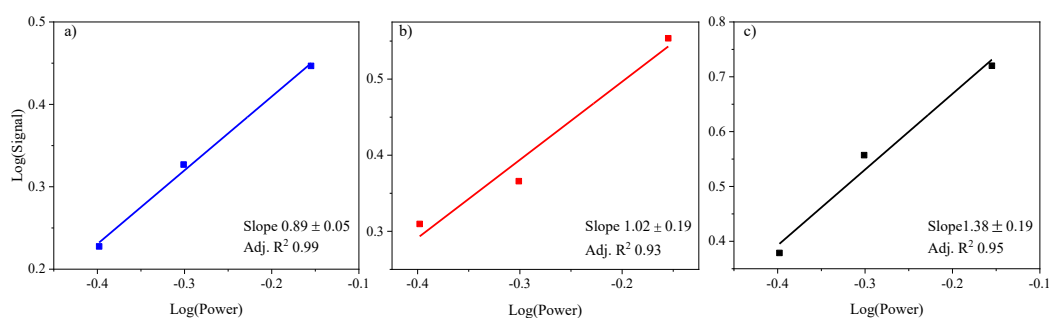


Figure 4.8 Power dependency for the integrated intensity for *p-E,E*-DPD using a 10 nm integration window, 405–415 nm, at $\Delta t = 2.5$ ns pump-probe delay. a) ethanol following excitation at 318 nm; b) acetonitrile following excitation at 317 nm; and c) cyclohexane following excitation at 315 nm.

spectral shape with triplet states providing a broad absorption across the probe region.^{33,34} Further experimentation implementing the use of triplet quenchers could be performed to resolve this assignment of this feature. Taken together, we assign τ_3 to a combination of a long-lived $^1n\pi^*$ state and presence of *p-E,Z*-DPD. To conclude the discussion of the long lived feature in the TAS, it is worth noting that a quantitative analysis of the conversion of *p-E,E*-DPD to *p-E,Z*-DPD is not possible from the TAS given the convoluted nature of the features both at early times (from the stimulated emission) and at $\Delta t = 2.5$ ns (from the presence of (potentially) the $^1n\pi^*$ state).

It is evident from the data thus far that *p-E,E*-DPD may possess suitable properties for applications as a UV filter. Notably, its absorption spectrum is similar to that of *E*-EHMC,^{2,4} but with a slight red-shift (~ 10 nm), meaning it extends further into the UVA which is a sought after quality for a UV filter. Coupled to this is the rapid relaxation of the excited state through an accessible CI, consistent with the previous literature of similar species.^{3,22,25} Furthermore, the apparent degradation upon constant UVR is attributed to interconversion to the *p-E,Z*-DPD isomer. This finding is, once again, in good agreement with previous reports on *E*-EHMC versus *Z*-EHMC.^{4,7} However, *Z*-EHMC is known to have a different response from DNA compared to *E*-EHMC,⁸ something which may also occur between *p-E,E*-DPD and *p-E,Z*-DPD but these studies are beyond the scope of the work presented here.

Whilst there are similarities to *E*-EHMC, there are evident differences. First, the apparent interconversion through the CI between the two isomers is longer for *p-E,E*-DPD in comparison with *E*-EHMC, e.g. in cyclohexane, $\tau_2 \sim 10$ ps for *p-E,E*-DPD versus ~ 2 ps for *E*-EHMC (see Table 4.2).⁴ This indicates that photoisomerisation is impinged by the different substituent in the *para* position. In this case, the addition of a second methyl acrylate alters the excited state dynamics by increasing the time for ground state repopulation, be it in *p-E,E*-DPD or *p-E,Z*-DPD. Whilst the underlying reason for this is not known, this inevitably points to alterations to the excited state landscape along the photoisomerisation coordinate. Added to this is that the increase in excited state lifetime could promote competing pathways; the ns component (τ_3) of the *E*-EHMC can entirely be attributed to occurrence of the *Z*-isomer whilst for *p-E,E*-DPD, this appears to be constructed of multiple components, the *p-E,Z*-DPD isomer and a long-lived $n\pi^*$ state. Additionally, compared to *E*-EHMC, the time taken to reach a photo-equilibrium is increased to 20

minutes (*cf.* 2 minutes for *E*-EHMC, using a standard solar spectrum as the irradiation source).⁷ Finally, of note is that no detectable spectroscopic evidence for *p*-*Z,Z*-DPD was observed in any experiments, leading to the hypothesis that a photo-equilibrium is only established between *p*-*E,E*-DPD and *p*-*E,Z*-DPD.

4.5 Conclusion

This study highlights the effect of chemical substitution on an established photoisomerisation pathway. In this instance, we compare *p*-*E,E*-DPD with the commercial UV filter *E*-EHMC. Following photoexcitation in solvents of varying polarity, the excited state population in *p*-*E,E*-DPD evolves out of the Franck-Condon region within 500 fs, along with geometry rearrangement of the solute and surrounding solvent, enabling access to an energetically accessible S_1/S_0 conical intersection. As the population transfers to the electronic ground state, the first difference between *p*-*E,E*-DPD and *E*-EHMC is in the relaxation times; ~ 10 ps for *p*-*E,E*-DPD and ~ 2 ps *E*-EHMC (both in cyclohexane). Ultimately this change is assigned to effects of the additional methyl acrylate on the excited state landscape. The second difference relates to the assignment of τ_3 ; here τ_3 describes the presence of the corresponding *p*-*E,Z*-DPD isomer, along with a small percentage of the excited state population trapped in an $^1n\pi^*$ state, which persists beyond the time-window of the present measurements ($> ns$). This ns component is absent in *E*-EHMC. Furthermore, no evidence for *p*-*Z,Z*-DPD was observed, leading to the conclusion that its formation is unfavoured and the photoequilibrium is generated between *p*-*E,E*-DPD, and *p*-*E,Z*-DPD. As a final comparison, the steady-state absorption spectra of *p*-*E,E*-DPD (in solvents of varying polarity) are red-shifted relative to the absorption spectra of *E*-EHMC, allowing for stronger absorption within the UVA region of the spectrum. This is a key quality, which is expected for new UV filters, given the growing need for photoprotection across the UVB and UVA regions of the solar spectrum.³⁵ Taken together, the results shown here provide insight into how modifications of the molecular structure can provide both positives, red-shifting the absorption spectra, and negatives, by increasing the excited state lifetime.

4.6 Supporting Information

4.6.1 Fitting Residuals

Extracted fitting residuals from TAS of *p*-*E,E*-DPD collected when fitting with a multi-step sequential model.

a) b)

c) d)

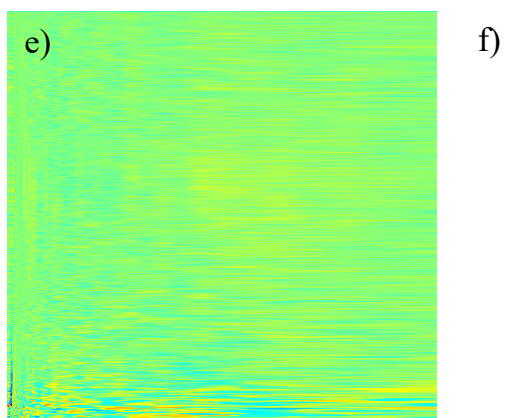


Figure S4.1 False colour heat maps of fitting residuals for *p*-*E,E*-DPD in ethanol: a) excited at 318 nm and b) excited at 329 nm, acetonitrile c) excited at 317 nm and d) excited at 327 nm and cyclohexane e) excited at 315 nm and f) excited at 329 nm.

4.6.2 Power Dependencies

Power dependency measurements of *p-E,E*-DPD show a linear dependence across the spectral features of the TAS. These measurements were achieved by varying the pump power and taking a 10 nm integration window across a particular spectral window at a given pump-probe time delay. Each TAS displays a linear relationship to the incident pump power (log(signal) vs. log(power) plots), strongly suggesting single photon induced dynamics.

a)

b)

c)

d)

e)

f)

Figure S4.2 Power dependencies for the integrated signal intensity for *p-E,E*-DPD for a 10 nm integration window, 515-525 nm, at $\Delta t = 1$ ps pump-probe delay; a) ethanol following excitation at 318 nm and b) ethanol following excitation at 329 nm c) acetonitrile following excitation at 317 nm and d) acetonitrile following excitation at 327 nm e) cyclohexane following excitation at 315 nm and f) cyclohexane following excitation at 329 nm.

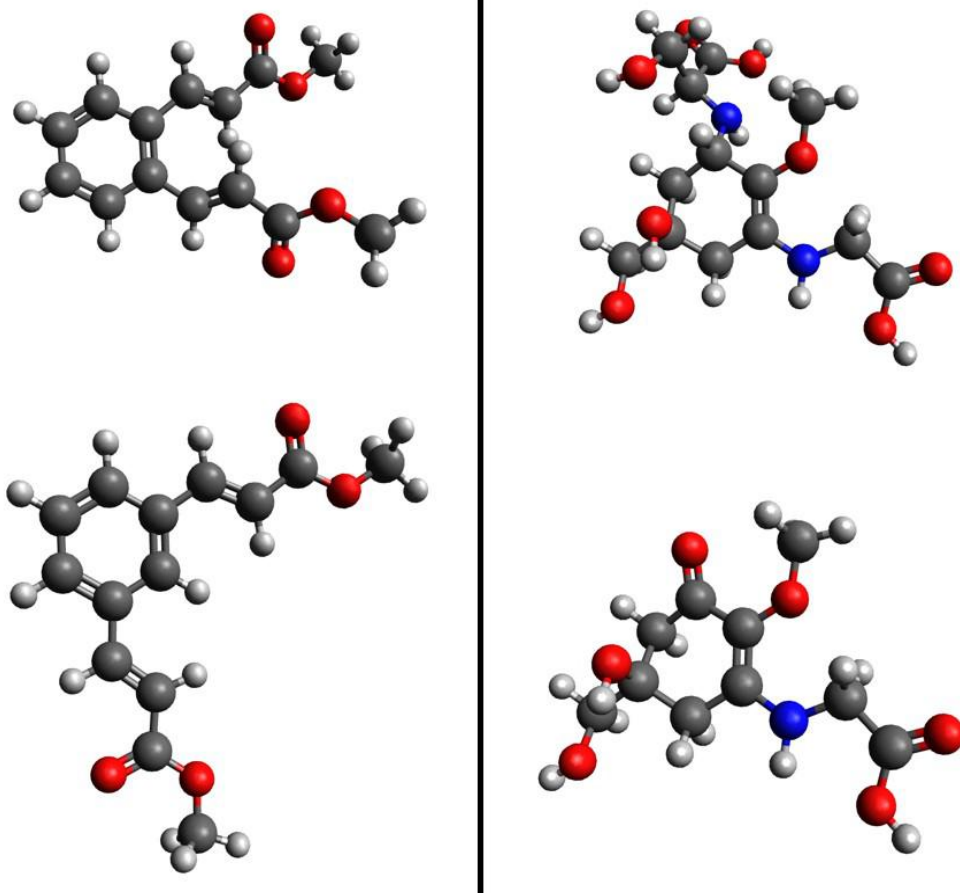
4.7 Bibliography

- 1 N. A. Shaath, *Photochem. Photobiol. Sci.*, 2010, **9**, 464–469.
- 2 U. Osterwalder and B. Herzog, *Photochem. Photobiol. Sci.*, 2010, **9**, 470–481.
- 3 L. A. Baker, M. D. Horbury, S. E. Greenough, F. Allais, P. S. Walsh, S. Habershon and V. G. Stavros, *J. Phys. Chem. Lett.*, 2016, **7**, 56–61.
- 4 Y. Peperstraete, M. Staniforth, L. A. Baker, N. D. N. Rodrigues, N. C. Cole-Filipiak, W.-D. Quan and V. G. Stavros, *Phys. Chem. Chem. Phys.*, 2016, **18**, 28140–28149.
- 5 T. M. Karpkird, S. Wanichweacharungruang and B. Albinsson, *Photochem. Photobiol. Sci.*, 2009, **8**, 1455–1460.
- 6 S. Pattanaargson, T. Munhapol, P. Hirunsupachot and P. Luangthongaram, *J. Photochem. Photobiol. A Chem.*, 2004, **161**, 269–274.
- 7 K. M. Hanson, S. Narayanan, V. M. Nichols and C. J. Bardeen, *Photochem. Photobiol. Sci.*, 2015, **14**, 1607–1616.
- 8 A. Sharma, K. Bányiová, P. Babica, N. El Yamani, A. R. Collins and P. Čupr, *Sci. Total Environ.*, 2017, **593–594**, 18–26.
- 9 N. Blüthgen, S. Zucchi and K. Fent, *Toxicol. Appl. Pharmacol.*, 2012, **263**, 184–194.
- 10 M. Coronado, H. De Haro, X. Deng, M. A. Rempel, R. Lavado and D. Schlenk, *Aquat. Toxicol.*, 2008, **90**, 182–187.
- 11 M. Ghazipura, R. McGowan, A. Arslan and T. Hossain, *Reprod. Toxicol.*, 2017, **73**, 175–183.
- 12 H. Miura, S. Takahashi, H. Kasai, S. Okada, K. Yase, H. Oikawa and H. Nakanishi, *Cryst. Growth Des.*, 2010, **10**, 510–517.
- 13 W. Humphrey, A. Dalke and K. Schulten, *J. Mol. Graph.*, 1996, **14**, 33–38.
- 14 T. H. Dunning, *J. Chem. Phys.*, 1989, **90**, 1007–1023.
- 15 C. Adamo and V. Barone, *J. Chem. Phys.*, 1999, **110**, 6158–6170.
- 16 M. Valiev, E. J. Bylaska, N. Govind, K. Kowalski, T. P. Straatsma, H. J. J.

- Van Dam, D. Wang, J. Nieplocha, E. Apra, T. L. Windus and W. A. De Jong, *Comput. Phys. Commun.*, 2010, **181**, 1477–1489.
- 17 A. Klamt and G. Schüürmann, *J. Chem. Soc. Perkin Trans. 2*, 1993, **0**, 799–805.
- 18 D. M. York and M. Karplus, *J. Phys. Chem. A*, 1999, **103**, 11060–11079.
- 19 P. Winget, D. M. Dolney, D. J. Giesen, C. J. Cramer and D. G. Truhlar, Minnesota solvent descriptor database, <http://comp.chem.umn.edu/solvation/mnsddb.pdf>.
- 20 J. J. Snellenburg, S. P. Laptенок, R. Seger, K. M. Mullen and I. H. M. van Stokkum, *J. Stat. Softw.*, 2012, **49**, 1–22.
- 21 K. M. Mullen and I. H. M. van Stokkum, *J. Stat. Softw.*, 2007, **18**, 1–46.
- 22 M. D. Horbury, L. A. Baker, W.-D. Quan, S. E. Greenough and V. G. Stavros, *Phys. Chem. Chem. Phys.*, 2016, **18**, 17691–17697.
- 23 A. Espagne, D. H. Paik, P. Changenet-Barret, M. M. Martin and A. H. Zewail, *ChemPhysChem*, 2006, **7**, 1717–1726.
- 24 H. Kuramochi, S. Takeuchi and T. Tahara, *J. Phys. Chem. Lett.*, 2012, **3**, 2025–2029.
- 25 M. D. Horbury, L. A. Baker, N. D. N. Rodrigues, W.-D. Quan and V. G. Stavros, *Chem. Phys. Lett.*, 2017, **673**, 62–67.
- 26 M. D. Horbury, W.-D. Quan, A. L. Flourat, F. Allais and V. G. Stavros, *Phys. Chem. Chem. Phys.*, 2017, **19**, 21127–21131.
- 27 M. D. Horbury, A. L. Flourat, S. E. Greenough, F. Allais and V. G. Stavros, *Chem. Commun.*, 2018, **54**, 936–939.
- 28 X. P. Chang, C. X. Li, B. Bin Xie and G. Cui, *J. Phys. Chem. A*, 2015, **119**, 11488–11497.
- 29 S. Kinoshita, Y. Miyazaki, M. Sumida, Y. Onitsuka, H. Kohguchi, Y. Inokuchi, N. Akai, T. Shiraogawa, M. Ehara, K. Yamazaki, Y. Harabuchi, S. Maeda, T. Taketsugu and T. Ebata, *Phys. Chem. Chem. Phys.*, 2018, **20**, 17583–17598.

- 30 N. D. N. Rodrigues, M. Staniforth, J. D. Young, Y. Peperstraete, N. C. Cole-Filipiak, J. R. Gord, P. S. Walsh, D. M. Hewett, T. S. Zwier and V. G. Stavros, *Faraday Discuss.*, 2016, **194**, 709–729.
- 31 S. Foley, S. Navaratnam, D. J. McGarvey, E. J. Land, T. G. Truscott and C. A. Rice-Evans, *Free Radic. Biol. Med.*, 1999, **26**, 1202–1208.
- 32 M. Vengris, D. S. Larsen, M. A. van der Horst, O. F. A. Larsen, K. J. Hellingwerf and R. van Grondelle, *J Phys Chem B Condens Matter Mater Surf Interfaces Biophys*, 2005, **109**, 4197–4208.
- 33 D. V. Bent and E. Hayon, *J. Am. Chem. Soc.*, 1975, **97**, 2599–2606.
- 34 M. D. Horbury, L. A. Baker, W. D. Quan, J. D. Young, M. Staniforth, S. E. Greenough and V. G. Stavros, *J. Phys. Chem. A*, 2015, **119**, 11989–11996.
- 35 R. P. Sinha and D.-P. Häder, *Photochem. Photobiol. Sci.*, 2002, **1**, 225–236.

5 Expanding on the Bottom-up and Functionalisation Approaches



Biosynthesis and extraction of the MAAs was performed by Ms Nazia Auckloo, School of Life Sciences, University of Warwick.

Synthesis of *ortho* and *meta* *E,E*-DPD was performed by Ms Michelle Chan and Dr Guy J. Clarkson, Department of Chemistry, University of Warwick.

Calculations displayed in Table 5.2 were performed by Ms Sofia Goia and Mr Matthew A.P. Turner, Department of Chemistry, University of Warwick.

In the previous two Chapters, the photochemistry of two different classes of photoprotective molecules has been explored. This Chapter contains unpublished work with a brief preliminary discussion, owing to time constraints, that seeks to further explore the results and conclusions of both Chapter 3 and 4. In Chapter 3 we showed the dynamics of two mycosporine-like amino acids (MAA) motifs; this work will now be extended to the actual MAAs themselves in an effort to elucidate the dynamics of natural MAA systems. Likewise in Chapter 4 we observed how a photoisomerisation pathway was affected through symmetric functionalisation of an acrylate moiety on the phenyl ring. We will now discuss the effects of substitution on the photoisomerisation pathway,¹⁻⁴ at both the *ortho* and *meta* positions relative to the first acrylate moiety.

5.1 The Photodynamics of Bacterial Sunscreens

The results from Chapter 3 showed how the two different core motifs of MAAs behave following photoexcitation. The results are consistent with the previous theoretical work of Losantos *et al.*⁵ that show how the cyclohexenone based motifs are prevented from relaxing back to the ground electronic state with the conical intersection (CI) energetically higher in energy than the minimum of the excited electronic state (see Section 1.3.2 for more details). For the systems based on the cycloheximine motifs, the experimental results displayed in Chapter 3 again agree with computational work by Losantos *et al.* which shows that there is no barrier *en route* to the CI between the excited electronic and the ground electronic state.⁵ While the experimental results in Chapter 3 agree with the recent theoretical work, questions still exist pertaining to the ability of MAAs to provide photoprotection, especially for those which are formed with a cyclohexenone core such as 4-deoxygadusol and mycosporine-glycine that both show high levels of photostability.⁶⁻⁸ In an effort to further identify the relaxation mechanisms for MAAs, transient electronic absorption spectroscopy (TEAS) has been performed on two different sample mixtures: one containing the MAAs, shinorine, mycosporine-glycine and 4-deoxygadusol (termed Sample 1 henceforth) and the second containing porphyra-334, and a geometric isomer pair, usujirene and palythene (termed Sample 2). These samples provide a broad absorption across the UVB and UVA regions as shown in Figure 5.1 along with the structures of the MAAs in each sample mixture.

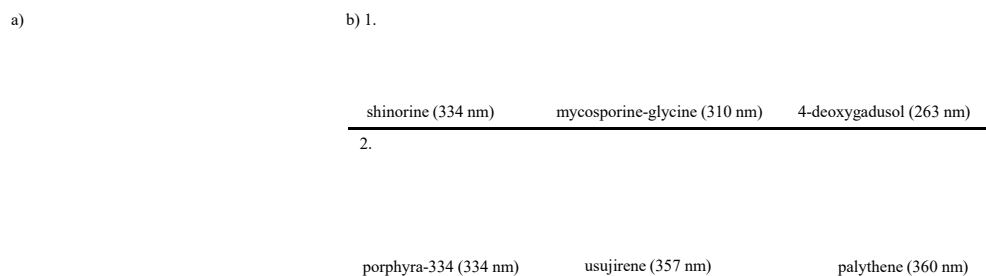


Figure 5.1 a) UV/Vis spectra of both MAA samples. Sample 1 in water (black line), and Sample 2 in methanol (red line). Vertical lines show the photoexcitation wavelengths used for each sample.

b) Structures of MAAs present in each Sample 1 and Sample 2 with their reported absorption maximum (in brackets) to aid discussion.

5.1.1 Experimental Methodology

5.1.1.1 Biosynthesis and Extraction

Biosynthesis of 4-deoxygadusol, mycosporine-glycine and shinorine along with the extraction of usujirene, palythene and porphyra-334 was performed by Ms Nazia Auckloo (School of Life Sciences, University of Warwick) following the protocol detailed below:

A mixture comprised of 3 μl of plasmid DNA containing the gene constructs pET 29b-Ava 3858-3855 and competent cells (*E. coli* Bap1) was prepared under sterile conditions where 100 μl of the mixture was transferred into an electroporation cuvette. The cuvette was tapped three times to avoid air bubbles affecting the electric flow. A 2 kV voltage was applied (25 μF and resistance capacity: 200 Ω) and 1 ml Luria Bertani (LB) was quickly added after electroporation to prevent the cells from dying. The cuvette was incubated at 37°C for 1 hr on a shaker. Different volumes (100 μl , 200 μl and 400 μl) of the reaction mixture was spread on selective agar plates (LB Agar containing kanamycin plates) and the latter were incubated at 37°C overnight. A single colony was selected the following day and allowed to grow in 10 ml LB containing kanamycin.

A culture of 10 ml LB broth and kanamycin was inoculated with the genes constructs which was subsequently allowed to grow overnight at 37°C on the shaker. On the following day, 5 ml of the respective overnight culture was transferred to 500 ml fresh LB broth supplemented with 50 $\mu\text{g}/\text{mL}$ kanamycin and allowed to grow at 37°C on the shaker until reaching an optical density at 600 nm (OD_{600}) of about 0.6. This process was carried out twice (simultaneously) leading to a total culture of 1 L. 500 μl of 1 M isopropyl β -D-1-thiogalactopyranoside (IPTG) was then added to the culture

medium after the latter had an OD₆₀₀ of 0.6 and the flasks were left overnight at 20°C on the shaker. The next day, the induced culture with IPTG was centrifuged at 4000 rpm for 30 minutes. The supernatant was discarded and the pelleted cells were resuspended in 20 ml methanol. The resuspended cells were then sonicated for 3 sets of 1 minute pulses with 1 minute recovery in between on ice. The solution was centrifuged at 4000 rpm for 30 minutes. Following centrifugation, the residue (pelleted cells) was discarded and the supernatant was dried.

For the extraction of usujirene, palythene and porphyra-334, (Sample 1) *Palmaria palmata* was macerated in 25 % methanol at 4 °C overnight after which it was centrifuged and the supernatant evaporated. This produced a crude extract. From this crude extract, reverse-phase column chromatography followed by HPLC was performed to further purify the MAAs.

5.1.1.2 Experimental Details

A full description of the transient absorption setup is given in Section 2.3. For the measurements discussed below, only the key details are provided. Samples were prepared in water for Sample 1 and in methanol for Sample 2, the samples were then placed in a 1 mm quartz cuvette. The cuvette was translated in the plane of the sample interaction (perpendicular to laser beam travel) to ensure a fresh sample is interrogated for each pump-probe pulse pair. Degradation of the sample was monitored by comparing the signal intensities before and after each scan. Photoexcitation wavelengths were chosen for Sample 1 at distinct spectral regions in the absorption spectrum, centred on 300 and 328 nm. For Sample 2 the excitation was chosen to correspond to the reported absorption maximum of usujirene, 357 nm.^{9,10} Steady-state UV/Vis measurements were performed on a Cary-60 spectrometer using a 1 cm quartz cuvette.

5.1.2 Results

5.1.2.1 Transient Electronic Absorption Spectroscopy Measurements

TEAS was performed on Sample 1 using two photoexcitation wavelengths, 300 nm and 328 nm, and at 357 nm for Sample 2. The resulting data is displayed as false colour heat maps shown in Figure 5.2. As shown in Figure 5.2 the TAS of both Sample 1 and Sample 2 exhibit largely the same dynamics. For Sample 1 following photoexcitation at both wavelengths there is a ground state bleach (GSB) along with an excited state

absorption (ESA), located at the blue edge of the probe region. However, there are differences between the TAS at different excitations; for photoexcitation at 328 nm (Figure 5.2b) there is a broad stimulated emission (SE) evident across the probe region at early pump-probe time delay which is absent following photoexcitation at 300 nm (Figure 5.1a). All of the described features recover to baseline within 10 ps of the photoexcitation.

a) b) c)

Figure 5.2 False colour heat maps for Sample 1 in water photoexcited at a) 328 nm and b) 300 nm. c) False colour heat map of Sample 2 in methanol photoexcited at 357 nm. The pump-probe time delay is plotted linearly from -0.5 ps to 1 ps and then logarithmically out to 3 ns.

Following photoexcitation of Sample 2 (Figure 5.2c) again there is a broad SE across the probe region (400-570 nm) at early pump-probe time delay along with an ESA and GSB feature around 400 nm. Additionally, for Sample 2 there is a faint ESA at the red edge (long wavelengths) of the probe region which still persists to the maximum pump-probe time delay. Also evident is the presence of a GSB and ESA feature, < 400 nm, which is visible to the maximum pump-probe time delay of 3 ns.

5.1.3 Discussion

From the spectra shown in Figure 5.1, we can see that there is a broad absorption across the UVA/B spectral regions. For Sample 1, this is consistent with the presence of the three MAAs synthesised, with the two main peaks centred at 263 and 328 nm providing good agreement with the reported maxima of 4-deoxygadusol and shinorine.¹¹ The third MAA, mycosporine-glycine, has a reported absorption maximum at 310 nm,⁸ and its presence can account for the plateau in the spectrum between 300 and 285 nm (Figure 5.1 black trace). This separation in the absorption maxima and the overall spectral shape of each MAA individually, with one main absorption feature across the UVA/B region, allows us to assume that the narrowband photoexcitation employed in the transient absorption studies, (typically a full width

half maximum of 4 nm) excites primarily only one distinct MAA species within the sample mixture.

In Sample 2, once again, there is a mixture of three MAAs: porphyrin-334, usujirene and palythene. As implied from Figure 5.1 (red trace), these three MAAs provide a strong absorbance across the UVA with the reported absorption maximum at 334 nm, 357 nm and 360 nm for porphyrin-334, usujirene and palythene, respectively.^{10,12} From the spectrum shown in Figure 5.1, it is evident that usujirene and palythene are present as well as a small shoulder attributed to the presence of porphyrin-344. Unlike Sample 1, the differentiation of absorption maxima between MAAs in this sample is smaller, particularly for usujirene and palythene (357 to 360 nm absorption maxima) which are geometric isomers. As such the photoexcitation at 357 nm will inevitably excite both usujirene and palythene.

A quantitative analysis of all the TAS was performed through the use of a global fitting method, using a sequential model ($A \xrightarrow{\tau_1} B \xrightarrow{\tau_2} C \xrightarrow{\tau_3} D$). The lifetimes extracted from photoexcitation of Sample 1 and Sample 2, including the photoexcitation wavelength used, are shown in Table 5.1, along with the extracted errors. The evolutionary associated difference spectra (EADS) of Sample 1 are displayed in Figure 5.3. The quality of the fits was examined through the residuals which are displayed in

Table 5.1 Lifetimes and associated errors (2σ) from the global sequential fitting of Samples 1 and 2.

Excitation Wavelength	τ_1	τ_2	τ_3
Sample 1			
300 nm	2.00 ps \pm 90 fs	-	-
328 nm	140 \pm 50 fs	1.74 ps \pm 60 fs	-
Sample 2			
357 nm	240 \pm 50 fs	930 \pm 50 fs	1.896 ns \pm 70 ps

a)

b)

Figure 5.3 EADS of Sample 1 photoexcited at a) 328 nm and b) 300 nm.

Figure S5.1 in the supporting information. Further information on the fitting procedure is given in Section 2.4.

Photoexcitation of Sample 1 at 328 nm preferentially excites the MAA shinorine. The first EADS (Figure 5.3a) decays with a lifetime of $\tau_1 = 140$ fs, which displays a GSB (< 360 nm) and SE (360-500 nm). The sharp negative feature at 370 nm is attributed to an artefact of the instrument response. The decay of this stimulated emission feature is assigned to population transfer across the excited state potential energy surface towards and through, an energetically accessible CI. The assignment of these features is consistent with the data obtained in the model MAA system termed NN (see Chapter 3 for more details).¹³ Furthermore, the extracted lifetime ($\tau_1 = 140 \pm 50$ fs) compares well with calculated excited state lifetimes for similar systems.⁵ As discussed in Chapter 3, one would expect this SE to red-shift as the excited state population evolves across the potential energy surface *en-route* to the CI. This red-shift is indeed evidenced here again in the SE feature (and again in Figure 5.2c). However, we have been unable to extract any dynamical due to limitations of the fitting procedure regarding the treatment of spectrally shifting signals. Once through the CI, the excited state population reaches a vibrationally hot electronic ground state, which subsequently undergoes intramolecular vibrational redistribution (IVR) and intermolecular energy transfer (IET) to the solvent. These processes are sensibly consistent with the observed spectral features of the second EADS: an ESA which spectrally blue-shifts as pump-probe time delay increases, offset from the GSB. These features recover back to the baseline with a lifetime of $\tau_2 = 1.74$ ps. This assignment is again consistent with the result of Chapter 3.

For the photoexcitation of Sample 1 at 300 nm (which approximately corresponds to the absorption maximum for mycosporine-glycine) there is an absence of the stimulated emission feature observed at the other excitation wavelength (328 nm Figure 5.2 panel a, compared to panel b). The TAS is fitted with one lifetime and corresponding EADS comprising of a GSB feature (< 350 nm) and ESA (> 350 nm). These features are attributed to the cooling of a vibrational hot ground electronic state. Unlike previous reports both here (*vide supra*) and in Chapter 3. The TEAS data does not show spectral features that can be assigned to the initially prepared excited electronic state. We postulate two reasons for this: first the observable signals from the excited electronic state, either absorption or emission, falls out of the probe region

(320-720 nm). Secondly and more likely, the response from the excited electronic state occurs on a timescale that is much faster than our instrument response allows us to (< 100 fs). The weak signal-to-noise of the data adds to the difficulty in trying to extract spectral features that might be assigned to those of the excited electronic state.

Figure 5.4 EADS of Sample 2 photoexcited at 357 nm. τ_3 (blue trace) is scaled by a factor of 3 to aid visualisation.

The TAS of Sample 2 following photoexcitation at 357 nm, was fitted with three lifetimes given in Table 5.1 and the corresponding EADS are displayed in Figure 5.4. We note here that this excitation wavelength, and the small separation of the absorption spectrum between usujirene and palythene will inevitably lead to excitation of both of these two MAAs. In the first EADS, two features are present, the GSB below 390 nm as well as the SE across the probe window (400-650 nm). Consistent with the discussion of Sample 1 above, and that of the results in Chapter 3, the decay of the SE feature is assigned to population traversing the excited state potential energy surface *en-route* to an energetically accessible CI.¹³ As the population travels along this potential energy surface towards the CI, there is an observed red-shift in the SE signal as pump-probe time delay increases. Again, due to the fitting procedure, used no extra quantitative information can be gleaned from the shifting of this feature. Once the population has traversed through the CI onto the ground electronic state, the population is now in a vibrationally hot ground electronic state. This population will vibrationally cool with a lifetime of τ_2 . Unlike the previous results from Sample 1, here there is a clear long-lived excited state absorption (broad ESA in τ_3 from 550-720 nm); this ESA decays with a lifetime of τ_3 . The EADS associated with τ_3 also show a photoproduct comprising of a GSB and ESA centred at 390 nm, which are likely attributed to the formation of the palythene (i.e. the *trans* isomer of usujirene). The assignment of this feature as the presence of the palythene is aided through the red-shift in absorbance of the *trans* isomer compared to the initial isomer usujirene.¹⁰ This shift leads to an enhancement of the absorption at the red edge of the UV/Vis

spectrum (390 nm), and a depletion of the initial absorbance (380 nm). As the TAS is a differential measurement this is observed as a bleach and a absorption feature spectrally offset to red wavelengths, similar photoproduct features have been observed before with other photoisomerisations.³ We add here that power dependency measurements were performed on both the ESA and photoproduct features in τ_3 (Figure S5.3). The signal attributed to the *trans* isomer formation displays a single photon dependence with pump beam power, while the second broad ESA displays a multiphoton dependence with pump beam power as such the broad ESA feature described by τ_3 may be attributed to a solvated electron given its spectral location.^{14,15}

As discussed in Section 2.4, we have assumed a sequential fitting model for all of the observed dynamics. However, for Sample 2, the relaxation from the initial electronic excited state produces two separate observable dynamical pathways. Firstly the SE and ESA attributed to the internal conversion through a CI followed by the photoproduct formation of the geometric isomer palythene, and secondly the solvated electron feature. The spectral features assigned to both of these processes are observed in parallel with one another. As a consequence of the sequential model used, the EADS associated with τ_3 displays the two different features with the same lifetime ($\tau_3 \approx 1.90$ ns). This lifetime however is attributed decay to the solvated electron feature,¹⁶ as the formation of the ground electronic of either isomer is significantly faster than the lifetime of τ_3 ($\tau_2 = 960$ fs). Additionally, both geometric isomers are known to be photostable at much longer timescales (hours),¹⁰ as such the signals attributed the formation of the isomer can be considered stationary for the lifetime of τ_3 . Figure 5.5 shows TAS at specific Δt illustrating the stability of the photoproduct attributed to palythene and the decay of the ESA attributed to the solvated electron.

Wavelength (nm)

Figure 5.5 Select TAS of Sample 2 following photoexcitation at 357 nm, showing the decay of the solvated electron feature and the stability of the ESA attributed to the geometric isomer palythene.

5.1.4 Conclusions for Bacterial Sunscreens

The photodynamics of three MAAs have been explored with all three exhibiting a ultrafast decay (< 500 fs) from the photoexcited electronic state back to the ground electronic ground state through an accessible CI. The observed ultrafast relaxation can be used to aid the explanation of the observed high photostability of several MAA studied previously.^{10,12,17,18} These results agree with previous computational reports alongside photoacoustic calorimetry showing a high conversion of the absorbed energy to the solvent in the form of heat.^{12,18} Transient absorption studies performed on shinorine and mycosporine-glycine showed no evidence of photoproduct formation, while the long-lived component from Sample 2 was attributed to the formation of the geometric isomer palythene and a solvated electron feature. Similar studies were also attempted on the third MAA present in Sample 1, 4-deoxygadusol, however no dynamics were observed across the probe region. While the work presented above is preliminary and the discussion limited, there are avenues which will be explored to aid further discussion of this work. Future work will endeavour to globally fit the TAS from Sample 2 using a branched model to accurately describe the dynamics of both the solvated electron and the formation of the *trans* isomer, palythene. Furthermore, Ms Abigail Whittock (Department of Chemistry, University of Warwick) in collaboration Ms Nazia Auckloo (School of Life Sciences, University of Warwick) are working to improve the biosynthesis allowing for individual MAAs to be isolated and studied.

Returning to the role of MAAs as both natural and cosmetic UV filters, the observed dynamics of a rapid relaxation from the excited electronic state, along with the broad-spectrum coverage across the UVA/B spectral region provide suitable characteristics for the use as commercial UV filters. Additionally, the formation of photoproducts is minimal and does not pose a problem. The reason for this is two-fold: (1) a component of the photoproduct is comprised of the geometric isomer palythene, which is also a MAA and highly photostable. (2) The solvated electron ‘photoproduct’ is an artefact of the fs pump photon power, and highly unlikely to occur at solar irradiance.

5.2 Effects of Positional Substitution on Photoisomerisation

In Chapter 4, we discussed how the symmetric substitution of methyl cinnamate increased the excited state lifetime *en-route* to the accessible CI along the photoisomerisation coordinate. In this section we have taken this one step further and varied the positions of the substitution, in an effort to explore how both *ortho* and *meta* substitutions alters the relaxation dynamics of methyl cinnamate following photoexcitation. Figure 5.6 shows the structures and steady-state UV/Vis spectra in ethanol of both the *ortho* species, dimethyl 3,3'-(1,2-phenylene)(2*E*,2'*E*)-diacrylate, abbreviated to *o-E,E*-DPD (Figure 5.6bi) and *meta* species, dimethyl 3,3'-(1,3-phenylene)(2*E*,2'*E*)-diacrylate, abbreviated to *m-E,E*-DPD (Figure 5.6bii.) along with the structure and UV/Vis of the *para* species *p-E,E*-DPD (Figure 5.6biii; see Chapter 4 for details) for comparison.

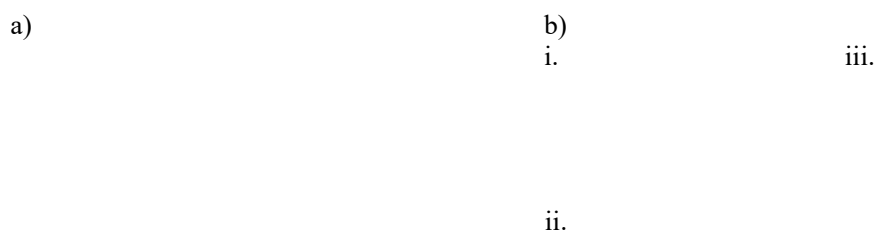


Figure 5.6 a) Steady-state UV/Vis spectra of *o-E,E*-DPD (black line), *m-E,E*-DPD (red line) and *p-E,E*-DPD shown in blue, all at 10 μ M concentration. b) Structures of the *ortho* (i), *meta* (ii) and *para* (iii) species.

5.2.1 Experimental Methodology

5.2.1.1 Synthesis and Characterisation

Synthesis of both *o-E,E*-DPD and *m-E,E*-DPD was performed by Dr Guy J. Clarkson and Ms Michelle Chan (Department of Chemistry, University of Warwick) in the following manner. For the *o-E,E*-DPD species, triphenylphosphine (53 mg / 0.2 mmol), 1,2-diiodobenzene (330 mg / 1 mmol), methyl acrylate (390 mg / 0.41ml / 4.53 mmol) and triethylamine (8 ml / excess) were all added to a 100 ml Schlenk tube. Nitrogen gas was bubbled through the mixture for 5 minutes then palladium acetate (23 mg / 0.1 mmol) was added and nitrogen bubbling continued for a further minute

before the Schlenk was sealed and the mixture heated and stirred at 100°C for 48 hours. The reaction mixture was poured onto a mixture of 2N hydrochloric acid (about 50 ml) containing some ice. The mixture was extracted with dichloromethane. These mixtures were extracted once with 2N hydrochloric acid and the dichloromethane layer dried with magnesium sulphate, filtered and the solvent removed at reduced pressure to give a brown oil. The oil was titrated with diethyl ether and the solvent decanted from a brown powder which was discarded. The diethyl ether was removed at reduced pressure and the mixture placed on a column of silica. Column chromatography was conducted with a solvent gradient of petrol to petrol: dichloromethane (1:1). The appropriate fractions were evaporated to dryness and the solid recrystallized from diethyl ether/petrol in the fridge to give the product.

Synthesis of the *m-E,E*-DPD species proceeded through the esterification of 1,3-phenylene-3,3'-bis(2-propenoic acid) with methanol. Concentrated sulphuric acid (1 ml) was added. The mixture is then allowed to reach room temperature and stand overnight. The precipitate was isolated by vacuum filtration and recrystallized from a saturated solution of methanol as plates. For both the *o-E,E*-DPD and *m-E,E*-DPD products, ¹H NMRs are shown in Figure 5.7.

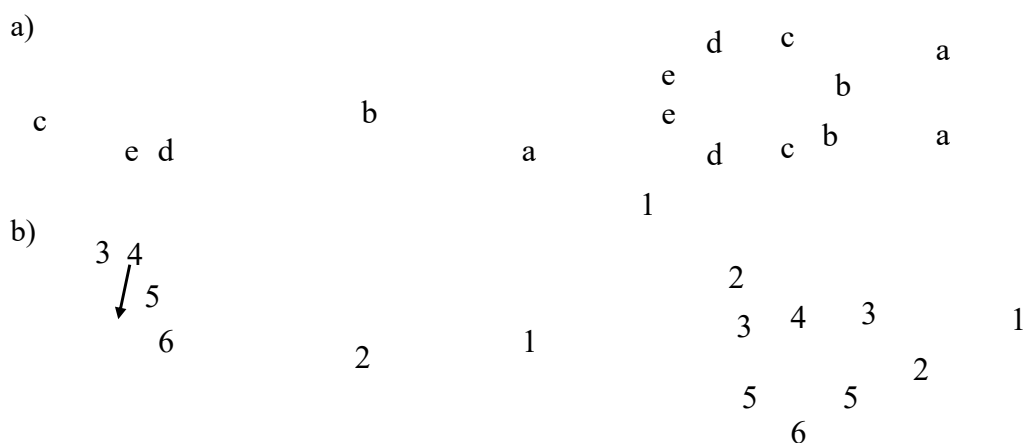


Figure 5.7 ¹H NMR of the synthesised products a) *o-E,E*-DPD b) *m-E,E*-DPD.

5.2.1.2 Experimental Details

Experimental details for the transient absorption setup are described in Section 2.3; details relating specifically to these measurements are given below. The photoexcitation wavelength was chosen to be the absorption maximum in the UVA/B region for each sample, which corresponded to 294 nm for *o-E,E*-DPD and 272 nm

for *m-E,E*-DPD. Each sample was prepared in 1 mM concentration in ethanol and flowed through the Harrick cell with a path length of 100 μm .

Steady-state irradiation was performed at 10 μM concentration using a Xenon arc lamp with a 5 nm bandwidth centred on the same excitation wavelengths as the TEAS measurements with a power of 400 μW . Irradiated ^1H NMR samples were dissolved in ethanol at approximately 10 mM concentration and irradiated at the specified wavelengths for 16 hrs with the same irradiation conditions as described above. Samples were dried with nitrogen gas and then dissolved in deuterated chloroform for ^1H NMR analysis. Steady-state UV/Vis and associated measurements were performed on a Cary 60 using a 1 cm quartz cuvette.

5.2.1.3 Calculations

The calculations reported here for both *o-E,E*-DPD and *m-E,E*-DPD were performed by Ms Sofia Goia and Mr Matthew A.P. Turner (Department of Chemistry, University of Warwick). Structures of DPD were generated for all three isomers in each structure (*E,E*, *E,Z*, *Z,Z*), using Visual Molecular Dynamics,¹⁹ with the molefactory plugin. Each structure underwent a geometry optimization within density functional theory using a cc-pVTZ basis set and PBE functional,^{20,21} using the NWChem software.²² A conductor-like screening model (COSMO) was used to replicate the effect of the solvent.^{23,24} The default COSMO implicit solvent model for ethanol within NWChem was used, the descriptors of which are based on the Minnesota Solvent Descriptor Database.²⁵

5.2.2 Results

5.2.2.1 Transient Electronic Absorption Spectroscopy Measurements

Collected TAS of both *o-E,E*-DPD and *m-E,E*-DPD, following photoexcitation at 294 and 272 nm, respectively, are displayed as false colour heat maps in Figure 5.8. Both heat maps display two ESA features centred on 350 and 450 nm along with an additional ESA at the red edge of the probe spectrum around 720 nm in the *meta* species and peaking out of the probe region in the *o-E,E*-DPD species. The first two features centred on 350 and 450 nm spectrally narrow as they evolve over pump-probe time delay.

a) b)

Figure 5.8 False colour heat maps for the TAS of a) *o*-*E,E*-DPD in ethanol and excited at 294 nm b) *m*-*E,E*-DPD in ethanol and excited at 272 nm. The pump-probe time delay is plotted linearly up to 1 ps and then logarithmically to the maximum time delay (3 ns).

5.2.2.1 Calculations

Ground state geometry optimisations of all three isomers in both the *ortho* and *meta* geometries were optimised at the cc-pVTZ /PBE level of theory. Table 5.2 shows the energy difference between each of the three potential isomers relative to the *E,E* form which was found to be the global minimum energy for each species (i.e. *o*-*E,E*-DPD and *m*-*E,E*-DPD).

Table 5.2 Calculated energy differences between the three isomers relative to the lowest energy isomer *E,E*.

Species	Isomer	<i>E,E</i>	<i>E,Z</i>	<i>Z,Z</i>
<i>o</i> - <i>E,E</i> -DPD	Ground state energy difference relative to <i>E,E</i> (eV)	0	0.04	0.30
<i>m</i> - <i>E,E</i> -DPD	Ground state energy difference relative to <i>E,E</i> (eV)	0	0.25	0.52

5.2.2.2 Steady-State Spectroscopy Measurements

The steady-state irradiation spectra of *o*-*E,E*-DPD following photoexcitation at 294 nm (shown in Figure 5.9a) shows a depletion of absorbance of both main features in the spectrum (260 and 294 nm) up to the maximum time delay of 6 hrs, with an observed growth towards the 200 nm region. For the *m*-*E,E*-DPD species (Figure 5.9b) the steady-state irradiation centred on 272 nm shows a depletion of the main feature with a small increase in the absorbance at wavelengths below 250 nm. Also shown in

Figure 5.9 is the ^1H NMR spectra for both *o*-*E,E*-DPD and *m*-*E,E*-DPD following irradiation for 16 hrs.

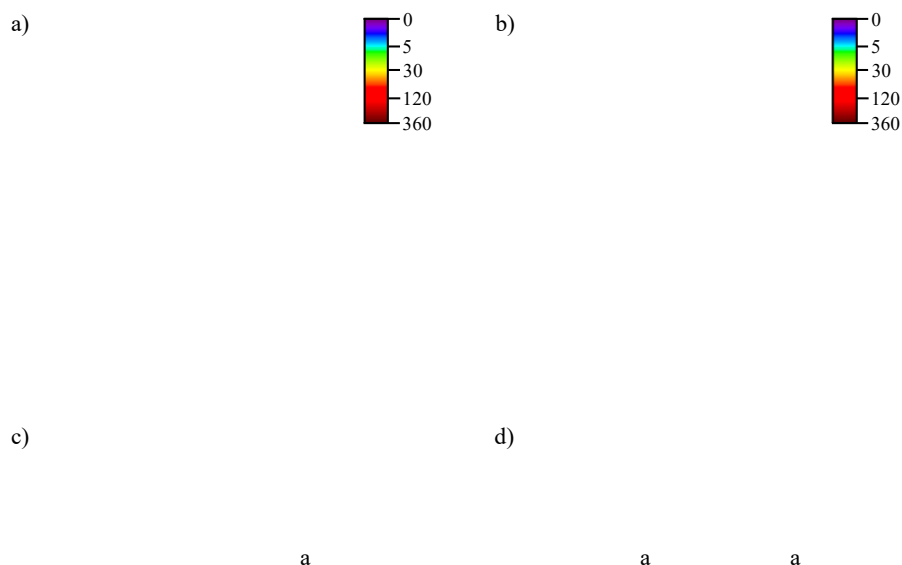


Figure 5.9 Steady-state irradiation spectra for both a) *o*-*E,E*-DPD and b) *m*-*E,E*-DPD in ethanol at $10\ \mu\text{M}$ concentration. Colour bar indicates irradiation time in minutes. c) ^1H NMR spectrum of *o*-*E,E*-DPD following 16 hrs of irradiation at 294 nm. d) ^1H NMR spectrum of *m*-*E,E*-DPD following 16 hrs of irradiation at 272 nm. a, denotes peaks with 13 Hz splitting.

5.2.3 Discussion

We begin by discussing the analysis of the ^1H NMR and steady-state irradiation (Figures 5.7 and 5.9). Both the initial *ortho* and *meta* samples are assigned to their *E,E* structures. This is further confirmed from the computed electronic ground state structures, showing the lowest energy to be the *E,E* isomer in both *ortho* and *meta* species (Table 5.2). The steady-state irradiation studies of both *o*-*E,E*-DPD and *m*-*E,E*-DPD species show no formation of a stable photoequilibrium between *E,E* and *E,Z* following irradiation for a maximum time of 6 hrs as seen for the *para* species in Chapter 4. ^1H NMR of the irradiated species shows the appearance of several new hydrogen environments for the *o*-*E,E*-DPD species, one of which is a doublet and can be attributed to the *E,Z* isomer due to the 13 Hz splitting. Similarly the ^1H NMR of the *m*-*E,E*-DPD species also displays two doublets attributed to *E,Z* isomer due to their 13 Hz splitting, along with the formation of several additional peaks. This initially suggests that irradiation of both *o*-*E,E*-DPD and *m*-*E,E*-DPD leads to photoisomerisation and the generation of the *E,Z* species for both *o*-*E,E*-DPD and

m-E,E-DPD. As in Chapter 4, from the ¹H NMR there is no environments that could be interpreted to the formation of the *Z,Z* isomer for either the *ortho* or *meta* species.

Dynamical information from the TAS was extracted through the use of a global sequential fitting model ($A \xrightarrow{\tau_1} B \xrightarrow{\tau_2} C \xrightarrow{\tau_3} D$), performed in Glotaran.^{26,27} The reported lifetimes and associated errors are displayed in Table 5.3 for both the *o-E,E*-DPD and *m-E,E*-DPD species. The evolutionary associated difference spectra (EADS) for both species are displayed in Figure 5.10. The quality of the fits was examined through the residuals which are displayed in Figure S5.2. Further information pertaining to the fitting procedure (along with a description of the origin of the residuals) is available in Section 2.4.

Table 5.3 lifetimes and associated errors (2σ) extracted from the global sequential fit for *o-E,E*-DPD and *m-E,E*-DPD in ethanol.

	τ_1	τ_2	τ_3
<i>o-E,E</i> -DPD	690 ± 50 fs	473.38 ± 10 ps	$\gg 3$ ns
<i>m-E,E</i> -DPD	1.28 ± 0.05 ps	1.263 ns ± 28 ps	$\gg 3$ ns

a)

b)

Figure 5.10 EADS for a) *o-E,E*-DPD in ethanol photoexcited at 294 nm and b) *m-E,E*-DPD in ethanol photoexcited at 272 nm.

Photoexcitation of *o-E,E*-DPD and *m-E,E*-DPD at 294 nm and 272 nm, respectively, leads to population of the vibrationally hot electronic excited state. This vibrationally hot electronic excited state then cools transferring the energy both through IVR and IET. Both of these processes occur with a lifetime of τ_1 , alongside of which any geometry arrangement required for moving out of the Franck-Condon region is also expected to occur within the lifetime of τ_1 . Between the EADS for τ_1 and τ_2 there is mild blue-shifting of the features which provide good evidence for vibrational cooling on the same excited electronic state, these mild shifts also imply that there is no electronic state change within the lifetime of τ_1 as discussed in Chapter 4 and observed previously for similar systems.^{28,29} τ_2 then describes the population travelling along the potential energy surface toward an accessible CI between the photoexcited state and the ground electronic state, similar to what is observed in *p-E,E*-DPD (*para* species). Like in Chapter 4, there is a significant increase in the excited state lifetime

for photoisomerisation when compared to the *para* methoxy substituted methyl cinnamate reported by Peperstraete *et al.*³⁰ This increase in the excited state lifetime could be attributed to greater steric hindrance between the methyl acrylate moieties constricting the geometry rearrangement as the population moves towards the CI. Furthermore, work by Promkatkaew *et al.*³¹ on hydroxy substituted methyl cinnamate showed that for the *ortho* species the potential energy surface is relatively flat with a low energy barrier to the CI, while for the *meta* species there is a large energy barrier which would inhibit a nonradiative relaxation through the CI. Both these results are in contrast with the *para* substituted species which has no energy barrier *en-route* to the CI thus the favoured relaxation mechanism would be a nonradiative decay through the CI back to the electronic ground state.

The final lifetime of τ_3 describes the long lived ESA centred at 360 nm in the probe region which persists beyond the temporal range of the experiment (3 ns). This feature could be attributed to the formation of the *E,Z* isomer, or to the presence of a long lived excited electronic state. As there appears to be no agreement between the steady-state irradiation and the final TAS the ESA is assigned to a transient species.

5.2.4 Conclusions for Substituent Effects on Photoisomerisation

The results and discussion presented above describe the latest understanding on the current avenue of research on functionalised cinnamates. While there is still a need for additional experimental and computational work, certain conclusions can be drawn from the present results. Firstly, the position of the methyl acrylate substitution on the phenyl ring drastically increases the excited state lifetime of the system compared to the results in Chapter 4 and those of the methoxy-methyl cinnamate reported by Peperstraete *et al.*^{4,30} This elongation of the excited state lifetime could be attributed to the formation of a barrier in the excited electronic state between the initially populated Franck-Condon region and CI, which has been previously proposed by Promkatkaew *et al.* for similar systems.^{31,32} Alternatively, the proposed flat nature of the excited state, coupled with the initial vibrational cooling for both the *ortho* and *meta* species may lead to an ineffective energetic drive to reach the CI, leading to an increased quantum yield for competing pathways such as fluorescence. Additionally, continuous irradiation of both species yields no stable photoequilibrium like what is

observed for the *para* substituted species, however there is evidence for *E* to *Z* isomerisation for both the *ortho* and *meta* species. Further computational studies similar to those in Chapter 4, and studies of the excited state potential energy surfaces performed by Promkatkaew *et al.* could certainly aid in the understanding of the relaxation mechanism. Such work is currently ongoing within the group and beyond the scope of this current thesis.

Finally, relating these results back to the role of photoprotection, the prolonged excited state lifetimes and degradation upon UV exposure shown here provide a poor demonstration of the photodynamical properties of a commercial UV filters. These results show that strongly favoured relaxation pathways such as photoisomerisation can be perturbed significantly by simply moving substituents one or two carbon atoms along the conjugated ring.

5.3 Supporting Information

5.3.1 Fitting Residuals

a) b) c)

Figure S5.1 False colour heat maps of fitting residuals for MAAs Sample 1 a) photoexcited at 328 nm b) photoexcited at 300 nm and c) MAA Sample 2 photoexcited at 357 nm.

a) b)

Figure S5.2 False colour heat maps of fitting residuals for a) *o*-*E,E*-DPD photoexcited at 294 nm and b) *m*-*E,E*-DPD photoexcited at 272 nm.

5.3.2 Power Dependencies

Power dependencies on Sample 2 show differing dependence on the pump beam power across the spectral features of the TAS. Power dependencies of *o*-*E*,*E*-DPD and *m*-*E*,*E*-DPD show a linear dependence across the spectral features of the TAS. These measurements were achieved by varying the TOPAS output power and taking a 10 nm integration window across a particular spectral window at a given pump-probe time delay.

a) b) c)

Figure S5.3 Power dependencies for the integrated intensity for MAA Sample 2, photoexcited at 357 nm: a) 10 nm integration window, 395-405 nm, at $\Delta t = 1$ ps pump-probe delay. b) 10 nm integration window, 390-4005 nm, at $\Delta t = 10$ ps pump-probe delay. c) 10 nm integration window, 695-705 nm, at $\Delta t = 10$ ps pump-probe delay.

a) b)

Figure S5.4 Power dependencies for the integrated intensity for 10 nm integration window centred on 350 nm at a pump-probe time delay of 1 ps for a) *o*-*E*,*E*-DPD, photoexcited at 294 nm b) *m*-*E*,*E*-DPD photoexcited at 272 nm.

5.4 Bibliography

- 1 M. D. Horbury, L. A. Baker, N. D. N. Rodrigues, W.-D. Quan and V. G. Stavros, *Chem. Phys. Lett.*, 2017, **673**, 62–67.
- 2 M. D. Horbury, E. L. Holt, L. M. M. Mouterde, P. Balaguer, J. Cebrián, L. Blasco, F. Allais and V. G. Stavros, *Nat. Commun.*, 2019, **10**, 1–8.
- 3 L. A. Baker, M. D. Horbury, S. E. Greenough, F. Allais, P. S. Walsh, S. Habershon and V. G. Stavros, *J. Phys. Chem. Lett.*, 2016, **7**, 56–61.
- 4 J. M. Woolley, J. S. Peters, M. A. P. Turner, G. J. Clarkson, M. D. Horbury and V. G. Stavros, *Phys. Chem. Chem. Phys.*, 2019, **21**, 14350–14356.
- 5 R. Losantos, I. Funes-Ardoiz, J. Aguilera, E. Herrera-Ceballos, C. García-Iriepa, P. J. Campos and D. Sampedro, *Angew. Chemie Int. Ed.*, 2017, **56**, 2632–2635.
- 6 M. Moliné, E. M. Arbeloa, M. R. Flores, D. Libkind, M. E. Farías, S. G. Bertolotti, M. S. Churio and M. R. van Broock, *Radiat. Res.*, 2011, **175**, 44–50.
- 7 E. M. Arbeloa, S. G. Bertolotti and M. S. Churio, *Photochem. Photobiol. Sci.*, 2011, **10**, 133–42.
- 8 R. P. Rastogi and A. Incharoensakdi, *Photochem. Photobiol. Sci.*, 2014, **13**, 1016–1024.
- 9 W. M. Bandaranayake, *Nat. Prod. Rep.*, 1998, **15**, 159–172.
- 10 F. R. Conde, M. O. Carignan, M. S. Churio and J. I. Carreto, *Photochem. Photobiol.*, 2003, **77**, 146–150.
- 11 Q. Gao and F. Garcia-Pichel, *Nat Rev Microbiol*, 2011, **9**, 791–802.
- 12 F. R. Conde, M. S. Churio and C. M. Previtali, *Photochem. Photobiol. Sci.*, 2004, **3**, 960–967.
- 13 J. M. Woolley, M. Staniforth, M. D. Horbury, G. W. Richings, M. Wills and V. G. Stavros, *J. Phys. Chem. Lett.*, 2018, **9**, 3043–3048.
- 14 S. Arai and M. C. Sauer, *J. Chem. Phys.*, 1966, **44**, 2297–2305.

- 15 M. J. Bedard-Hearn, R. E. Larsen and B. J. Schwartz, *J. Chem. Phys.*, 2005, **122**, 134506.
- 16 J. Peon, G. C. Hess, J.-M. L. Pecourt, T. Yuzawa and B. Kohler, *J. Phys. Chem. A*, 1999, **103**, 2460–2466.
- 17 F. R. Conde, M. S. Churio and C. M. Previtali, *J. Photochem. Photobiol. B Biol.*, 2000, **56**, 139–144.
- 18 F. R. Conde, M. S. Churio and C. M. Previtali, *Photochem. Photobiol. Sci.*, 2007, **6**, 669–674.
- 19 W. Humphrey, A. Dalke and K. Schulten, *J. Mol. Graph.*, 1996, **14**, 33–38.
- 20 T. H. Dunning, *J. Chem. Phys.*, 1989, **90**, 1007–1023.
- 21 C. Adamo and V. Barone, *J. Chem. Phys.*, 1999, **110**, 6158–6170.
- 22 M. Valiev, E. J. Bylaska, N. Govind, K. Kowalski, T. P. Straatsma, H. J. J. Van Dam, D. Wang, J. Nieplocha, E. Apra, T. L. Windus and W. A. De Jong, *Comput. Phys. Commun.*, 2010, **181**, 1477–1489.
- 23 A. Klamt and G. Schüürmann, *J. Chem. Soc. Perkin Trans. 2*, 1993, **0**, 799–805.
- 24 D. M. York and M. Karplus, *J. Phys. Chem. A*, 1999, **103**, 11060–11079.
- 25 P. Winget, D. M. Dolney, D. J. Giesen, C. J. Cramer and D. G. Truhlar, Minnesota solvent descriptor database, <http://comp.chem.umn.edu/solvation/mnsddb.pdf>.
- 26 J. J. Snellenburg, S. P. Laptinok, R. Seger, K. M. Mullen and I. H. M. van Stokkum, *J. Stat. Softw.*, 2012, **49**, 1–22.
- 27 K. M. Mullen and I. H. M. van Stokkum, *J. Stat. Softw.*, 2007, **18**, 1–46.
- 28 A. Espagne, D. H. Paik, P. Changenet-Barret, M. M. Martin and A. H. Zewail, *ChemPhysChem*, 2006, **7**, 1717–1726.
- 29 H. Kuramochi, S. Takeuchi and T. Tahara, *J. Phys. Chem. Lett.*, 2012, **3**, 2025–2029.
- 30 Y. Peperstraete, M. Staniforth, L. A. Baker, N. D. N. Rodrigues, N. C. Cole-

Filipiak, W.-D. Quan and V. G. Stavros, *Phys. Chem. Chem. Phys.*, 2016, **18**, 28140–28149.

- 31 M. Promkatkaew, S. Suramitr, T. Karpkird, S. Wanichwecharungruang, M. Ehara and S. Hannongbua, *Photochem. Photobiol. Sci.*, 2014, **13**, 583.
- 32 M. Promkatkaew, S. Suramitr, T. M. Karpkird, S. Namuangruk, M. Ehara and S. Hannongbua, *J. Chem. Phys.*, 2009, **131**, 224306.

6 Conclusions and Outlook

“Success is no accident. It is hard work, perseverance, learning, studying, sacrifice and most of all, love of what you are doing or learning to do.” **Pele.**

6.1 Conclusions

This thesis expands upon the accumulated knowledge in the field of photochemistry with an emphasis on understanding the key relaxation mechanisms employed by cosmeceutical relevant classes of molecules: mycosporine-like amino acids (MAAs) and cinnamates. The photoexcited dynamics of both MAAs and cinnamate derivatives have been studied in this thesis by employing ultrafast transient electronic absorption spectroscopy (TEAS) to monitor the evolution of excited population with femtosecond temporal resolution, combined with a molecular *bottom-up approach* to simplify the studied molecular systems to the base UV chromophore. Both MAAs and functionalised cinnamates have been described as future UV filters.^{1,2} Thus a fundamental understanding of the molecules' ability to dissipate the absorbed harmful UVA/B is warranted to aid their inclusion into any commercial formulations.³

In Chapter 1 we discussed the role of solar radiation and its effects on humans and the environment with a particular focus on MAAs and cinnamates. We then discussed the underlying quantum mechanical principles involved in the absorption and dissipation of energy within a molecule. Finally we introduced the TEAS technique, providing an overview of how this technique is useful for understanding the photochemistry of molecular systems in solution.

Chapter 2 discussed the fundamental physics needed to generate near infrared femtosecond laser pulses, and convert them to the UV region of the spectrum. These techniques are then applied to the design of the transient absorption spectroscopy apparatus used for the collection of data presented (and discussed) in Chapters 3, 4 and 5. To close this Chapter, we detailed the data collection methods and described the different fitting models available to extract dynamical information from the studies undertaken.

The first of the results Chapters employs the *bottom-up approach* to explore the photodynamics of two MAA motifs, one based on a cyclohexenone ring (3-aminocyclohex-2-en-1-one), termed ACyO and the other a cycloheximine ring ((*Z*)-*N*-(3-(butylamino)-2-methylcyclohex-2-en-1-ylidene)-butan-1-aminium 4-methylbenzenesulfonate), termed NN. For both systems multiple, solvent environments were utilised to explore different environmental effects on the photodynamics. Photoexcitation of ACyO in acetonitrile leads to population of a vibrationally hot

excited electronic state which cools with a lifetime of 2 ps. The population then remains trapped within the excited electronic state for the maximum time delay of the experiment (2.5 ns). ACyO in methanol leads to the same overall dynamics; a long lived excited electronic state, although there is a change in the spectral features plausibly attributed to the competition between a stimulated emission and excited state absorption. Following the photoexcitation of NN, the population traverses the excited electronic state to an accessible conical intersection (CI) with a lifetime on the order of 500 fs. Once the population has traversed through the CI back to the electronic ground state vibrational cooling occurs with a lifetime of 2 ps. Finally, there is a small long-lived component evidenced through global fitting of the data, which is attributed to either a trapped population in the excited electronic state or to the formation of a photoproduct. The observed photodynamics of both ACyO and NN are consistent with previous theoretical work showing that the accessible CI available to the NN species is higher in energy than the minimum of the S_1 for ACyO leading to the trapping of the photoexcited population at the minimum on the potential energy surface.⁴

In Chapter 4, we considered the effect of symmetric functionalisation on the photoisomerisation pathway of methyl cinnamate. 3,3'-(1,4-phenylene)(2*E*,2'*E*)-diacrylate (*p-E,E*-DPD) was synthesised by collaborators and both TEAS and steady-state irradiation combined with ¹H NMR experiments were performed. These experiments determined that photoisomerisation is the main relaxation pathway following photoexcitation with the lifetime for isomerisation found to be < 10 ps across all three solvents studied. This pathway leads to the reformation of the *E,E* species and the formation of *E,Z* which was confirmed through the use of ¹H NMR. While the relaxation through photoisomerisation was found to be the main pathway, there was also a long lived absorption which persisted to the maximum pump-probe time delay of 3 ns assigned to the presence of an $n\pi^*$ state.

Chapter 5 details recent unpublished work advancing on the results of the previous studies. The first section displays TEAS data on three different natural MAAs (mycosporine-glycine, shinorine and usujirene). Each shows a rapid relaxation through a CI back to the ground electronic state, similar to the observed dynamics of NN from Chapter 3. Interestingly, one of the MAAs studied, mycosporine-glycine, has a core structure similar to that of ACyO which, as discussed in Chapter 3, prevents effective repopulation of the electronic ground state. This points to the additional

functionality between the core structure of ACyO and mycosporine-glycine altering the potential energy surface to facilitate a rapid relaxation pathway. In the second section of Chapter 5 the role of functionalisation position of the methyl acrylate moiety is explored for both the *ortho* and *meta* species. From the collected TEAS and steady-state data, there is an observed difference in relaxation dynamics and photostability when compared to the *para* substituted species discussed in Chapter 4. Here both the *ortho* and *meta* species exhibit significantly longer excited state lifetimes; much greater than the 10 ps observed in Chapter 4, along with a decrease in photostability with no photoequilibrium reached after 6 hrs of irradiation. ^1H NMR of the irradiated samples showed that there was formation of the *E,Z* isomer for the both species. While further analysis is still required, there is a clear dependence between the relaxation dynamics and the position upon which substitution of the methyl acrylate moiety is made.

6.2 Outlook

6.2.1 Mycosporine-Like Amino Acids

The work shown here provides a fundamental *bottom-up approach* to exploring the photodynamics of MAAs through TEAS measurements. These studies highlight the core photodynamical properties of the molecules in the solution-phase, a key stepping stone to the use of MAAs as UV filters. Further studies can, and should, be undertaken to further explore the effects of functionalisation of the two core structures of MAAs, with the overall aim being to generate a catalogue of UV filters which provide optimal coverage across the UVA/B region of the electromagnetic spectrum. Studies carried out previously by Losantos *et al.*⁵ highlight this available opportunity to tune the absorbance across the UVA/B region by selecting the functional groups added to the core MAA moieties. Furthermore, unlike many current commercial UV filters, shown in Chapter 1, such as oxybenzone and cinnamates derivatives,^{6,7} which dissipate energy through hydrogen transfer or isomerisation, the mechanism for relaxation of MAAs is driven by the shape of the potential energy surface without requiring any hydrogen migration or large scale geometry changes.

6.2.2 Functionalisation and Substituent Effects of Cinnamates

Cinnamates have been previously studied through ultrafast spectroscopy to explore the photoisomerisation pathway.^{3,7} The effects of functionalisation across the phenyl ring on the photoisomerisation pathway has been previously examined through theoretical and steady-state methods.^{8,9} In Chapters 4 and (part of) Chapter 5, we have demonstrated through ultrafast spectroscopy a marked difference in the excited state lifetime following photoexcitation for a base methyl cinnamate structure substituted at different positions on the phenyl ring with an additional methyl acrylate moiety; this adds increased molecular complexity along with additional isomeric products. While the work is ongoing to understand the exact mechanism for the relaxation of the *ortho* and *meta* substituted species, there is a clear dependence between the formation of a photoequilibrium and the position of substitution within the methyl cinnamate.

Taken together (MAAs and cinnamates), the work presented in this thesis shows the detailed information which can be gained from the use of ultrafast spectroscopy measurements to monitor the photoexcited dynamics of UV filters. TEAS combined with a molecular *bottom-up approach* can provide insight into these dynamics and the effects of molecular functionalisation on these dynamics. This work has implications for the next generation of commercial UV filters; especially in light of the increasing need for enhanced UVA protection,¹⁰ and growing list of current UV filters which have reported toxicity and photoallergenic properties.^{11,12} Both MAAs and functionalised (current) UV filters may provide a suitable avenue for new UV filters that are both less phototoxic (to humans and aquatic life) as well as protecting humans across the entire UVA/B region of the electromagnetic spectrum.

6.3 Bibliography

- 1 N. A. Shaath, *Photochem. Photobiol. Sci.*, 2010, **9**, 464–469.
- 2 W. M. Bandaranayake, *Nat. Prod. Rep.*, 1998, **15**, 159–172.
- 3 N. D. N. Rodrigues and V. G. Stavros, *Sci. Prog.*, 2018, **101**, 8–31.
- 4 R. Losantos, I. Funes-Ardoiz, J. Aguilera, E. Herrera-Ceballos, C. García-Iriepa, P. J. Campos and D. Sampedro, *Angew. Chemie Int. Ed.*, 2017, **56**, 2632–2635.
- 5 R. Losantos, I. Lamas Frejo, R. Montero, A. Longarte and D. Sampedro, *Phys. Chem. Chem. Phys.*, 2019, **21**, 11376–11384.
- 6 L. A. Baker, M. D. Horbury, S. E. Greenough, P. M. Coulter, T. N. V Karsili, G. M. Roberts, A. J. Orr-Ewing, M. N. R. Ashfold and V. G. Stavros, *J. Phys. Chem. Lett.*, 2015, **6**, 1363–1368.
- 7 Y. Peperstraete, M. Staniforth, L. A. Baker, N. D. N. Rodrigues, N. C. Cole-Filipiak, W.-D. Quan and V. G. Stavros, *Phys. Chem. Chem. Phys.*, 2016, **18**, 28140–28149.
- 8 M. Promkatkaew, S. Suramitr, T. M. Karpkird, S. Namuangruk, M. Ehara and S. Hannongbua, *J. Chem. Phys.*, 2009, **131**, 224306.
- 9 M. Promkatkaew, S. Suramitr, T. Karpkird, S. Wanichwecharungruang, M. Ehara and S. Hannongbua, *Photochem. Photobiol. Sci.*, 2014, **13**, 583.
- 10 E. L. Holt and V. G. Stavros, *Int. Rev. Phys. Chem.*, 2019, **38**, 243–285.
- 11 M. Avenel-Audran, L. Martin, H. Dutartre, C. Bernier, M. Jeanmougin, C. Comte, J. L. Peyron, L. Benkalfate, M. Michel, M. C. Ferrier-Lebouëdec, M. Vigan, J. L. Bourrain, A. Goossens and O. Outtas, *Arch. Dermatol.*, 2010, **146**, 753–757.
- 12 C. A. Downs, E. Kramarsky-Winter, R. Segal, J. Fauth, S. Knutson, O. Bronstein, F. R. Ciner, R. Jeger, Y. Lichtenfeld, C. M. Woodley, P. Pennington, K. Cadenas, A. Kushmaro and Y. Loya, *Arch. Environ. Contam. Toxicol.*, 2016, **70**, 265–288.

